WATER-GAS SHIFT ASSISTED AUTOTHERMAL FUEL REFORMING

DING OVI LIAN

SCHOOL OF MECHANICAL AND AEROSPACE ENGINEERING

A thesis submitted to the

Nanyang Technological University

in fulfilment of the requirement for the degree of

Doctor of Philosophy

2008

Acknowledgement

I would like to express my heartfelt gratitude to my supervisor, A/P Chan Siew Hwa, for his selfless guidance and advice given during my PhD candidature. In addition, I would like to thank the technicians from Energy Systems Laboratory for their assistance in this period. Lastly, I would like to thank British Gas Asia Pacific for sponsoring this project.

Abstract

A rising concern on the energy and environment issues demands cleaner and more efficient energy systems to replace the existing energy systems. Fuel cell is recognised as a quiet and reliable power technology that has relatively low impact on the environment. Although fuel cell technologies are maturing, maximum performance is obtained with pure hydrogen and oxygen as gas feed. However, hydrogen production through renewable sources is still not economically viable. During this transitional period, fossil fuels will still be a significant energy resource, which underlines the importance of fuel reforming.

A project was sponsored to study fuel reforming processes which include steam reforming, partial oxidation and autothermal. Autothermal reforming (ATR), in particular, has been selected for further investigation as it combined steam reforming (STR) and partial oxidation (POX), which enabled it to operate at thermal-neutral condition.

The objective of this project is to study the behaviour of water-gas shift (WGS) assisted autothermal reforming (ATR) to enhance the concentration of hydrogen product without any external heat supply to the reformer.

To achieve this goal, an equilibrium study was conducted to assess STR, POX and ATR production capability and determine the conditions that are favourable for highest H_2 yield. This is followed by design and fabrication of ATR reactor and WGS reactor

according to the plug flow and other design criteria and set up of testing facilities. An extensive experiment data were then collected to determine the kinetic rates of each reforming reaction.

In addition to the fundamental study of thermodynamic and kinetic aspect of the processes performed in this project, a mathematical model had been coded to predict the behaviour and products of the standalone ATR and WGS assisted ATR (ATR-WGS) under steady state, cold-start and transient operation. Effects such as non-plug flow gas velocity profile, catalyst porosity profile and diffusion of gases in the porous catalyst were included in the mathematical model to make the model closer to reality.

The results from the model indicated that the recommended space velocity for ATR in order to obtain high H_2 and moderately low CO is around 300 hr^{-1}. For WGS, it determined that the optimum range of space velocity is between 106.09 hr^{-1} and 212.18 hr^{-1}. However, it should be noted that WGS is sensitive to operating temperature. Hence, it should operate between 873 and 973 K. The model also showed that the cold start time for ATR-WGS reactor is longer than standalone ATR reactor due to the addition of a slower WGS process. From the results of the model, it was also observed that WGS plays an important part in the final products of the reaction. In addition to these findings, the results showed that there are serious overshoot/undershoot of performance related parameters in the transients, whose values are quite different from those under steady state conditions. The results in the transient study also indicated that pulsing feed may increase H_2 with lower CO in the product.

In conclusion, the project on the development and optimization of WGS assisted ATR with methane as gas feed had been successfully completed which allows us to have better understanding on the complexity of the integrated system. In addition, it is concluded that the reforming models developed in this study can replicate the characteristics of the reformer under different operating conditions and parameters related to the transport phenomena occurred in the reformer.

Table of Content

List of figures and tables

Notations

List of symbols

a	No. of atoms
A_s	Geometric surface area per volume of catalyst, m^2/m^3
AF	Molar air-fuel ratio
b	No. of atoms
C	Concentration, mol/m^3
C_p	Specific heat at constant pressure, J/mol K
D_m	Mass diffusivity, m^2/s
G	Gibbs free energy, J
H	Total enthalpy, J
h_t	Heat transfer coefficient, W/m^2 K
h_m	Mass transfer coefficient, m/s
k	Equilibrium constant
k	Thermal conductivity, W/m K
n	Total mole number
P	Pressure, atm
$\overline{R}$	Universal gas constant (8.314), J/mol K
$\dot{r}$	Reaction rate, mol/m^3 s
T	Temperature, K
WF	Molar water-fuel ratio
w	Gas velocity, m/s

x No. of moles

z Axial distance, m

Greek Letters

α Thermal diffusivity, m^2/s

ε Porosity

λ Lagrangian multiplier

$\overline{\mu}$ Molar chemical potential, J/mol

ρ Density, kg/m^3

σ Collision diameter, $\mathring{A}$

Π Function

Ω Lennard-Jones potential

Subscripts

1 Reactants

2 Products

Cat Catalyst

g Gas

i Element index

j Specie index

l Constant

m Constant

n	Constant
o	Constant
s	Catalyst surface

1 Introduction

In view of limitation in global resources and worsening air pollution, fundamental efficiency improvements in the energy system are required. The energy crisis in California in 2001 highlighted such economic importance of energy and environmental issues and hence, the urgency to develop renewable and sustainable energy roadmap for the future generations [1, 2].

In the effort of facilitating the growth of renewable and sustainable energy, over 100 heads of government attended the United Nations' World Summit on Sustainable Development in Johannesburg in 2002. This summit is the successor to the much vaunted Earth Summit held in Rio de Janeiro a decade ago. The aim of this summit was to translate noble ideas visioned in Rio summit into plans with targets and timetables attached and to setup funds to help these projects [3]. Subsequently, Britain released its energy white paper which targeted to reduce 60% of the carbon dioxide emissions by 2050 from 1990's levels [4].

This change in energy policy and political support spurred research activities in the development of renewable and sustainable energy, which contribute to the technological innovations in the fields of energy and environment [5]. Consequently, renewable energy sources such as biomass [6, 7], wind [8, 9], ocean [10, 11], geothermal [12, 13] and solar [14, 15] are being explored extensively to reduce the reliance on fossil fuels. However, to build a truly renewable and sustainable energy system, hydrogen will have to join

electricity as the platform of future energy system. In this system, hydrogen is produced from renewable sources, such as via photoelectrolysis of water, in which energy from the sun is used to convert water into hydrogen and oxygen. Hydrogen is then used to power a fuel cell, in which hydrogen and oxygen from air recombine to produce electricity, heat and water. Consequently, this energy system will be highly efficient and will have zero impact on the environment, which resolves the energy demand and pollution issues.

Fuel cell, touted as a quiet and reliable power technology that has relatively low environmental impact, are intrinsically much more energy efficient than current power systems. They could achieve up to 80% system efficiency (with heat utilisation) in electric power plants using solid oxide fuel cells (SOFCs) and up to 50% efficiency for transportation using proton exchange membrane fuel cells (PEMFCs) [16]. Different fuel cells have different requirements on the operating temperature and fuel gas quality. For low temperature fuel cells, such as PEMFC, it requires hydrogen as the fuel and nearly CO-free and sulphur-free gas feed from the fuel processor.

To aid the development, US had proposed spending USD$273 million for Freedom Fuel program, which would focus on spurring research to develop the technologies and infrastructure needed to produce, store and distribute hydrogen for use in future fuel cell vehicles or stationary electric generating facilities. It is predicted that by 2040, the hydrogen fuel cell initiatives could reduce annual greenhouse gas emissions by more than 500 million metric tons of carbon equivalent each year [17]. In addition to this, US and Europe entered a fuel cell agreement to foster closer collaboration on fuel cell

development. The European commissioners and the American government would strengthen research links in both the public and private sectors and would look into overcoming the cost, performance and durability issues through joint EU-US projects [18].

Singapore also played a part in promoting clean energy by launching Singapore Initiative in New Energy Technology (SINERGY) programme. This joint initiative between Economic Development Board (EDB), Land Transport Authority (LTA) and Ministry of Environment (ENV) serves to encourage the development, adoption and commercialization of new technologies, products and innovations in the area of clean energy [19, 20]. In response to these programmes, Nanyang Technological University (NTU) formed Fuel Cell Strategic Research Programme (SRP) to conduct fuel cell-related research such as fuel reforming, Proton Exchange Membrane fuel cell (PEMFC), Solid Oxide fuel cell (SOFC) and integrated fuel cell - gas turbine system studies [21].

Although fuel cell technologies are maturing, hydrogen production through renewable sources is still not economically viable. The cost of production is often 2 to 3 times higher than current technologies and current petroleum infrastructure is unsuitable for it [22]. In the future, hydrogen and electricity will ultimately come from sustainable renewable energy resources but during this transitional period, fossil fuels will still be a significant energy resource. This is aided by the growth of fuel cell technology, which will provide a base for the establishment of the hydrogen option into the energy market.

Reforming of the fossil fuels to hydrogen may involve several steps including fuel deep desulphurisation, reforming, water-gas shift and carbon monoxide (CO) clean up. Traditionally, there are three thermochemical reforming process, i.e., steam reforming (STR), thermal decomposition (TDC) and partial oxidation (POX). STR is widely used in industry for making hydrogen (H_2) and syngas. STR generally gives higher H_2/CO ratios compared to POX for a given feed, but STR is endothermic and thus requires external heating. POX, on the other hand, is an exothermic process. However, it is more difficult to control and is less efficient. The major operating problems in catalytic POX include the over-heating or hot spots due to the exothermic nature of the reactions and coking problem.

ATR integrates POX and STR; thereby inheriting the characteristics of both processes. The main features of ATR are [23]:

- Low energy requirement, due to the opposite contribution of the exothermic and endothermic reaction
- Low specific consumption
- High gas space velocity (at least one order of magnitude relative to the traditional STR)
- Preset H_2/CO ratio easily regulated by inlet $CH_4/O_2/H_2O$ ratios

Despite the above advantages, ATR still faces a setback. The CO concentration in the products is still unacceptable for low temperature polymer electrolyte fuel cell applications where CO poisoning of the Pt catalysts is still a concern. To counter this,

clean up technologies, such as water-gas shift (WGS) and/or preferential oxidation (PROX) needs to be integrated with the reforming process. Both PROX and WGS reduces the CO concentration by oxidation but the latter can increase the hydrogen in the products and has a wide range of working temperature, whereas, the former has a limited working temperature window and could possibly decrease the hydrogen as oxygen is more selective towards hydrogen that to CO.

The objective of this research is to study the behaviour of water-gas shift (WGS) assisted autothermal reforming (ATR), which combines STR and POX processes, to enhance the concentration of hydrogen without any external heat supply to the reformer.

To achieve this goal, an equilibrium study will be conducted to assess STR, POX and ATR production capability and determine the conditions that are favourable for highest H_2 yield. This is followed by design and fabrication of ATR reactor and WGS reactor according to the plug flow and other design criteria. Two rigs will be designed and built for experiment purpose. Utilising the facilities, an extensive experiment data will be collected to determine the kinetic rates of each reforming reaction. The kinetic rates will then be incorporated into a mathematical model to study the behaviour of WGS assisted ATR under steady state, cold-start and transient operation.

The scope of the project includes the following:

- Literature review of hydrogen production, cleanup technologies, reactor design and catalyst treatment (Detailed in chapter 2)
- Thermodynamic analysis of fuel reforming process which includes STR, POX and ATR (Detailed in chapter 4 and 5)
- Thermodynamic analysis of WGS and WGS assisted ATR process (Detailed in chapter 4 and 5)
- Design and develop ATR reactors (Detailed in chapter 3 and appendix)
- Design and develop a reforming rig for studying the behaviour of the WGS assisted reforming process (Detailed in chapter 3 and appendix)
- Design and develop a kinetic rig to study and obtain kinetic rates for different catalysts in the WGS assisted reforming process (Detailed in chapter 3 and appendix)
- Obtain chemical kinetics of ATR process with Ni catalyst (Detailed in chapter 4)
- Obtain chemical kinetics of WGS process with Pt catalyst (Detailed in chapter 4)
- Modelling of kinetics reaction in ATR and WGS (Detailed in chapter 5)
- Determination of optimal operating range for ATR and WGS (Detailed in chapter 4 and 5)
- Modelling of the kinetic reactions in a WGS-assisted ATR reforming process (Detailed in chapter 5)
- Compare kinetic results with experimental data (Detailed in chapter 5)
- Study of transient behaviour of WGS assisted ATR fuel reformer (Detailed in chapter 5)
- Cold-start behaviour and modelling of WGS assisted ATR fuel reformer (Detailed in chapter 5)

From the scope listed above, one can see that this is a comprehensive study of ATR, WGS and WGS-assisted ATR reformer. The scope covers literature reviews, equilibrium study, design and fabrication works, experiments and mathematical modelling. This ensures that there is no lapse of understanding between each stage.

In the mathematical modelling, additional considerations such as non-plug flow gas velocity profile, catalyst porosity profile and diffusion of gases in the porous catalyst pallets are included to make the simulation model closer to reality. With heat transfer along the wall and gas-to-wall heat transfer integrated into the 2D model, the simulation model is unique and comprehensive.

Further studies on cold start study and transient performance of ATR-WGS are performed to understand the dynamic changes of the composition and temperature in the reactor during the cold start and transient operations as there are no studies done.

2 Literature Review

To meet the energy demands at lower rate of energy consumption with corresponding reduction in pollutant and CO_2-emissions, there must be a major improvement in the energy efficiency of power plants. This requires fundamental changes in the energy system and hydrogen is expected to join electricity as the foundation of future energy system. However, hydrogen does not exist as an available energy source and must be extracted from water, fossil fuels and renewable energy sources. During this extraction process, hydrogen and other products are produced and may require clean-up process to yield purer hydrogen.

At the moment, the choice of hydrogen production technologies are fossil fuel reforming [24, 25, 26], electrolysis [27, 28, 29], photoelectrolysis [30-36], photobiological [37, 38], biomass gasification and pyrolysis [39-43]. Among these technologies, hydrogen production from fossil fuels is favoured as the current petroleum infrastructure is suited for it and its production cost is relatively cheaper. Thus, the focus of this section would be on hydrocarbon fuel reforming as indicated in the scope of this study.

This literature review discusses some of the research and development in the hydrogen production and clean up technologies. Some works on catalyst and catalyst treatments would also be reviewed.

2.1 Hydrogen Production Technologies

Steam reforming (STR) has been the most important route for large scale manufacture of synthesis gas for ammonia, methanol and other petrochemicals [44]. Much research had been performed on it and the current direction of research point towards thermodynamic analysis and simulation of different configurations of system [45].

Ioannides [46], Lin *et al.* [47] and Lutz *et al.* [48] performed thermodynamic analysis on steam reforming with focus on different aspects. Ioannides and Lin *et al* studied the effects of operating parameters such as temperature, water/fuel ratio and pressure on the hydrogen yield of steam reforming while Lutz *et al* focused on the thermal efficiency of steam reforming and compared equilibrium results to experimental measurements. Ioannides observed that the yield of hydrogen (H_2) increases with increasing reforming temperature and approaches the stoichiometric yield at high temperature. In addition, the author noted that the increase of pressure has a negative effect on the hydrogen yield. Such effect was also discovered by Lin *et al.* when they conducted steam reforming experiments at high pressure and temperature using coal and lime (CaO) as the feedstock. They also found that reducing pressure will lead to more carbon monoxide (CO) and carbon dioxide (CO_2) in the product gas. On the other hand, Lutz *et al.* [48] observed that the experimental thermal efficiency is significantly lower than the predicted efficiency. The difference in the experimental and predicted result is attributed to the non-equilibrium composition as well as the heat transfer losses in the reactor. Since their model only made use of chemical equilibrium equations combined with system energy

balance, they are unable to predict results for different gas space velocities. However, they concluded that the equilibrium model is sufficient for understanding the effect of the temperature on the reaction. Beside these theoretical works, Achenbach and Riensche [49] carried out experiments to determine the kinetics of the methane/steam reforming process at anode materials of a solid oxide fuel cell. For temperature range of 700 °C - 940 °C, methane (CH_4) partial pressure of 0.11 – 0.33 bar and system pressure of 1.1 – 2.8 bar, their results show that there is no effect of the water (H_2O) partial pressure on the catalytic reforming process. They also concluded that at high temperatures and high conversion rate, the mass transfer effects must be taken into account. Similarly, Dicks and co-workers [50] conducted a kinetic study on the methane steam reforming rate given by a typical thin electrolyte-supported nickel/zirconia SOFC anode using a tubular plug flow differential reformer. The reaction rate was studied as a function of temperature (700 °C - 1000 °C) and partial pressure of methane (2 – 40 kPa), hydrogen (10 – 70 kPa) and steam (10 – 70 kPa) with total pressure of 1 atm. They found that the reaction was first order in methane with a weak positive effect of hydrogen and a stronger negative effect of steam.

In addition to the thermodynamic studies performed, many researchers also tried to increase the efficiency and production yield of the STR plant by trying different configurations, better system integration or novel solutions through either prototypes or computer simulations [51]. Han and co-workers [52] developed an on-site hydrogen generator which consists of a methanol steam reformer and a metal membrane purification module. The system is capable of producing 99.9995 % of pure hydrogen at

a rate of 10 Nm^3/h and has less than 1 ppm of CO in the product. By combining steam reforming, hydrogen purification and catalytic combustion into a single vessel, the system is able to reach an overall thermal efficiency of 82 % HHV CH_4. Other than this prototype, Asakura and co-workers [53] demonstrated two types of hydrogen production systems with different type of reformers; a low pressure reformer (less than 0.1MPa) and a medium-pressure reformer (0.1 to 0.98 MPa) using natural gas as the feedstock. The demonstrated systems each consist of a desulfurizer, burner, mixer, reformer, CO shift reactor and Pressure Swing Adsorption (PSA) unit. With this configuration, their low pressure system is able to generate 30 Nm^3/h of 99.999 % pure hydrogen and achieve less than 0.1 ppm for CO. In comparison, their medium pressure system is more compact and achieves about 10% higher efficiency. Beside these developments, Venkataraman *et al.* [54] ran several tests on a multi-pass catalytic wall reactor using methane and steam as feedstock. Their tests showed that catalytic coated thin wall eliminates heat transfer resistance and allows the reactor to operate at a lower temperature during catalytic combustion. Their results also showed that catalytic wall reactor is able to attain 90% and above for methane conversion and achieve high H_2/CO ratio of 14.

The other common thermochemical reforming process utilised in the industries is partial oxidation (POX). It has fast reaction time and is an exothermic process, which does not require heat supply to sustain the process [55]. However, it is difficult to control and is less efficient than STR. Much research had been carried out to improve the efficiency, understand and improve the process. Avel *et al.* [56] performed a series of computer simulations on hydrogen generation for PEMFC – integrated combined heat and power

(CHP) plant using natural gas as feed stock. They studied the effects of ethane and propane in natural gas and simulated the plant behaviour for different input conditions. Their results showed that the addition of ethane and propane in natural gas increases the temperature of the product by 110 K and 120 K, respectively. They also concluded that water injection and energy integration plays a critical role in controlling and adjusting the temperature. To understand the reforming process better, Zhu *et al.* [57] carried out thermodynamic study on methane partial oxidation. Using kinetic rates from CHEMKIN programme, they were able to show that there are two distinct reaction zones in the reactor during POX, namely, rapid oxidation zone and slow conversion zone with the rapid oxidation zone length shorten as the temperature increases. In addition, their model predicts the process will achieve optimum operating condition at temperature of greater than 1073 K and at O_2/CH_4 ratio of 0.5. However, they did not incorporate carbon as part of the products which could severely deactivate the catalysts during operation. This exclusion would have cause significant discrepancy in the simulation and experimental values. In addition to these, Voltz *et al.* [58] used an integral reformer to study the oxidation of CO and hydrocarbons (HC) over Pt-coated beads. They developed a rate expression that accounted for inhibition by CO, C_3H_6 and NO expressed as:

$$\dot{r}_{CO} = \frac{\mathrm{k}\chi_{CO}\chi_{O_2}}{(1+\mathrm{K}_{CO}\chi_{CO})^2} \qquad (1)$$

Other researchers like Muradov *et al.* [59] explored several novel approaches to produce hydrogen from natural gas with low CO_2 emissions. Using the most promising conceptual design, they performed a computer simulation on it. From their results, they found that

their design could lessen CO_2 emission which is 2.5 times lesser than that from steam methane reforming process.

The other area that contributes significantly to the improvement of POX process is the study and investigation of catalysts. Choudhary and co-workers [60] investigated the influence of different metal oxide substrate on the performance of nickel (Ni) and/or cobalt (Co) containing catalyst in the oxidative methane-to-syngas conversion at very low resident time. They observed that nickel-containing zirconium oxide (ZrO_2), thorium oxide (ThO_2) and uranium oxide (UO_2) catalysts showed good performance with the latter giving the best performance. In addition, they found that NiO-titanium oxide (TiO_2) and NiO-silicon oxide (SiO_2) catalyst showed poor performance as these catalysts deactivated very fast due to sintering of Ni and/or formation of catalytically inactive binary metal oxide phases by solid-solid reaction at the high catalyst calcination and/or catalytic reaction temperature.

The third reforming process is autothermal reforming (ATR). ATR is a combined process of partial oxidation (POX) and steam reforming (STR) under thermal-neutral condition. It has the advantage of being energy efficient although its hydrogen yield lies in between STR and POX. During the ATR process, the air-to-fuel (AF) ratio and the water-to-fuel (WF) ratio are two crucial parameters for a fixed composition of the fuel, in determining the reaction temperature and the reformate composition. Due to the ease of control and being energy efficient, ATR is the favoured approach to produce syngas from hydrocarbon fuels. Several researchers such as Chan *et al* [61] and Ayabe *et al.* [62]

performed thermodynamic analysis on ATR to gain better understanding in the process while Qi and co-workers [63] constructed an on-board ATR prototype for automobile to demonstrate its feasibility. Through the thermodynamic analysis of equilibrium products for natural gas undergone ATR, Chan and co-worker [61] were able to determine the parameters to obtain maximum hydrogen yield with minimum production of carbon monoxide and solid carbon. They predicted that an optimal hydrogen yield of 36.3 – 36.6 % can be achieved when the molar air-fuel ratio and molar water-fuel ratio are set to 3.5 and 2.5 – 4, respectively. Under this condition, it is found that the formation of carbon monoxide is 2.24 – 4.38 % while the formation of solid carbon is effectively suppressed to zero [64]. Their results show that the corresponding equilibrium temperature of the reaction is 820 – 871 K. They have also determined the sensitivity profile of hydrogen and carbon monoxide yield with respect to the change of natural gas composition [65]. Using the same technique, Ayabe *et al.* [62] carried out investigation on ATR of methane (CH_4) and propane (C_3H_6) over supported metal catalysts to determine the carbon deposition region and the heat balance of the reaction. Their simulated results agreed with their experimental results on ATR of CH_4, showing that little carbon deposition was observed. However, some significant discrepancy was observed between the predicted result and experimental result for ATR of propane as large amount of carbon was found deposited on the catalysts even under the steam-rich condition. They reasoned that this was due to initial decomposition of the hydrocarbon at the inlet zone. In the development of ATR system, Qi *et al.* [63] worked on gasoline autothermal reforming (ATR) systems and showed that on-board ATR systems are feasible and have great potential for on-board application. With the prototypes that they

have developed, they managed to obtain 62 % in thermal efficiency using 93 octane gasoline as fuel. They concluded that further integration of system components is required to improve the overall system efficiency and controllability.

2.2 Clean-up Technologies

After the primary reactors (such as ATR, STR or POX), the hydrogen-rich mixture from the reforming process typically contains 0.5-2 % of CO which must be removed or converted to an inert compound before being fed into a low temperature fuel cell [66]. Thus, there is a need for gases clean up and/or purification. Gasses cleanup and purification can be carried out by water-gas shift (WGS), preferential oxidation (PROX), methanation or membrane technologies. The choice of gasses cleanup and purification technology would depend on the purity of hydrogen feed required and compatibility with the reformate temperature.

Water-gas shift (WGS) is one of the major steps in H_2 production from gaseous, liquid and solid hydrocarbons or alcohols [67]. It plays a major role in most of the proposed processes for generating fuel-cell grade hydrogen. In addition to its potential role in generating fuel-cell grade hydrogen, WGS and its reverse have great importance in several commercial operations. Industrial processes using the WGS or its reverse usually carry out the reaction in two stages. The first step is at a higher temperature, frequently in the 400 ºC range. This step shifts up to 85 % of the CO to H_2 and converts all of the sulphur containing contaminants to H_2S, which is removed prior to low temperature

WGS. The low temperature WGS is typically in the 200 ºC range, which completes the CO conversion [68]. The high temperature shift catalysts used are normally chromium-promoted iron oxide formulations, while copper-zinc oxides are the usual basis for low temperature shift operations. For WGS process, the typical space velocity is 4000 h^{-1} [67].

Although WGS has been popularly adopted for gases cleanup, there is minimal understanding of the process. Currently, research works focus on the kinetics and the reaction mechanisms of WGS. A few other researchers like Tonkovich improved the WGS reactor by using novel solutions. Wang *et al*. [69] investigated the kinetic properties for the forward and reverse WGS reaction through energetic analysis. Their results showed that for surface redox mechanism, the rate controlling step in FWGS (Forward WGS) is the dissociation of adsorbed H_2O while the dissociation of adsorbed CO_2 is the rate controlling step of the RWGS (Reverse WGS) reaction. They also found that the RWGS reaction is more sensitive to the catalyst structure than the FWGS reaction. In addition, they discovered that increasing sulphur content in the gas feedstock would increase the activation barrier of the rate controlling step, thereby, poisoning the catalysts. In another research work, Koryabkina and co-workers [70] determined the kinetic parameters for water-gas shift reaction on Cu-based catalysts. They proposed that the kinetics can be explained based on the redox mechanism with $CO_* + O_* \rightarrow CO_{2*} + *$ as the rate-determining step. They also found that the addition of ZnO and ceria did not increase the rate per unit of Cu surface area and concluded that Cu is the active site for the catalysis. Likewise, Choi and Stenger [71] evaluated the existing reaction

mechanisms and compared the results with their experimental results for WGS reaction. They observed that the rate expressions derived from adsorptive mechanism and redox mechanism agreed with their results extremely well. However, they also noted that other expressions (including empirical expression) also matched their results with a high degree of accuracy. In addition to these works, Salmi and Hakkarainen [72] have investigated the transient kinetic, chemisorption and thermogravimetric of WGS on industrial copper-based catalyst. They found that there is a significant reduction of the catalyst and an increase in the surface area during the initial activation at 250 ºC. Their studies also showed that carbon dioxide response was faster than the hydrogen response at 250 ºC and 235 ºC, whereas at 150 ºC and 200 ºC, the carbon dioxide and hydrogen liberation rates were almost equal. They also observed that carbon dioxide and hydrogen formation rates were enhanced by water and water-hydrogen pre-treatment of the catalyst.

In an attempt to achieve a breakthrough in WGS process, Tonkovich and co-workers [73] conducted some studies on micro-channel WGS reactor. They observed fast intrinsic kinetics for the WGS reaction (about 25 ms) and 99.8 % CO conversion at 300 ºC for the micro-channel WGS reactor. Their successful experiments led them to conclude that micro-channel reactor reduces heat and mass transport limitations for reactions and facilitates fast intrinsic reaction kinetics, which can translate to smaller WGS reactor with one to two orders of magnitude than conventional processing hardware.

Other than these areas, researchers had also carried out tests on catalysts to find suitable catalysts for WGS process and investigate the effect of catalyst structure on the process. Patt and co-workers [74] have found that molybdenum carbide (Mo_2C) catalysts are more active than a commercial Cu-Zn-Al shift catalyst for the WGS reaction at 220 ºC to 295 ºC under atmospheric pressure. They also noted that Mo_2C did not catalyse the methanation reaction and is a promising candidate for new WGS catalyst. Similarly, Li *et al.* [75] conducted some experiments on Cu and Ni-containing cerium oxide catalysts for low temperature WGS. They observed that small quantities of base metal results in closely associated clusters with the ceria surface and this significantly enhanced the activity of ceria supported WGS catalysts. In addition to these, Saito *et al.* [76] investigated the water-gas shift reaction over Cu/ZnO-based multicomponent catalysts. They found that the activity of Cu/ZnO-based catalyst for the water-gas shift reaction was less affected by pre-treatments at high temperature and deemed to be a better candidate for water-gas shift reaction. They also observed that a two-stage reaction system composed of the first reaction zone for the water-gas shift reaction at 637 K (High Temperature Water-Gas Shift) and the second reaction zone for the reaction at 523K (Low Temperature Water-Gas Shift) was more efficient than a one-stage reaction system. Besides these studies, Tabakova *et al.* [77] examined supported gold catalysts on various supports for the WGS reaction. They concluded that the catalytic activity of the gold/metal oxide catalysts depends strongly not only on the dispersion of the gold particles but also on the state and the structure of the supports.

In partial oxidation (PROX), a small amount of air (usually about 2 %) is added to the gas stream, which then passes over a metal catalyst. This catalyst preferentially adsorbs CO, rather than H_2, where CO reacts with oxygen from the air and oxides to CO_2. Consequently, the crucial requirements for PROX reaction are high CO oxidation rate and high selectivity.

As with WGS process, researchers focus on the thermodynamic and kinetic studies and carry out prototype demonstrations on PROX processes to gain better understanding and experience. Himeno *et al.* [78] did a study on the selective oxidation of CO in a hydrogen-rich reformate gas for a polymer electrolyte membrane fuel cell (PEMFC) using Pt-Ru alumina supported catalyst. From their experiments, they were able to reduce CO concentration from 1 % to 50 ppm at temperature range of 393 to 473 K. They also attempted to create a prototype reactor to demonstrate the process in a larger scale. However, they were not able to achieve the results that they had observed and concluded that design of their prototype need to be optimised. Similarly, Dudfield and co-workers [79] designed and constructed a compact CO preferential oxidation (PROX) reactor for a 20 kW PEM fuel cell application. Their demonstration showed that their reactor was able to reduce CO feed stream from 2.7 % to less than 20 ppm with methanol steam reformer as the primary reactor. Besides these development, Lee *et al* [80] also demonstrated a PROX reactor for 10 kW PEMFC system. Their PROX reactor was able to achieve CO concentration of less than 20 ppm for 1.2 % CO gas feed after a start-up time of 3 min.

Other researchers like Korotkikh *et al.* [81], Choi *et al.* [82] and Kahlich *et al.* [83] performed detailed thermodynamic analysis on PROX process to gain insights into the operation of the PROX reactor. Korotkikh and co-worker studied the effect of space velocity, gas composition and temperature on activity and selectivity of PROX on Pt promoted monolith catalyst. They found that the conversion of CO was virtually independent of concentration and noticed that increasing the temperature from 90 to 150 °C showed a small increase in CO conversion and H_2 oxidation. In addition, their results showed that CO conversion decreases with increasing space velocity. Hence, they recommended that the PROX process to be carried out in a low space velocity and temperature operating condition. Choi and Stenger [82] carried out studies to evaluate various rate expressions and simulate the performance of the CO oxidation step of a methanol fuel processor. After verifying their rate expressions with their experimental results, they investigated the effect of O_2/CO ratio and water addition through computer simulation. They noted that O_2/CO ratio must be greater than 1 to achieve 100 % CO conversion; for high CO selectivity, higher O_2/CO ratio is advantageous at low temperature and vice versa. It was also shown that adding water increases the performance of PROX reactors. In addition, they found that the trend of decreasing CO conversion and selectivity at higher temperatures was caused by the reverse water gas shift reaction rather than a difference in the activation energies for CO oxidation and H_2 oxidation. Probing deeper, Kahlich *et al.* investigated a wide range of CO concentrations over Pt/Al_2O_3 catalyst. Their result showed that a CO oxidation rate enhancement by a factor of 2 in the presence of hydrogen. They suspected that the phenomenon could be due to either H_2-induced CO desorption or the interaction of the hydroxylated Al_2O_3

support with CO adsorbed on Pt. Similarly, Shishu [84] studied carbon monoxide (CO) oxidation over Pt in a differential reformer using a monolith substrate at low conversion levels (10%). After carrying out several sets of experiment, Shishu fitted his data in the simple power law form, which describes the kinetic reaction for CO oxidation:

$$\dot{r}_{CO} = \frac{k\chi_{O_2}}{\chi_{CO}^{0.5}} \tag{2}$$

In addition to these work, Kim and Lim [66] performed a study on selective CO oxidation on Pt/Alumina (Al_2O_3) in hydrogen-rich mixtures for the range of 150 °C - 350 °C and concentration of 0.5 % - 2 % for oxygen and carbon monoxide. They described the intrinsic kinetics of the CO oxidation by a simple power law expression, with activation energy of 78 kJ/mol and reaction orders of -0.51 and 0.76 for the CO and oxygen (O_2) partial pressure, respectively. Their results also showed that the selectivity displayed a maximum with increasing temperature and was dependent mainly on the feed composition and reaction temperature.

Other than these areas, researchers had also carried out tests on catalysts to find suitable catalysts for PROX process. Rohland and plzak [85] investigated on CO oxidation using Fe_2O_3-Au catalyst to explore the feasibility of integrating the process with PEMFC system. From their experiment, they achieved relatively high oxidation rate at 1000 ppm CO and 5 % air-bleed at 80ºC. From these test, they concluded that a PEMFC-integrated CO oxidation system is highly feasible with the catalyst used. Besides this work, Dudfield and co-workers [79] reported on a compact CO preferential oxidation reactor

for PEMFC applications. They tested a range of non-precious and precious metal catalysts and found that activated Pt-Ru formation catalyst has the highest level of activity and selectivity towards CO oxidation. Likewise, Snytnikov *et al.* [86] conducted experiments on selective oxidation of CO over Pt, Ru and Pd supported catalysts. They observed that the Ru and Pt catalysts were the most active and selective among the studied catalysts and concluded that these catalysts are able to provide a single step removal of CO from hydrogen-rich stream both in the absence and presence of CO_2 and H_2O to a PEMFC tolerant level.

The third chemical clean-up process discussed in this section is Methanation, which is a highly exothermic reaction. The process is a hydrogenation of CO using H_2 that is already present in the feed stream and is capable of reducing the CO content to less than 100 ppm in hydrogen-rich reforming gases. This approach avoids the oxygen addition and thus avoids complicating the clean-up process. In methanation, the methane produced does not poison the electrode but only acts a diluent [16]. However, the disadvantage of this method is the consumption of hydrogen, which is the desired product.

In view of this disadvantage, not much research work has been done in this area for fuel cell applications. Sughrue and Bartholomew [87] performed a large array of experiment parameters to determine the kinetics of CO methanation on nickel (Ni) catalyst. With the kinetics of the methanation process obtained, further studies were carried to investigate the effects of product inhibition by water and methane on the activity of the Ni catalyst.

They observed that methane does not inhibit the rate of CO methanation whereas they found that water is a strong inhibitor and an irreversible poison at sufficiently high temperatures and concentrations.

In attempt to improve the CO methanation process, Ledjeff-Hey and co-workers [88] performed a theoretical study on the CO management system to reduce CO to an acceptable level for PEMFC application. From their study, they found that a combined process of carbon dioxide scrubber with subsequent methanation will reduce the carbon monoxide content to an acceptable level of less than 10 ppm. Other than this developmental work, Gorke *et al.* [89] constructed a microchannel reactor to reduce the CO content by methanation process. They demonstrated that the reactor was able to carry out methanation at residence times of 300 ms and was able to remove CO almost completely from the gas flow at a temperature of 300 °C. From their experiments, they observed that the temperature has to be controlled precisely to achieve the desired result due to the different reaction mechanisms that could happen during the process.

The last gases clean-up and purification method is membrane separation technology. This approach is different from previously mentioned process as it is a mechanical rather than chemical approach. Whilst the use of diffusion membranes facilitates the supply of ultra-pure hydrogen to the fuel cells, the technology is inherently expensive and operates under high-pressure differentials, e.g., 10 to 20 bar. However, the selective removal of hydrogen in a membrane reactor would allow the hydrogen production process to operate at lower reaction temperatures than conventional processes [16].

In the numerous research works done on membrane technology, palladium membrane has been studied more extensively than other types of membranes for hydrogen separation since it is permeable only to hydrogen [16]. Using palladium membrane, Uemiya and co-workers [90] conducted an investigation on a double tubular type membrane reactor. Their results showed that the CO can be converted beyond equilibrium and the level of CO conversion is dependent on the thickness of palladium film. In the development work, Kikuchi *et al.* [91] have developed a composite membrane consisting of thin palladium layer deposited on the outer surface of porous ceramics. By using electrodeless-plating, the palladium layer could completely cover the surface, so that only hydrogen could permeate through the membrane with 100 % selectivity. Such membrane has been incorporated into a prototype steam reformer developed by Tokyo Gas and Mitsubishi Heavy Industries for the PEMFC system, which has demonstrated its feasibility. However, the cost of palladium membrane is still a major stumbling block to general adoption of the technology. Realising this, Criscuoli *et al.* [92] performed an economical analysis of palladium membrane reactors. They analysed the effect of the palladium thickness and permeability to hydrogen on costs of membrane devices. They found that a palladium membrane with thickness less than 20 μm could represent a possible alternative to conventional apparatus.

2.3 Modelling Related

Up to this point, the reviews have been focused on the reforming technologies and gases clean-up and purification technologies. The reviews on these areas are sufficient for comprehending the mechanisms and knowing the development work of each process. However, these are not adequate for conducting experiments and simulating the reforming and clean-up process. Other aspects of reforming process such as heat transfer characteristic, velocity profile, temperature profile, design of reactor, catalysts characteristics and its pre-treatment of catalysts in the reactor need to be investigated as well. The investigation of heat transfer and profiles in the reactor would lead to better understanding of the thermodynamic aspect of the gases. As such, incorporating these understandings would result in a more comprehensive simulation model.

Lamine *et al.* [93] investigated the radial heat transfer in packed columns and compared results obtained with gas and liquid flow. They found that the effective radial thermal conductivity of the packed bed increases linearly with the fluid velocity but the slope is found to be lower for liquid than for gas. They also observed that the radial thermal conductivity and wall heat transfer coefficient to be independent of the axial position. In addition, Vortmeyer and Haidegger [94] compared two mathematical approaches, namely, Wall Heat Transfer (WHT) and Wall Heat Conduction (WHC) methods in determining the design safety and operations of exothermic catalytic reactors with experimental results. They found large differences between calculated and measured near wall temperatures for WHT method while results using WHC method, agreed well

with the experimental data. They concluded that models using WHC method would have significant improvements in the axial temperature profiles and hot spot location than those using WHT method.

In order to probe deeper, investigation on the porosity of catalyst and its effect on velocity and temperature profile is important. As such, Papageorgiou and Froment [95] modelled fixed bed reactors without any chemical reaction, incorporating the structure non-uniformities of the bed. Their results showed that in the region extending up to a distance of two particle diameters from the wall bounding surface, flow oscillates in a strongly damped fashion with peak velocities at locations of higher voidage. Similarly, Schnitzlein [96] conducted a numerical study to investigate the two dimensional porosity distributions in the packed beds. From this, the author made a conclusion that the contribution of branching effects and channelling to fluid-mechanical radial dispersion can be separately represented by means of a detailed pseudohomogenous model provided that the numerical eddy diffusion introduced by the discretisation procedure can be kept sufficiently small. Likewise, Borkink and Westerterp [97] studied the influence of a radial porosity and velocity profile on the temperature and concentration profiles in wall-cooled packed beds. From their observations, it was found that the effective radial heat conductivity can be taken as constant over the radius despite the wall effect. However, they discovered that the influence of a radial superficial velocity profile can be significant through the convective term in the heat balance, especially for low tube-to-particle diameter ratios; the discrepancies in NTU (Number of Transfer Unit) can range from 20 % for high Reynolds number and up to 100 % for low Reynolds number. They

concluded that significantly higher values for the temperatures can be predicted, if radial porosity and velocity profile are incorporated in the heat and mass balances due to the non-uniform distribution of active catalyst over the radius. In addition to these works, Levent [98] did a theoretical study on the distribution of concentration and temperature in the porous iron oxide/chromia catalyst for water-gas shift reaction. His study showed that the external temperature differences are large as compared with intraparticle temperature differences at high fluid temperature. He also showed that the intraparticle temperature gradient might have larger effect on the reaction rate than the concentration when the heat of reaction was large. In addition, his results showed maximum temperature difference between surface and interior of the catalyst is about 49K at the highest reaction rate while the external temperature differences between the fluid and surface temperatures are of the order of 100 K. In the same field of work, Kalthoff and Vortmeyer [99] measured ignition/extinction temperatures and temperature profiles in a wall cooled exothermic fixed bed reactor are compared with the solutions of the two dimensional pseudo-homogenous model. They found that best agreement with experiments was obtained when the governing equations were solved with respect to radial profile velocity distribution. Adding to these researchers' works, Bey and Eigenberger [100] conducted a series of experiments to determine the velocity profile for different sphere, ring and cylinder sizes. In the range of velocities and tube-to-particle diameters, they found that the velocity is the highest in the vicinity of the tube wall. They also have fitted the experiment results to a model and found it to agree with the results satisfactory.

2.4 Experiment Related

Before the commencement of experiments, getting the proper design of the reactor is important as subsequent simulation work of the process would be based on the reactor design. Appropriate dimensions of the reactor, such as length and diameter, are crucial as they affect the space velocity, gas concentration and temperature profile. Consequently, it is critical to obtain useful information and data for proper design of a reactor [24].

Dierickx *et al.* [101] presented a set of plug flow criteria at the Amsterdam convention. In order to obey the plug flow criteria, the following rules must be applied:

- Greater than 10 – 20 particles on reformer diameter i.e. $d_t > 10d_{particle}$
- Greater than 3 – 5 extrudates on reformer diameter i.e. $d_t > 3d_{extrudate}$
- Longer than 50 – 100 extrudates on bed length i.e. $l_t > 50l_{extrudate}$

Once the above conditions are applied, the flow in the reformer should have the similar space velocity along each streamline and radially uniform conditions in temperature, pressure and composition. Any by-passing of flow, velocity gradients in the reformer, non-uniformity of the bed and back-mixing would deviate from plug flow. Rose [102] stated that for plug flow reformer, the tubes are usually narrow to ensure high surface/volume ratio as heat generation in the plug flow reformer are uneven and temperature rise can be uncontrollable. He also stated that a reformer with length/diameter ratio of 10 will have plug flow characteristics. Besides these criteria, Schmidt [103] presented a chart that shows the estimated space times (mean residence

times) for different processes versus the nominal reformer temperatures as shown in figure 1. It can be seen from the chart that the mean residence times for autothermal process should lay between 10^{-3} - 1 sec.

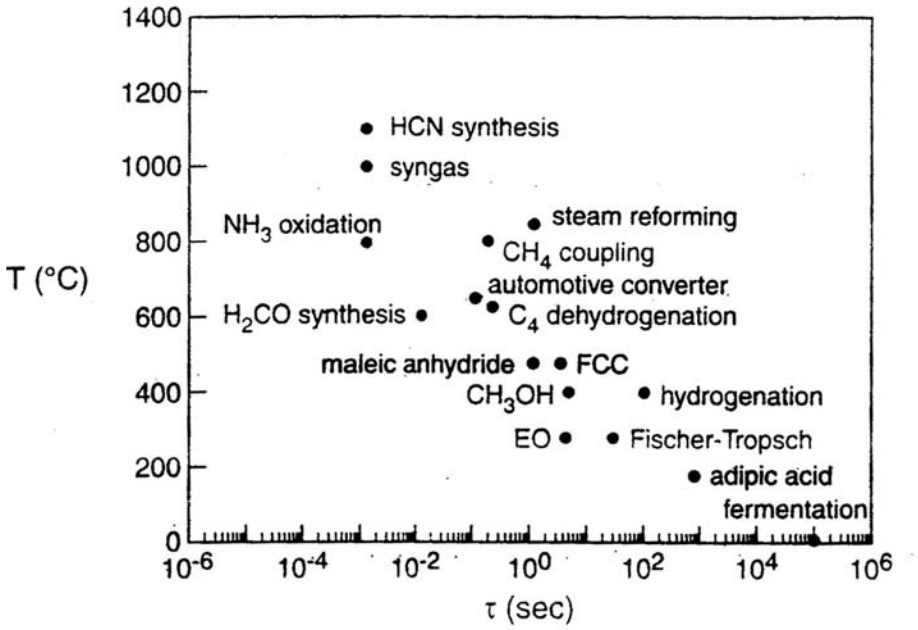

Figure 1: Reformer residence times required for different processes

During the process of hydrocarbon fuel reforming, it is likely that coking will occur in the process. Hence, considerable attention must be given on the issues of coking and carbon formation. Coking and carbon formation on the catalysts will potentially deactivate the catalysts and drastically reduce the performance of the reforming process. Research on this issue was carried out by Tracz *et* al [104]. Their study, on deactivation of Ni/Al_2O_3 catalyst caused by carbon, led to the observation of 3 kinds of carbon deposits formed during the reaction of hydrocarbon steam reforming, namely, true filaments, tubes and shells. They found that only shells have a deactivating characteristic and the kinds of carbon formations are dependent on the temperature. In addition to this, Fatsikostas and

Verykios [105] looked into the reaction of steam reforming of ethanol over nickel catalysts. They observed that, in the presence of Ni, the catalytic activity shifted towards lower temperatures. They also noted that the high dehydrogenation activity of Ni caused significant carbon deposits on the catalysts. Besides this, Demicheli and co-workers [106] studied the kinetics of carbon formation from STR CH_4-H_2 mixtures diluted with N_2 in the temperature range of 838-938K at atmospheric pressure. They found that carbon accumulation rate increased with increasing partial pressure of methane and decreased with increasing partial pressure of hydrogen. They were able to detect two types of carbon, C_α and C_β. They also noticed higher degree of crystallinity of carbon when temperature is increased. Ayabe *et al* [62] investigated catalytic ATR of methane and propane over supported metal catalysts. They determined the carbon deposition region using equilibrium calculations and found that there was little carbon deposition the deposition free region expected from the calculations. The deposited carbon that they observed has fibrous morphology, which did not affect the activation of the catalyst. Bartholomew [107] carried out an in-depth study on the deactivation phenomena connected with steam reforming and methanation using nickel catalyst. His study revealed that formation of graphitic carbon from H_2O/CH_4 mixtures is likely at low pressures and very high temperatures. It also showed that the decomposition of hydrocarbons on metal catalyst to form coke and carbons is very complex, which involved 1) reactions of adsorbed carbon to form amorphous, vermicular and graphitic carbons and 2) condensation of C_nH_m radicals on the nickel surface to form a high molecular weight polymeric coke. His study indicated that sufficient H_2 or H_2O will shorten the surface residence time of active carbon species, and will prevent coke

precursors to transform these species to more inactive forms, thereby minimising the formation of condensed hydrocarbons and amorphous and graphitic carbons.

Another important consideration for the experimental work is the suitability of catalyst. There are several types of catalyst available with the choice of precious or non-precious metal supported on different types of substrate. Some works [108-111] has already been done to find the performance and suitability of different types of catalyst [93, 112-114]. For instance, Lu *et al.* [115-117] performed an extensive review on the progress in catalyst innovation, optimization of reaction conditions, reaction mechanism and catalyst performance in methanol synthesis. They have also conducted a study to investigate the effects of reaction parameters on catalytic activity and carbon deposition on nickel catalysts. From these works, it is noted that precious metal catalyst gives an overall good performance albeit expensive.

The next consideration is the pretreatment procedure of the catalyst. Pre-treatment of catalyst is necessary to reactivate the catalyst (due to coking and carbon formation) or increase the activity of the catalyst prior to reforming [118]. From the works of several researchers [119-122], it is gathered that pretreatment of catalyst requires passing of hydrogen and inert gas for 1 hour at temperature above its light-off temperature. The flow rate, gas composition and temperature vary with each researcher [60, 123, and 124].

2.5 Summary

The literature survey showed that there is a wide coverage in the hydrocarbon fuel reforming and clean-up technologies. Even then, there are minimal understandings in WGS and no studies on ATR-WGS. Majority of the theoretical studies investigated the reforming and clean-up processes using equilibrium calculations. Equilibrium models are unable to predict results for different gas space velocities and mass transfer effect are not taken into consideration. This resulted in some discrepancies between experimental and equilibrium results. For the kinetic modeling works done, there are no inclusion of porosity and velocity profile. They also assumed that reactor gases travelled in a plug flow manner in their models. Besides this, there is also a lack of transient and cold-start studies done on the fuel reforming and clean-up technologies. Subsequently, these areas will be covered and improved in the current work.

Having considered many aspects of the simulation model and experiment, the research can progress from literature review to equilibrium study, and to the next stage of performing experiments and obtaining the kinetic rates of the reactions occurred in autothermal reforming. With the kinetic rates obtained, simulation of ATR, WGS and ATR-WGS process can be performed and analysed. This will include parametric studies, optimisation of the process, cold-start and transient studies. In order to make the 2D model more comprehensive and realistic, the catalysts in the reformer is modelled as a non-uniform (in radial direction) porous media, where gases in the reformer can diffuse in and out of the catalysts. The velocity and temperature profile affected by the catalysts

porosity are also taken into consideration, and hence a non plug flow model. With heat transfer along the wall and gas-to-wall heat transfer integrated into the 2D model, the simulation model is unique and comprehensive.

3 Experimental Setup and Methodology

Two test rigs, namely, the kinetic rig and reforming rig, were designed and built for the purpose of obtaining kinetic rates and verifying simulation results. The kinetic rig was designed for obtaining the kinetics of chemical reactions that occurred in the reactor, whereas, the reforming rig was used for verifying the simulation results at a larger scale. Further details on the test rigs and its corresponding flow process will be described in this section. Besides this, some information on the catalysts and the pre-treatment technique will be presented as well.

3.1 Kinetic Rig

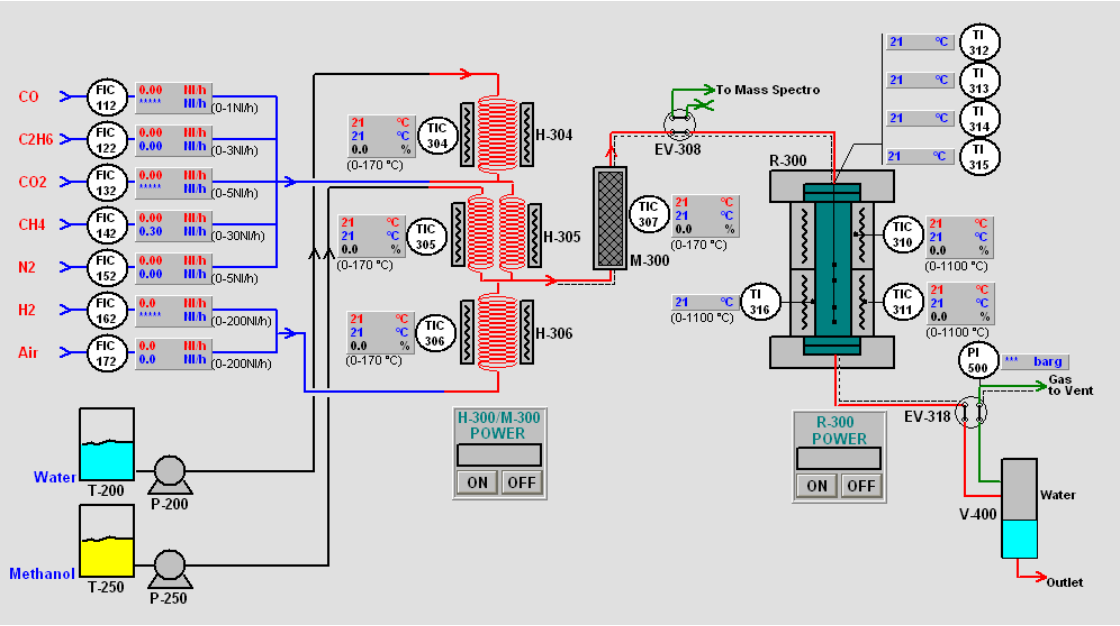

Figure 2: Schematic layout of kinetic rig

The schematic layout of the kinetic rig used for the current experimental study of gas reforming is shown in figure 2. In this system, the gas temperatures and flow rates are automatically controlled by electronic controllers to the set values. The system operation is automatically controlled by the system controller with a computer interface for monitoring and setting the operating parameters. Besides this, the system pressure in the kinetic rig is regulated by a high temperature resistant back-end pressure regulator.

The reformer is a stainless steel tube with an inner diameter of 10 mm and total length of 400 mm divided into three zones including a preheating zone of 100 mm, a reaction zone of 150 mm and a cooling zone of 150 mm. The preheating and cooling zone are filled with inert material (alumina) while the reaction zone is filled with either nickel catalyst (for obtaining kinetics of STR and POX) or platinum catalyst (for obtaining kinetics of WGS). Both the preheating and reaction zone are heated by a separate heater; the temperature in these two zones are measured and controlled by a four point thermocouple inserted in the center of the reformer.

During the reforming process, metered water (if necessary for the process) is supplied by the piston pump through the evaporator and mixed with metered gases (CH_4 and air) in the mixer. This mixture is then preheated before entering the reformer containing heated catalyst. After leaving the reformer, the reformate gas is passed through the condenser, the gas-liquid separator and the gas dryer to remove water content before entering the

gases analyser where its dry composition is determined. The dry composition of the products is measure by traditional CO, CO_2, O_2 and H_2 gas analysers coupled with hydrocarbon Flame Ionisation Detector (FID). N_2, if expected in the gas composition, is obtained by subtracting the measured gas composition from 100%. Each gas measurement is taken at interval of 1 min for 3 times and averaged to minimise measurement error.

The experimental conditions for methane steam reforming (STR) and partial oxidation (POX) in this study are set in a range that ensure normal and reliable operation of the kinetic rig and catalyst. The temperature in the reformer ranges from 773 to 1173 K, ensuring high catalyst activity. The reformer pressure is regulated at 1.5 bars and residence time of up to 3.6 kg cat·s/mol of inlet CH_4 with WF and AF molar ratio from 2 to 5 and 2 to 15, respectively, is carried out. Extensive trial tests was first carried out to check the transient time, reading repeatability and the carbon deposition on the catalysts before new catalyst was replaced and prepared for official experiments. The trial tests showed that during proposed time duration for experiments the repeatability is good and no carbon deposition is seen on catalysts when they are removed from the reactor. This suggests that the probability of deactivation of the catalysts is small. Therefore, the effect of the catalyst deactivation on the reforming performance is ignored.

3.2 Reforming Rig

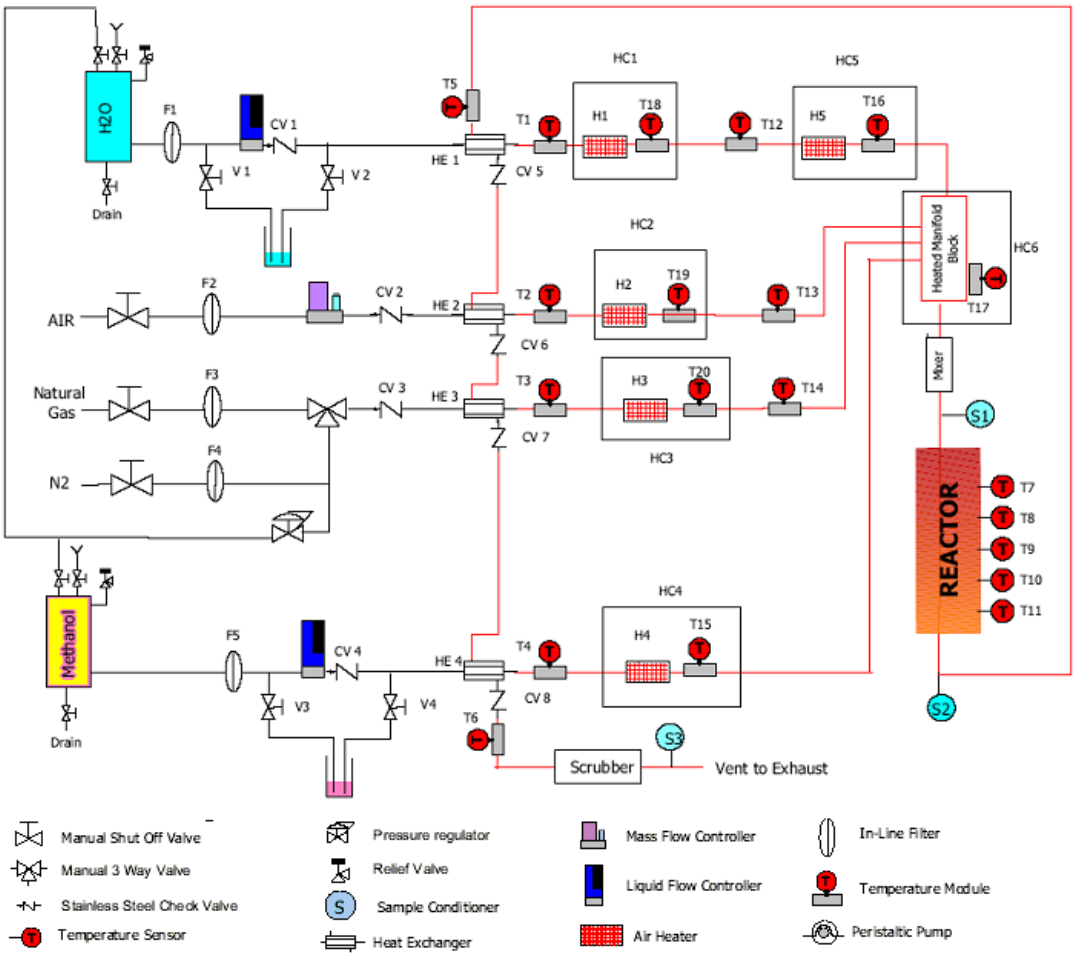

Figure 3: Schematic layout of reforming rig

The schematic layout of the reforming rig used in this study is shown in figure 3. In this system, the flow rates of air, methane and water are automatically controlled by a computer according to the set values. The feedstock passed through a heated manifold and mixer before entering the reactor at atmospheric pressure; the hot reformate gas from

the reactor is recycled to assist in heating the feedstock to ensure that water is in vapour state.

The reactor in this rig is designed and fabricated to satisfy the plug flow criteria listed by Dierickx [101] and the residence times provided by Schmidt [103]. The reformer is a stainless steel tube with an inner diameter of 30 mm and 400mm in length, of which the first and last quarter of the reactor is filled with inert material while the remaining is filled by catalyst. An independent heater is located at the reactor to initiate the start-up process and insulate against heat lost. Four thermocouples are placed along the reactor to monitor and record the reactor temperatures. The gas pipes are covered with thermal insulation material to minimise heat loss to the environment. Further technical information about the reformer can be obtained in the Appendix section.

Before the reforming process can be started on this system, the catalyst has to be warmed up to above its light-off temperature using an independent heater. After the temperature is reached, methane at flow rate of 2 l/min and air with air to fuel (AF) ratio of 3 are supplied. When the average catalyst temperature reaches 750 °C, water vapour is added to the inlet mixture and the flow rate of methane, AF ratio and molar water to fuel (WF) ratio are set to appropriate values to sustain thermally neutral operation between 500 to 900 °C. Based on the theoretical analysis of optimum conditions for autothermal reforming of methane [122], the AF ratio is varied from 2.5 to 4 and at each AF ratio, the WF ratio is varied. The WF ratio is increased at an increment of 0.5 from starting value of 1 until the autothermal reaction cannot be sustained. At each setting, a duration of 30

minutes is spent for the reactor to reach steady state before any data is recorded. The reformate gas is passed through the gas-liquid separator and the gas dryer to remove water content before entering to the gas analysers where its dry composition is determined. The dry composition of the products is measure by traditional CO, CO_2, O_2 and H_2 gas analysers coupled with hydrocarbon Flame Ionisation Detector (FID). N_2, if expected in the gas composition, is obtained by subtracting the measured gas composition from 100%. Each gas measurement is taken at interval of 1 min for 3 times and averaged to minimise measurement error.

Extensive trial tests was first carried out to check the transient time, reading repeatability and the carbon deposition on the catalysts before new catalyst was replaced and prepared for official experiments. The trial tests showed that during proposed time duration for experiments the repeatability is good and no carbon deposition is seen on catalysts when they are removed from the reactor. This suggests that the probability of deactivation of the catalysts is small. Therefore, the effect of the catalyst deactivation on the reforming performance is ignored.

3.3 Catalysts

The two types of catalysts used in the experiment, namely, sulfided nickel supported on gamma alumina and platinum supported on alumina, are supplied by Engelhard Company.

The nickel catalyst is a new type of commercial catalyst specialised for hydrogen production by hydrocarbon fuel reforming. The reasons for choosing this catalyst are that it is highly active, cheap and has prospective use in industries compared to other types of conventional nickel/ alpha alumina catalyst [126]. Conversely, the platinum catalyst is a common catalyst used for various applications. The reasons for choosing the catalyst in this study are that it is thermally stable and has wider range of operating temperature than conventional copper catalyst used for WGS application

Both catalysts are of spherical type and ready for use as supplied. The physical properties of the nickel and platinum catalyst are as shown in table 1.

	Nickel Catalyst	**Platinum Catalyst**
Active metal	Nickel	Platinum
Active metal content	9.8% on dry basis	0.5 % on dry basis
Metal distribution	Edge	Edge
Type	Reduced; dry	Reduced; dry
Support	Alumina spheres	Alumina spheres
Surface area	155 m^2/g	80 m^2/g
Mean particle size	1.1 mm	3.3 mm
Bulk density	0.55 g/cm^3	0.7 g/cm^3
Crush strength	2.55 kg	7 kg

Table 1: Physical properties of catalysts

In the verifying experiments, the amount of Ni and Pt catalyst loaded in the reforming reactor is 68 g and 132.78 g, respectively. The Ni and Pt catalysts are used as supplied. For the kinetic experiments, the amount of Ni and Pt catalyst loaded in the reaction zone of the kinetic reformer is 8.89 g and 14.48 g, respectively. The Pt catalysts are crushed into smaller pieces about 1mm in size before loading into the reactor while the Ni catalysts are used as supplied

At the beginning of each round of experiment, the Ni and Pt catalyst are pre-treated to reactivate the catalysts. This is to prevent any significant difference in the activity of the catalysts between each round of experiment and thus, good repeatability of the results. The catalyst is heated gradually to 873 K in nitrogen, after which, the catalyst is sustained at the same temperature for 1 hour in hydrogen. The catalyst is then kept at this temperature for a further hour in nitrogen to flush any residue hydrogen in the catalyst before the temperature is reduced to the required operating temperature.

4 Mathematical Modelling

In this chapter, the equations and concepts used in the simulation of the fuel reforming will be discussed in details. Two computer simulation models, namely, equilibrium model and kinetic model, have been used to predict the fuel reforming results. The equilibrium model is capable of predicting the final equilibrium products and temperature while the kinetic model is capable of predicting the real and transient behaviour and characteristics, in addition to the gas products and temperature. A brief description of the simulation programmes will also be included in this chapter.

4.1 Equilibrium Model

As is known, either the equilibrium or the rate conversion of a chemical reaction depends on the temperature, pressure and composition of the reactants. Many industrial reactions are not carried out to equilibrium and thus reactor design is based primarily on the reaction rate. Though employing a suitable catalyst to speed up a particular reaction is crucial, the choice of operating conditions may still be affected by equilibrium considerations. Chemical equilibrium of a reaction provides a target by which to measure improvements in a process. It may also determine whether or not an experimental investigation of a new process is worthwhile to explore. For example, if thermodynamic analysis indicates that a yield of x% in a process is possible at equilibrium and if a yield

of greater than x% is desired for the process to be commercially viable, there is no point to pursue the study.

The chemical equilibrium can be studied by two common approaches. One is based on equilibrium constants [127, 128] while the other is based on minimisation of the free energy [129]. One of the disadvantages of using the former is that it is rather difficult to test for the presence of some condensed species (either liquid or solid) in the reaction products than the latter. It is anticipated that solid carbon may form during the fuel reforming process and deactivate the active catalytic sites, thus retarding the catalytic reactions. Hence, a method based on minimisation of free energy is normally used in fuel reforming analysis. The condition of the chemical equilibrium may be stated in terms of thermodynamic functions such as the minimisation of Gibbs free energy or Helmholtz free energy or the maximisation of entropy. Among these, minimisation of the Gibbs free energy is more favourable when the reaction temperature and pressure are specified.

In this model, the chemical reaction for CH_4 undergoing ATR and WGS is described by the following:

$$x_0\mathrm{CH_4} + AF(\mathrm{O_2} + 3.76\mathrm{N_2}) + WF\mathrm{H_2O(g)} \rightarrow x_1\mathrm{CO_2} + x_2\mathrm{CO} + x_3\mathrm{O_2} + x_4\mathrm{N_2} + x_5\mathrm{H_2} + x_6\mathrm{CH_4} + x_7\mathrm{H_2O(g)} + x_8\mathrm{C(s)} \quad (3)$$

$$R_0\mathrm{CO} + W_0\mathrm{H_2O(g)} \rightarrow R_1\mathrm{CO_2} + R_2\mathrm{H_2} + R_3\mathrm{CO} + R_4\mathrm{H_2O(g)} \quad (4)$$

The Gibbs free energy for the above reactions can be expressed as:

$$G = \sum_{j=1}^{n} \mu_j x_j \qquad , j = 1 \ldots m,\ m+1 \ldots n \tag{5}$$

where n is the number moles of j species (1 to m are for ideal gases and m+1 to n are for condensed species

The molar chemical potential of species j is defined by [130]:

$$\bar{\mu}_j = \left(\frac{\partial G}{\partial n_j} \right)_{T,P,x_{i \neq j}} \tag{6}$$

The equilibrium state at fixed T and P is determined by minimising the Gibbs free energy subject to the constraints imposed by atom conservation:

$$b_i = \sum_{j=1}^{n} a_{ij} x_j = b_i^o \tag{7}$$

where a_{ij} is the number of atoms of element i in species j

b_i^o is the number of atoms of element i in the reactants

Defining a term Π to be:

$$\Pi = G + \sum_{i=1}^{l} \lambda_i \left(b_i - b_i^o \right) \tag{8}$$

where λ_i are Lagrangian multipliers

The condition for equilibrium thus becomes:

$$\partial \Pi = \sum_{j=1}^{n} \left(\bar{\mu}_j + \sum_{i=1}^{l} \lambda_i a_{ij} \right) \delta x_j + \sum_{i=1}^{l} \left(b_i - b_i^o \right) \delta \lambda_i = 0 \tag{9}$$

Treating the variations δx_j and $\delta \lambda_i$ as independent gives:

$$\bar{\mu}_j + \sum_{i=1}^{l} \lambda_i a_{ij} = 0 \tag{10}$$

Hence, for ideal gases,

$$\frac{\bar{\mu}_j^o}{\bar{R}T} + \ln\left(\frac{x_j}{x} \right) + \ln\left(\frac{P}{P_o} \right) + \sum_{i=1}^{l} \pi_i a_{ij} = 0 \tag{11}$$

where $x = \sum_{j=1}^{m} x_j$ $\qquad j=1 \ldots m$

For condensed species,

$$\frac{\bar{\mu}_j^o}{\bar{R}T} + \sum_{i=1}^{l} \pi_i a_{ij} = 0 \qquad j=m+1 \ldots n \tag{12}$$

where $\pi_i = \frac{\lambda_i}{\bar{R}T}$

For a given temperature and pressure, equations (7), (10) to (12) form a set of $n+l+1$ simultaneous equations.

Consider the chemical reaction (3), the system of simultaneous equations to be solved is:

$$x_1 + x_2 + x_6 + x_8 - x_0 = 0 \tag{13a}$$

$$2x_1 + x_2 + 2x_3 + x_7 - (2AF + WF) = 0 \tag{13b}$$

$$2x_4 - 7.52AF = 0 \tag{13c}$$

$$2x_5 + 4x_6 + 2x_7 - (4x_0 + 2WF) = 0 \tag{13d}$$

$$\frac{\mu_1^o}{\bar{R}T} + \ln\left(\frac{x_1}{x}\right) + \ln\left(\frac{P}{P_0}\right) + (\pi_1 + 2\pi_2) = 0 \tag{13e}$$

$$\frac{\mu_2^o}{\bar{R}T} + \ln\left(\frac{x_2}{x}\right) + \ln\left(\frac{P}{P_0}\right) + (\pi_1 + \pi_2) = 0 \tag{13f}$$

$$\frac{\mu_3^o}{\bar{R}T} + \ln\left(\frac{x_3}{x}\right) + \ln\left(\frac{P}{P_0}\right) + (2\pi_2) = 0 \tag{13g}$$

$$\frac{\mu_4^o}{\bar{R}T} + \ln\left(\frac{x_4}{x}\right) + \ln\left(\frac{P}{P_0}\right) + (2\pi_3) = 0 \tag{13h}$$

$$\frac{\mu_5^o}{\overline{R}T} + \ln\left(\frac{x_5}{x}\right) + \ln\left(\frac{P}{P_0}\right) + (2\pi_4) = 0 \tag{13i}$$

$$\frac{\mu_6^o}{\overline{R}T} + \ln\left(\frac{x_6}{x}\right) + \ln\left(\frac{P}{P_0}\right) + (\pi_1 + 4\pi_4) = 0 \tag{13j}$$

$$\frac{\mu_7^o}{\overline{R}T} + \ln\left(\frac{x_7}{x}\right) + \ln\left(\frac{P}{P_0}\right) + (2\pi_4 + \pi_2) = 0 \tag{13k}$$

$$\frac{\mu_8^o}{\overline{R}T} + (\pi_1) = 0 \tag{13l}$$

$$x = x_1 + x_2 + x_3 + x_4 + x_5 + x_6 + x_7 + x_8 \tag{13m}$$

For WGS, to determine the moles of products, the system of equations to be solved is:

$$R_1 + R_3 - R_0 = 0 \tag{14a}$$

$$2R_1 + R_3 + R_4 - (R_0 + W_0) = 0 \tag{14b}$$

$$2R_2 + 2R_4 - 2W_0 = 0 \tag{14c}$$

$$\frac{\mu_1^o}{\overline{R}T} + \ln\left(\frac{R_1}{R}\right) + \ln\left(\frac{P}{P_0}\right) + (\pi_1 + 2\pi_2) = 0 \tag{14d}$$

$$\frac{\mu_2^o}{\overline{R}T} + \ln\left(\frac{R_2}{R}\right) + \ln\left(\frac{P}{P_0}\right) + (2\pi_3) = 0 \tag{14e}$$

$$\frac{\mu_3^o}{\overline{R}T} + \ln\left(\frac{R_3}{R}\right) + \ln\left(\frac{P}{P_0}\right) + (\pi_1 + \pi_2) = 0 \tag{14f}$$

$$\frac{\mu_4^o}{\overline{R}T} + \ln\left(\frac{R_4}{R}\right) + \ln\left(\frac{P}{P_0}\right) + (\pi_2 + 2\pi_3) = 0 \tag{14g}$$

$$R = R_1 + R_2 + R_3 + R_4 \tag{14h}$$

It can be seen that the systems of simultaneous equations are a mixture of linear and non-linear equations. The method adopted in this model to solve these type of simultaneous equations is known as Newton Raphson method. The details of this method are described in several textbooks for numerical methods for solving nonlinear equations [131, 132].

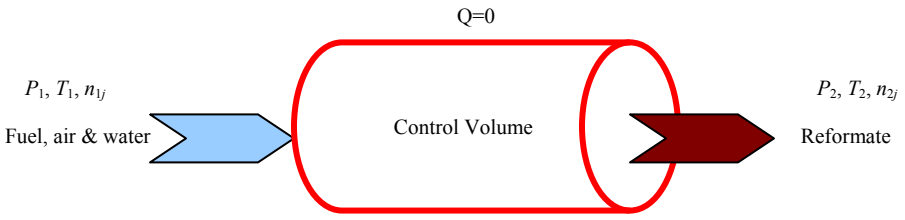

Figure 4: Schematic diagram of reforming process

Since the compositions of the reformate is dependent on the equilibrium temperature of the product, it is necessary to determine the reformate compositions in conjunction with the product temperature from the above equations. With continuous iterations, it is then possible to determine the equilibrium temperature of the products. From figure 4, it can be seen that the equilibrium temperature (denoted as T_2) can be computed from the following equation under adiabatic condition:

$$H_1\left(P_1, T_1, n_{1_j}\right) = H_2\left(P_2, T_2, n_{2_j}\right) \qquad j=1\ldots\text{m} \tag{15}$$

where j is number of species

subscript 1 is the inlet

subscript 2 is the outlet

The assumptions for this computation of equilibrium temperature are as follow:

- Steady flow process with negligible change of kinetic and potential changes
- Perfect insulation of reformer i.e. no heat loss to the surroundings
- Equilibrium chemical reactions with known reactants and products compositions
- Isobaric reactions with reactants entering the reformer at 1 atm and 298 K

A flow process of the equilibrium fuel reforming simulation program is shown in the following figure 5.

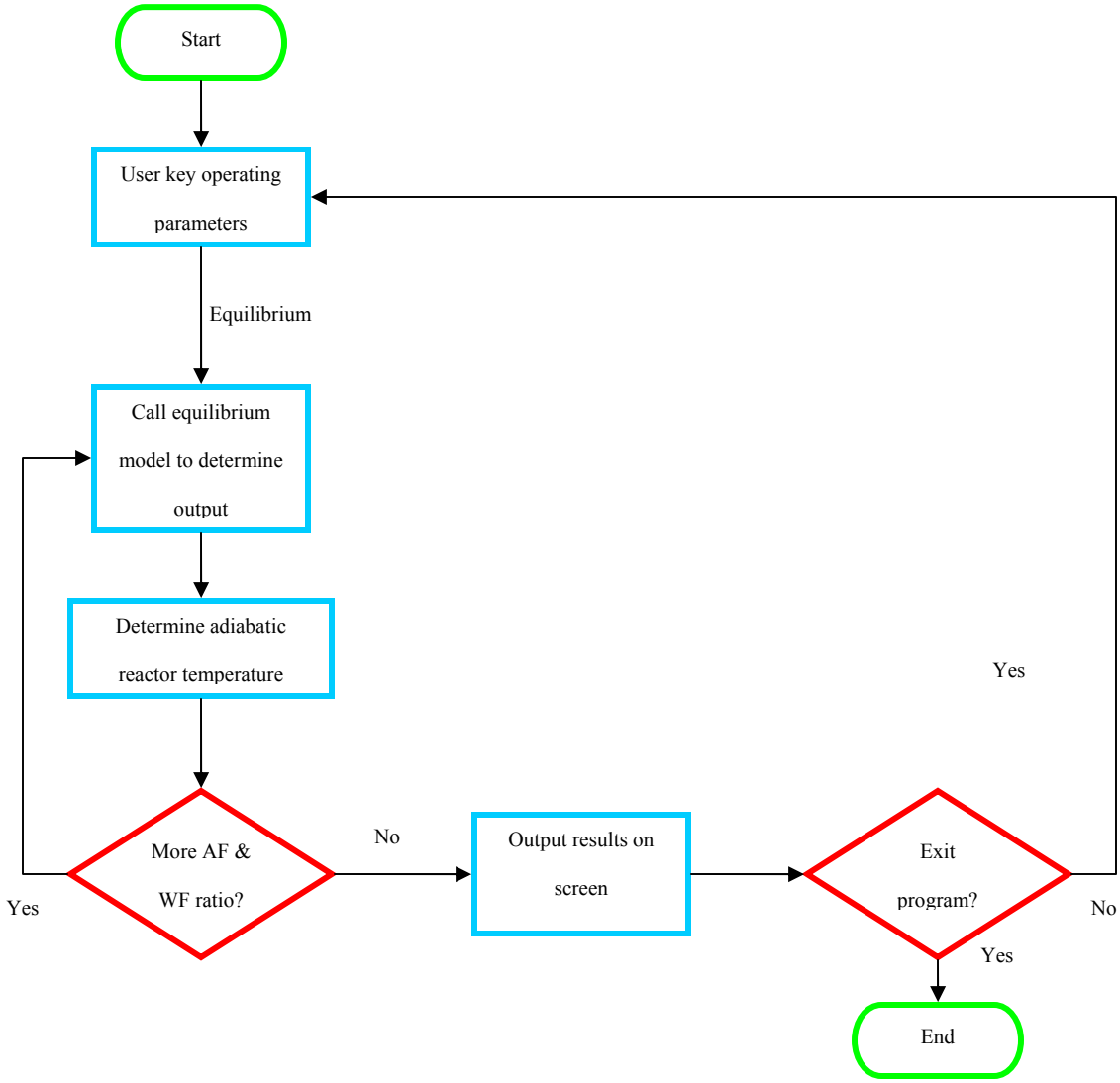

Figure 5: Process flow of equilibrium fuel reforming program

The fuel reforming program, written in Visual Basic programming language, allows various operating variables such as gas inlet temperature, gas pressure, gas flow rate, molar air-fuel ratio and molar water-fuel ratio to be set. In addition to this, the chemical equilibrium model can run with or without WGS reforming. After the variables and

options have been set, the program would perform the calculations for the chemical equilibrium model and their sub-procedures. For the chemical equilibrium model, after determining the products composition, the adiabatic reactor temperature could be determined. The final results of the chemical equilibrium model are then displayed in numerical form on-screen.

4.2 Kinetic Model

In chemical equilibrium model, the objective of the model is to determine the composition present at equilibrium for a specified temperature and pressure, whereas, in chemical kinetic model, the objective is to determine how quickly or slowly the equilibrium mixture is formed by considering the kinetics of the reactions, thereby understanding the behaviour of the reactions. In order to achieve this, the kinetics of each reaction must be determined through experiment.

For ATR, which is a combination of POX and STR at thermal-neutral conditions, the possible reactions in methane autothermal reforming are as follows [133-135]:

No.	Reaction	ΔH_{298} (kJ/mol)
1	$CH_4 + 2O_2 \rightarrow CO_2 + 2H_2O$	-802
2	$CH_4 + H_2O \rightarrow CO + 3H_2$	206.1
3	$CO + H_2O \rightarrow CO_2 + H_2$	-41.15
4	$CH_4 + 2H_2O \rightarrow CO_2 + 4H_2$	165.0
5	$CH_4 + CO_2 \rightarrow 2CO + 2H_2$	247.3
6	$CH_4 + 3CO_2 \rightarrow 4CO + 2H_2O$	330.0
7	$CH_4 \rightarrow C + 2H_2$	74.82
8	$2CO \rightarrow C + CO_2$	-173.3
9	$CO + H_2 \rightarrow C + H_2O$	-131.3
10	$CO_2 + 2H_2 \rightarrow C + 2H_2O$	-90.13
11	$CH_4 + 2CO \rightarrow 3C + 2H_2O$	-187.6
12	$CH_4 + CO_2 \rightarrow 2C + 2H_2O$	-15.3

Table 2: Reactions in autothermal reforming

However, according to thermodynamic analysis of the previous studies [133, 134], the main reactions in ATR are exothermic complete oxidation (reaction 1), steam reforming (reaction 2), water-gas shift (reaction 3) and CO_2-produced reforming reactions of methane (reaction 4) while other side reactions play insignificant role in the overall reaction. For example, the magnitude of the rate of direct CO_2 reforming reaction is very much smaller than that of the rates of complete oxidation and steam reforming reactions. Therefore, in this study, only the four major reactions, that is, reactions 1 to 4, are considered in ATR.

ATR is a combination of POX and STR under thermal-neutral condition. As a consequence, the kinetics for reaction 1 is obtained from performing methane POX while the kinetics for reaction 2 to 4 are extracted from methane STR.

For low-temperature WGS, the overall chemical reaction is shown in equation (16) [136]; the details of reaction mechanism of the low-temperature WGS will be presented in the corresponding section. As seen from the chemical reaction, WGS is a mildly exothermic reaction that is good for reducing CO level and enhancing H_2 production.

$$CO + H_2O \rightarrow CO_2 + H_2 \qquad (\Delta H_{298}\ (kJ/mol) = -41.15) \qquad (16)$$

The assumptions made during the development of the kinetic model are listed as follows:

1. Reactions can only occur under the presence of catalyst

2. Radiative heat transfer effect is negligible as maximum catalyst temperature is less than 1000 ºC
3. Pressure drop across the reactor is assumed to be negligible as gas flow rate is relatively low and the porosity of the bed is high enough (about 0.35)

In the following sections, the kinetic details and mechanisms of the STR, POX and WGS will be presented accordingly.

4.2.1 Kinetics of Steam Reforming

The overall conversion rate of methane to water and other gases in the reforming process can be determined from the experiments. The relationship between the conversion rates (χ_i) and resident times ($m_{cat} / F_{CH_4}^{in}$) can be expressed in the form of polynomial function as follows:

$$x_{CH_4} = a_0 + a_1\left(\frac{m_{cat}}{F_{CH_4}^{in}}\right) + a_2\left(\frac{m_{cat}}{F_{CH_4}^{in}}\right)^2 + a_3\left(\frac{m_{cat}}{F_{CH_4}^{in}}\right)^3 \quad (17)$$

$$x_{CO_2} = b_0 + b_1\left(\frac{m_{cat}}{F_{CH_4}^{in}}\right) + b_2\left(\frac{m_{cat}}{F_{CH_4}^{in}}\right)^2 + b_3\left(\frac{m_{cat}}{F_{CH_4}^{in}}\right)^3 \quad (18)$$

$$x_{H_2O} = c_0 + c_1\left(\frac{m_{cat}}{F_{CH_4}^{in}}\right) + c_2\left(\frac{m_{cat}}{F_{CH_4}^{in}}\right)^2 + c_3\left(\frac{m_{cat}}{F_{CH_4}^{in}}\right)^3 \quad (19)$$

$$x_{CO} = d_0 + d_1\left(\frac{m_{cat}}{F_{CH_4}^{in}}\right) + d_2\left(\frac{m_{cat}}{F_{CH_4}^{in}}\right)^2 + d_3\left(\frac{m_{cat}}{F_{CH_4}^{in}}\right)^3 \quad (20)$$

$$x_{H_2} = e_0 + e_1\left(\frac{m_{cat}}{F^{in}_{CH_4}}\right) + e_2\left(\frac{m_{cat}}{F^{in}_{CH_4}}\right)^2 + e_3\left(\frac{m_{cat}}{F^{in}_{CH_4}}\right)^3 \quad (21)$$

where

x_i is mole of i species conversion per mole of inlet CH_4, mol

m_{cat} is mass of catalyst, kg

$F^{in}_{CH_4}$ is inlet molar flow rate of CH_4, mol/s

$m_{cat} / F^{in}_{CH_4}$ is resident time, kgcat·s/mol

a_i to e_i (i=0-3) are constants

With assumption (1), the boundary conditions can be set as:

At $m_{cat} / F^{in}_{CH_4} = 0$, $x_i = 0$ (i=CH_4, CO_2, H_2O, CO and H_2)

Incorporating the boundary conditions, the constants, a_i to e_i (i=0-3), in the equations (17) to (21) can be determined by fitting these functions to the experimental data run on Ni catalyst. For example, the constants, a_i to b_i (i=0-3), in equations (17) and (18) can be obtained by fitting into experimental data shown in figure 6 and 7 under different resident time and methane conversion rate.

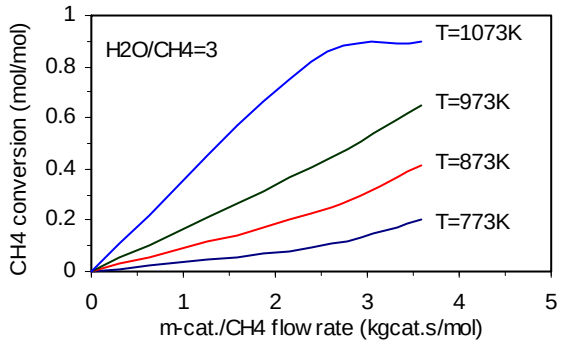

Figure 6: Total CH_4 conversion versus resident time at various catalyst temperatures (H_2O/CH_4=3)

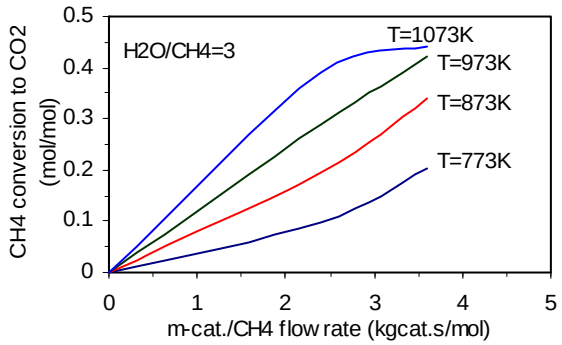

Figure 7: Mole fraction of CH_4 conversion to CO_2 versus resident time at various catalyst temperatures (H_2O/CH_4=3)

Once functions (17) to (21) have been determined, the rates of total CH_4 conversion and CH_4 conversion to other gases in the reforming process can be found by differentiating these functions with respect to resident time, $m_{\text{cat}} / F_{\text{CH}_4}^{in}$.

$$r_{CH_4} = \frac{dx_{CH_4}}{d(m_{cat} / F_{CH_4}^{in})} = a_1 + 2a_2\left(\frac{m_{cat}}{F_{CH_4}^{in}}\right) + 3a_3\left(\frac{m_{cat}}{F_{CH_4}^{in}}\right)^2 \quad (22)$$

$$r_{CO_2} = \frac{dx_{CO_2}}{d(m_{cat} / F_{CH_4}^{in})} = b_1 + 2b_2\left(\frac{m_{cat}}{F_{CH_4}^{in}}\right) + 3b_3\left(\frac{m_{cat}}{F_{CH_4}^{in}}\right)^2 \quad (23)$$

$$r_{H_2O} = \frac{dx_{H_2O}}{d(m_{cat} / F_{CH_4}^{in})} = c_1 + 2c_2\left(\frac{m_{cat}}{F_{CH_4}^{in}}\right) + 3c_3\left(\frac{m_{cat}}{F_{CH_4}^{in}}\right)^2 \quad (24)$$

$$r_{CO} = \frac{dx_{CO}}{d(m_{cat} / F_{CH_4}^{in})} = d_1 + 2d_2\left(\frac{m_{cat}}{F_{CH_4}^{in}}\right) + 3d_3\left(\frac{m_{cat}}{F_{CH_4}^{in}}\right)^2 \quad (25)$$

$$r_{H_2} = \frac{dx_{H_2}}{d(m_{cat} / F_{CH_4}^{in})} = e_1 + 2e_2\left(\frac{m_{cat}}{F_{CH_4}^{in}}\right) + 3e_3\left(\frac{m_{cat}}{F_{CH_4}^{in}}\right)^2 \quad (26)$$

As the kinetic mechanisms in methane steam reforming are very complicated and not covered within the scope of this research, the detailed analysis of possible mechanisms can be referred to [133, 134].

In this study, the methane steam reforming surface mechanism is adopted from Xu and Froment's work [133]. According to their work, the reaction mechanism is as follows:

- H_2O reacts with surface nickel atoms, yielding adsorbed oxygen and gaseous hydrogen.
- The H_2 formed is directly released into the gas stream and/or the gaseous H_2 is in equilibrium with adsorbed H and H_2.
- Methane is adsorbed on surface nickel atoms. The adsorbed methane either reacts with the adsorbed oxygen or dissociates to form chemisorbed radicals, CH_x, with x = 0 to 3.
- The adsorbed oxygen and the carbon-containing radicals react to form chemisorbed formaldehyde (CH_2O), formyl radical (CHO), CO or CO_2.
- CO and CO_2 are formed out of CHO and CH_2O species.

The corresponding forms of reaction rate expressions for reaction 2, 3 and 4 in Table 2 for methane steam reforming over nickel catalyst are shown as follows: [133].

$$R_2 = \frac{k_1}{p_{H_2}^{2.5}}\left(p_{CH_4}p_{H_2O} - \frac{p_{H_2}^3 p_{CO}}{K_{e1}}\right)\times\frac{1}{Q_r^2} \tag{27}$$

$$R_3 = \frac{k_2}{p_{H_2}}\left(p_{CO}p_{H_2O} - \frac{p_{H_2}p_{CO_2}}{K_{e2}}\right)\times\frac{1}{Q_r^2} \tag{28}$$

$$R_4 = \frac{k_3}{p_{H_2}^{3.5}}\left(p_{CH_4}p_{H_2O}^2 - \frac{p_{H_2}^4 p_{CO_2}}{K_{e3}}\right)\times\frac{1}{Q_r^2} \tag{29}$$

where $Q_r = 1 + K_{CO}p_{CO} + K_{H_2}p_{H_2} + K_{CH_4}p_{CH_4} + \frac{K_{H_2O}p_{H_2O}}{p_{H_2}}$

where R_j (kmol/kgcat·h) is the rate of reaction j (j = 1 – 3); p_{CH_4}, p_{O_2}, *etc.* are, respectively, partial pressures of gas species CH_4, O_2, *etc.*, k_j is a kinetic rate constant of reaction j and described as $k_j = k_{oj} \times e^{\frac{-E_j}{RT}}$, k_{oj} is a constant, E_j (kJ/kmol) is the activation energy, R = 8.314 kJ/kmol·K is the universal gas constant; T (K) is the gas temperature in the reaction zone; K_{ej} is the equilibrium constant of reaction j (j = 1 – 3); K_i is the adsorption constant of species i (i = CO, H_2, CH_4, H_2O) and expressed as $K_i = K_{oi} \times e^{\frac{-\Delta H_i}{RT}}$; K_{oi} is a constant; ΔH_i is the adsorption enthalpy of species i (kJ/kmol). k_j and K_i can be found by fitting the kinetic model to the experimental data.

Reaction rates for the consumption of CH_4 and formation of CO and CO_2 are obtained from following relations:

$$r_{CH_4} = -(R_2 + R_4) \tag{30}$$

$$r_{CO_2} = R_3 + R_4 \tag{31}$$

$$r_{H_2O} = -(R_2 + R_3 + 2R_4) \tag{32}$$

$$r_{CO} = R_2 - R_3 \tag{33}$$

$$r_{H_2} = 3R_2 + R_3 + 4R_4 \tag{34}$$

Substituting these rate equations (30) to (34) into equations (22) to (26) for the data treatment with different input and operating conditions, k_j and K_i in equations (27) to (29) can be computed by numerical iteration.

The relationship between temperature and calculated kinetic rate and adsorption parameters of k_j and K_i are depicted in figure 8 and figure 9, respectively. Based on these data, the constants k_{oj}, K_{oi}, activation energy E_j and adsorption enthalpy ΔH_i can be determined from the following relations:

$$E_j = \frac{\ln(k_{j(1)} / k_{j(2)})}{\frac{1}{T_{(2)}} - \frac{1}{T_{(1)}}} \times R\,; \qquad k_{oj} = k_{j(1)} e^{\frac{E_j}{RT_{(1)}}} \tag{35}$$

$$K_{oi} = K_{i(1)} e^{\frac{\Delta H_i}{RT_{(1)}}}\,; \qquad \Delta H_i = \frac{\ln(K_{i(1)} / K_{i(2)})}{\frac{1}{T_{(2)}} - \frac{1}{T_{(1)}}} \times R \tag{36}$$

where the subscript indices $_{(1)}$ and $_{(2)}$ are two arbitrary points (1) and (2) on the curves $\ln(k_j)$ and $\ln(K_i)$ against $1/T$ in figure 8 and 9.

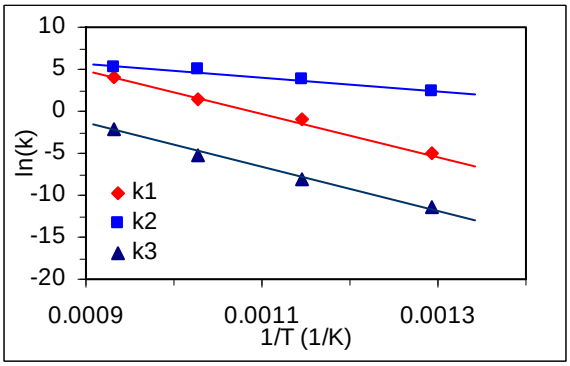

Figure 8: Temperature dependence of rate constants from 773 to 1073 K

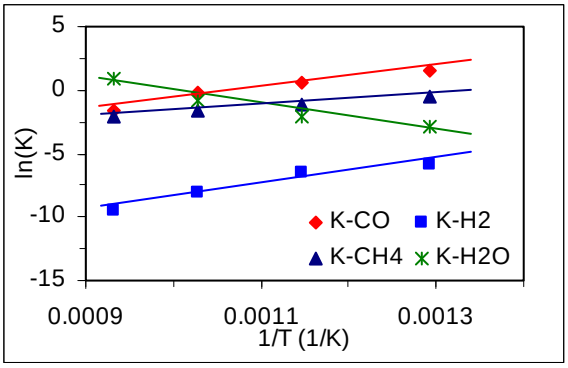

Figure 9: Temperature dependence of adsorption parameters from 773 to 1073 K

The calculated kinetic rate and adsorption constants in equations (27) to (29) based on the current experimental data are shown in Tables 3 to 5.

Table 3 Equilibrium constants (STR)

Reaction	Equilibrium constant K_{ej}
2	$5.75\times10^{12}\times e^{-11476/T}$ (bar^2)
3	$1.26\times10^{-2}\times e^{4639/T}$
4	$7.24\times10^{10}\times e^{-21646/T}$ (bar^2)

Table 4 Kinetic parameters (STR)

Reaction	k_{0j} (mol/kgcat·s)	E_j (J/mol)
2	9.048×10^{11} bar $^{0.5}$	209500
3	5.43×10^{5} bar $^{-1}$	70200
4	2.14×10^{9} bar $^{0.5}$	211500

Table 5 Adsorption constants (STR)

Species	K_{oi} (bar $^{-1}$)	ΔH_i (J/mol)
CH_4	1.995×10^{-3}	-36650
CO	8.11×10^{-5}	-70230
H_2	7.05×10^{-9}	-82550
H_2O	1.68×10^{4} bar	85770

4.2.2 Kinetics of Partial Oxidation

Similarly, for the partial oxidation, the overall conversion rate of methane to water and other gases in the reforming process can be determined from experiments. The relationship between the conversion rates and resident times can be expressed in the form of polynomial function as follows:

$$x_i = a_0 + a_1\left(\frac{m_{cat}}{F^{in}_{CH_4}}\right) + a_2\left(\frac{m_{cat}}{F^{in}_{CH_4}}\right)^2 + a_3\left(\frac{m_{cat}}{F^{in}_{CH_4}}\right)^3 \quad (37)$$

where

x_i is mole of i species (i=CH_4, O_2, CO_2, H_2O, CO and H_2) conversion per mole of inlet CH_4, mol

m_{cat} is mass of catalyst, kg

$F_{CH_4}^{in}$ is inlet molar flow rate of CH_4, mol/s

$m_{cat} / F_{CH_4}^{in}$ is resident time, kgcat·s/mol

a_i (i=0-3) are constants

Under assumption (1), the boundary conditions of the above equation can be set as:

At $m_{cat} / F_{CH_4}^{in} = 0$, $x_i = 0$ (i=CH_4, O_2, CO_2, H_2O, CO and H_2)

With the boundary conditions incorporated, the constants, a_i (i=0-3), for each specie in equation (37) can be determined by fitting these functions to the experimental data under different resident time and methane conversion rate.

Once the constants in (37) have been determined, the rates of total CH_4 conversion and CH_4 conversion to other gases in the reforming process can be found by differentiating these functions with respect to resident time, $m_{cat} / F_{CH_4}^{in}$.

$$r_i = \frac{dx_{CH_4}}{d(m_{cat} / F_{CH_4}^{in})} = a_1 + 2a_2\left(\frac{m_{cat}}{F_{CH_4}^{in}}\right) + 3a_3\left(\frac{m_{cat}}{F_{CH_4}^{in}}\right)^2 \quad (38)$$

where r_i is rates of conversion of i species (i=CH_4, O_2, CO_2, H_2O, CO and H_2) per mole of inlet CH_4, kgcat·s/mol

As the kinetic mechanisms in methane partial oxidation are very complicated and not covered within the scope of this research, the detailed analysis of possible mechanisms can be referred to [135, 136].

In this study, we had adopted the Langmuir-Hinshelwood model from Ma *et al.* [136]. According to their work, the reaction mechanism is as follows:

- O_2 reacts with surface nickel atoms, yielding adsorbed oxygen.
- Methane is adsorbed on surface nickel atoms. The adsorbed methane either reacts with the adsorbed oxygen or dissociates to form chemisorbed radicals, CH_x, with x = 0 to 3.
- The adsorbed oxygen and the carbon-containing radicals react to form chemisorbed formaldehyde (CH_2O), formyl radical (CHO), OH, CO or CO_2.
- CO, CO_2, H_2 and H_2O are formed out of CHO and CH_2O species.

The corresponding forms of reaction rate expressions for reaction 1, 2, 3, 4 in Table 2 for methane partial oxidation over nickel catalyst are shown as follows: [136].

$$R_1 = \frac{k_1 p_{CH_4} p_{O_2}^{1/2}}{\left(1 + K_{CH_4}^{C} p_{CH_4} + K_{O_2}^{C} p_{O_2}^{1/2}\right)^2} \tag{39}$$

$$R_2 = \frac{k_2}{p_{H_2}^{2.5}} \left(p_{CH_4} p_{H_2O} - \frac{p_{H_2}^3 p_{CO}}{K_{e1}} \right) \times \frac{1}{Q_r^2} \tag{40}$$

$$R_3 = \frac{k_3}{p_{H_2}} \left(p_{CO} p_{H_2O} - \frac{p_{H_2} p_{CO_2}}{K_{e2}} \right) \times \frac{1}{Q_r^2} \tag{41}$$

$$R_4 = \frac{k_4}{p_{H_2}^{3.5}}\left(p_{CH_4}p_{H_2O}^2 - \frac{p_{H_2}^4 p_{CO_2}}{K_{e3}}\right)\times\frac{1}{Q_r^2} \tag{42}$$

$$Q_r = 1 + K_{CO}p_{CO} + K_{H_2}p_{H_2} + K_{CH_4}p_{CH_4} + \frac{K_{H_2O}p_{H_2O}}{p_{H_2}}$$

Reaction rates for the consumption of CH_4 and formation of CO and CO_2 are obtained from following relations.

$$r_{CH_4} = -(R_1 + R_2 + R_4) \tag{43}$$

$$r_{O_2} = -2R_1 \tag{44}$$

$$r_{CO_2} = R_1 + R_3 + R_4 \tag{45}$$

$$r_{H_2O} = 2R_1 - R_2 - R_3 - 2R_4 \tag{46}$$

$$r_{CO} = R_2 - R_3 \tag{47}$$

$$r_{H_2} = 3R_2 + R_3 + 4R_4 \tag{48}$$

Substituting these rate equations (43) to (48) into equation (38) for different species and data treatment with different input and operating conditions, k_j and K_i in equations (39) to (42) can be solved by numerical iteration.

Based on the experimental data, the constants k_{oj}, K_{oi}, activation energy E_j and adsorption enthalpy ΔH_i can be determined from the following relations:

$$k_{oj} = k_j e^{\frac{E_j}{RT}}; \qquad E_j = \frac{\ln(k_{j(1)} / k_{j(2)})}{\frac{1}{T_{(2)}} - \frac{1}{T_{(1)}}} \times R \tag{49}$$

$$K_{oi} = K_i e^{\frac{\Delta H_i}{RT}}; \qquad \Delta H_i = \frac{\ln(K_{i(1)} / K_{i(2)})}{\frac{1}{T_{(2)}} - \frac{1}{T_{(1)}}} \times R \tag{50}$$

where the subscript indices $_{(1)}$ and $_{(2)}$ are the reference points (1) and (2) on the curves $\ln(k_j)$ and $\ln(K_i)$ against $1/T$, which are chosen at $1/T_{(1)}= 1/1073$ and $1/T_{(2)}=1/773$.

The calculated kinetic rate and adsorption constants in equations (39) to (42) based on the current experimental data are shown in Tables 6 to 8.

Table 6 Equilibrium constants (POX)

Reaction	Equilibrium constant K_{ej}
2	$5.75\times10^{12} \times e^{-11476/T}$ (bar^2)
3	$1.26\times10^{-2} \times e^{4639/T}$
4	$7.24\times10^{10} \times e^{-21646/T}$ (bar^2)

Table 7 Kinetic parameters (POX)

Reaction	k_{0j} (mol/kgcat·s)	E_j (J/mol)
1	3.287×10^{2} bar $^{-1.5}$	204000
2	4.225×10^{11} bar $^{0.5}$	240100
3	1.955×10^{5} bar $^{-1}$	67130
4	1.02×10^{9} bar $^{0.5}$	243900

Table 8 Adsorption constants (POX)

Species	K_{oi} (bar $^{-1}$)	ΔH_i (J/mol)
CH_4 (Combustion)	2.02×10^{-3}	30800
O_2 (Combustion)	7.4×10^{-5}	-36330
CH_4	6.65×10^{-4}	-38280
CO	8.23×10^{-5}	-70650
H_2	6.12×10^{-9}	-82900
H_2O	1.77×10^{4}	88680

4.2.3 Kinetics of Autothermal

As mentioned in the earlier section, ATR is a combination of POX and STR under thermal-neutral condition. Therefore, the kinetic for reaction 1 is obtained from performing methane POX while the kinetics for reaction 2 to 4 are extracted from methane STR. The POX and STR mechanism is adopted from Ma *et al.* [136] and Xu *et al.* [133], respectively.

The corresponding forms of reaction rate expressions for reaction 1, 2, 3, 4 in Table 2 for methane autothermal reforming over nickel catalyst are shown as follows:

$$R_1 = \frac{k_1 p_{CH_4} p_{O_2}^{1/2}}{\left(1 + K_{CH_4}^{C} p_{CH_4} + K_{O_2}^{C} p_{O_2}^{1/2}\right)^2} \quad (51)$$

$$R_2 = \frac{k_2}{p_{H_2}^{2.5}}\left(p_{CH_4}p_{H_2O} - \frac{p_{H_2}^3 p_{CO}}{K_{e1}}\right)\times\frac{1}{Q_r^2} \tag{52}$$

$$R_3 = \frac{k_3}{p_{H_2}}\left(p_{CO}p_{H_2O} - \frac{p_{H_2}p_{CO_2}}{K_{e2}}\right)\times\frac{1}{Q_r^2} \tag{53}$$

$$R_4 = \frac{k_4}{p_{H_2}^{3.5}}\left(p_{CH_4}p_{H_2O}^2 - \frac{p_{H_2}^4 p_{CO_2}}{K_{e3}}\right)\times\frac{1}{Q_r^2} \tag{54}$$

$$Q_r = 1 + K_{CO}p_{CO} + K_{H_2}p_{H_2} + K_{CH_4}p_{CH_4} + \frac{K_{H_2O}p_{H_2O}}{p_{H_2}}$$

Reaction rates for the consumption of CH_4 and formation of the products are obtained from following relations.

$$r_{CH_4} = -(R_1 + R_2 + R_4) \tag{55}$$

$$r_{O_2} = -2R_1 \tag{56}$$

$$r_{CO_2} = R_1 + R_3 + R_4 \tag{57}$$

$$r_{H_2O} = 2R_1 - R_2 - R_3 - 2R_4 \tag{58}$$

$$r_{CO} = R_2 - R_3 \tag{59}$$

$$r_{H_2} = 3R_2 + R_3 + 4R_4 \tag{60}$$

The calculated kinetic rate and adsorption constants in equations (51) to (54) based on the current experimental data are shown in Tables 9 to 11.

Table 9 Equilibrium constants (ATR)

Reaction	Equilibrium constant K_{ej}
2	$5.75\times10^{12}\times e^{-11476/T}$ (bar^2)
3	$1.26\times10^{-2}\times e^{4639/T}$
4	$7.24\times10^{10}\times e^{-21646/T}$ (bar^2)

Table 10 Kinetic parameters (ATR)

Reaction	k_{oj} (mol/kgcat·s)	E_j (J/mol)
1	3.287×10^{2} $bar^{-1.5}$	204000
2	9.048×10^{11} $bar^{0.5}$	209500
3	5.43×10^{5} bar^{-1}	70200
4	2.14×10^{9} $bar^{0.5}$	211500

Table 11 Adsorption constants (ATR)

Species	K_{oi} (bar^{-1})	ΔH_i (J/mol)
CH_4 (Combustion)	2.02×10^{-3}	30800
O_2 (Combustion)	7.4×10^{-5}	-36330
CH_4	1.995×10^{-3}	-36650
CO	8.11×10^{-5}	-70230
H_2	7.05×10^{-9}	-82550
H_2O	1.68×10^{4}	85770

4.2.4 Kinetics of Water Gas Shift

In low temperature WGS, the surface mechanism of the reaction is described as follows [71, 137-142]:

- CO and H_2O are adsorbed on the catalyst surface and form an intermediate that results in desorbed hydrogen and CO_2; this mechanism is also known as adsorptive mechanism:

$$H_2O + CO \rightarrow CO_{(ads)} + H_2O_{(ads)} \rightarrow [\text{int}*] \rightarrow CO_{2(ads)} + H_{2(ads)} \rightarrow CO_2 + H_2$$

The surface mechanism for low temperature WGS was obtained from the work of Choi and Stenger [71]. The rate expression adopted to describe the WGS surface mechanism, assuming that the surface reaction is rate controlling, is expressed as follows:

$$r_{CO} = k\left(\frac{P_{H_2O}P_{CO} - P_{H_2}p_{CO_2}/K_{eq}}{\left(1 + K_1P_{CO} + K_2P_{H_2O} + K_3P_{CO_2} + K_4P_{H_2}\right)^2}\right) \quad (61)$$

where $K_{eq} = \exp\left(\frac{5693.5}{T} + 1.077\ln T + 5.44\times10^{-4}T - 1.125\times10^{-7}T^2 - \frac{49170}{T^2} - 13.148\right)$

The procedure to determine the kinetic rate and adsorption constant of WGS is similar to the procedure shown in the previous sections for determining the kinetic rates of POX and STR except that CO is the only specie considered.

The calculated kinetic rate and adsorption constants in Eq. (61) based on the current WGS experimental data are shown in Tables 12 and 13.

Table 12 Kinetic parameter (WGS)

Reaction	k (mol/kgcat · s)	E (J/mol)
1	748.824 bar $^{-2}$	53821

Table 13 Adsorption constants (WGS)

Species	K_{oi} (bar $^{-1}$)	ΔH_i (J/mol)
CO_2	0.036	-9795
CO	2.222	23616
H_2	2.197×10^{-5}	-63540
H_2O	2.006×10^{-5}	-66104

4.2.5 2-D unsteady autothermal reformer model

A schematic layout of the reactor used in this study is shown in figure 10. The reactor is cylindrical in shape, 30 mm in diameter and 200 mm in length, filled with catalysts (either spherical sulfided nickel or spherical platinum).

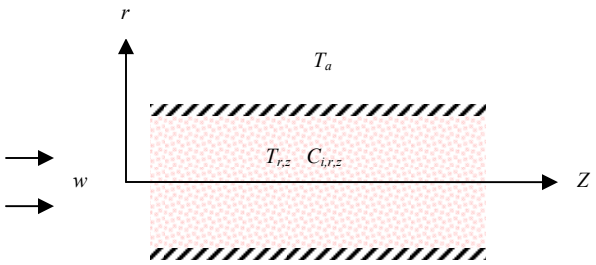

Figure 10: Schematic layout of a 2-D reactor

To simplify the model, one may assume that the gas flow in the reactor is uniform and apply 1-D model for the reactor. However, the radial dispersion of the gas flow due to catalyst and the radial heat transfer due to heat loss through the wall of the reactor may have some effects on the overall reforming performance. To take these effects into account of the modelling work, a 2-D reactor model is more appropriate to describe the reforming behaviour for the above mentioned conditions.

Other effects such as the non-plug flow gas velocity profile, the catalyst porosity profile and the diffusion of gases into and out of the porous catalyst pallets are also included in the kinetic model to make the simulation model closer to reality.

With assumptions (2) and (3) mentioned previously, the governing equations, initial conditions and boundary conditions are as follows [143, 144]:

Energy equation for gas phase,

$$\varepsilon(r)\rho_g C_{p,g}\frac{\partial T_g}{\partial t} + \rho C_{p,g} w(r)\frac{\partial T_g}{\partial z} = h_t A_s\left(T_s - T_g\right) \qquad (62)$$

Concentration equation for gas phase,

$$\varepsilon(r)\frac{\partial C_{\mathrm{g}}}{\partial t}+w(r)\frac{\partial C_{\mathrm{g}}}{\partial z}=\frac{1}{r}\frac{\partial}{\partial r}\left[D_{\mathrm{r}}(r)r\frac{\partial C_{\mathrm{g}}}{\partial r}\right]+D_{\mathrm{ax}}(r)\frac{\partial^{2}C_{\mathrm{g}}}{\partial z^{2}}+h_{\mathrm{m}}A_{\mathrm{s}}\left(C_{\mathrm{c}}-C_{\mathrm{g}}\right) \tag{63}$$

Energy equation for catalyst phase,

$$\left(1-\varepsilon(r)\right)\rho_{\mathrm{c}}C_{\mathrm{p,c}}\frac{\partial T_{\mathrm{c}}}{\partial t}=\frac{1}{r}\frac{\partial}{\partial r}\left[K_{\mathrm{r}}(r)r\frac{\partial T_{\mathrm{c}}}{\partial r}\right]+K_{\mathrm{ax}}(r)\frac{\partial^{2}T_{\mathrm{c}}}{\partial z^{2}}$$

$$+h_{\mathrm{t}}A_{\mathrm{s}}\left(T_{\mathrm{g}}-T_{\mathrm{c}}\right)+\rho_{\mathrm{c}}\sum_{j=1}^{4}\left(-\Delta H_{j}\right)\eta_{\mathrm{eff}}R_{j} \tag{64}$$

Relationship between bulk gas and gas at catalyst surface,

$$\eta_{\mathrm{eff}}\rho_{\mathrm{c}}\,r\frac{M}{\rho_{\mathrm{g}}}=h_{\mathrm{m}}A_{\mathrm{s}}\left(C_{\mathrm{g}}-C_{\mathrm{c}}\right) \tag{65}$$

where subscript g denotes gas

subscript c denotes catalyst

subscript *i* denotes gas species

subscript *j* denotes reaction index

subscript *r* denotes radial direction

subscript *ax* denotes axial direction

T is temperature, K

C is concentration, mol/m^3

C_p is specific heats, J/kgK

D_r is radial diffusion, eq. (69), m^2/s

D_{ax} is axial diffusion, eq. (70), m^2/s

$\varepsilon(r)$ is porosity profile, eq. (67)

ρ is density, kg/m^3

K_r is radial thermal conductivity, eq. (71), W/mk

K_{ax} is radial thermal conductivity, eq. (72), W/mk

h_m is mass transfer coefficient, eq. (77), m/s

h_t is heat transfer coefficient, eq. (73), W/m^2K

ΔH is the heat of reaction, -ve sign to denote exothermic reaction, J/mol

$\dot{r}$ is reaction rate, mol/s

A_s is geometric surface area per volume of catalyst = 155 m^2/m^3

η_{eff} is the effectiveness factor, eq. (68)

$w(r)$ is the velocity function, eq. (66)

r is radial coordinates, m

z is axial coordinates, m

The initial conditions and boundary conditions for the above equations are as follows:

For energy equation of gas phase,

$$T_{\mathrm{g}}(z,0)=T_{\mathrm{in}}$$

$$T_{\mathrm{g}}(0,t)=T_{\mathrm{in}}$$

$$\left.\frac{\partial T_{\mathrm{g}}}{\partial z}\right|_{z=\mathrm{L}}=0$$

For concentration equation of gas phase,

$$C_{gi}(z,0)=C_{gi,\mathrm{in}}$$

$$C_{gi}(0,t)=C_{gi,\mathrm{in}}$$

$$\left.\frac{\partial C_{\mathrm{g}}}{\partial z}\right|_{z=\mathrm{L}}=0$$

$$\left.\frac{\partial C_{\mathrm{g}}}{\partial r}\right|_{r=R}=0$$

For energy equation of catalyst phase,

$$T_{\mathrm{s}}(z,0)=T_{\mathrm{s,set}}$$

$$\left.\frac{\partial T_{\mathrm{s}}}{\partial z}\right|_{z=0}=0$$

$$\left.\frac{\partial T_s}{\partial z}\right|_{z=L} = 0$$

$$K_r \left.\frac{\partial T_s}{\partial r}\right|_{r=R} = \alpha\left(T_s - T_a\right)$$

where α is the overall heat transfer coefficient through the reactor wall, eq. (86), W/m^{2}K

In this model, finite difference method (FDM) is used to solve equations (62) to (65). The scheme used for solving the equations is Forward-Time Centered-Space (FTCS), which is an explicit scheme, $O\left(\Delta t + \Delta z^2\right)$ and conditionally stable [145].

As it is conditionally stable, it is subjected to the following stability criteria:

$$d = \frac{\alpha \Delta t}{\Delta z^2} \le \frac{1}{2}$$

$$c = \frac{w \Delta t}{\Delta z} \le 1$$

The stability criteria must be strictly adhered to in order to obtain accurate transient results and for the scheme to remain stable. As such, there are checks to ensure that gas velocity (w) , thermal (α) and mass (D_m) diffusivity are below thresholds which would cause the stability criteria to be violated.

The auxiliary equations required for computing equations (62) to (65) are given below:

With reference to Papageorgiou *et al.* [95] and Borkink *et al.* [97], the velocity function, *w(r)*, which is used to define the velocity profile of the gas stream, is expressed as:

$$w(r)=\begin{cases} w_o \times (1+\sin(\pi r_{step})) & \text{for } (\Delta r \times r_{step}) < (\Phi/2 - 2d_p) \\ w_o \times (1+1.5\sin(\pi r_{step})) & \text{for } (\Delta r \times r_{step}) > (\Phi/2 - 2d_p) \end{cases} \quad (66)$$

where w_o is the local superficial velocity, m/s

Δr is the step change in radial direction, m

Φ is diameter of the reactor, m

d_p is the diameter of catalyst pellet, m

r_{step} is the number of steps in radial direction

Incorporating the velocity function, *w(r)*, will accommodate for the non plug-flow gas stream in the reactor due to non-homogenous catalyst packing.

Accordingly, the porosity profile in the cylindrical packed bed reactor can be expressed as [96, 100]:

$$\varepsilon(r)=\begin{cases} \varepsilon_{min} + (1-\varepsilon_{min})R'^2 & \text{for } R' < 0 \\ \varepsilon_o + (\varepsilon_{min} - \varepsilon_o)\exp\left(\frac{R'}{10}\cos\left(\frac{\pi R'}{0.876}\right)\right) & \text{for } R' > 0 \end{cases} \quad (67)$$

where

$$\chi_{min} = 0.5\left[\Phi - \left((\Phi - d_p)^2 - d_p^2\right)^{0.5}\right], \text{ m}$$

Dimensionless radial coordinate, $R^{'} = \left(\frac{\Phi}{2} - r\right) \Big/ \chi_{\min} - 1$

Minimum void fraction, $\varepsilon_{\min} = 0.28$ for spheres smaller than 3.5mm

Void fraction at core of packed bed, $\varepsilon_{o} = 0.38$ for spheres smaller than 3.5mm

This would take the non-homogenous catalyst packing into consideration and thus, accounting for the non plug-flow gas stream.

The effectiveness factor, η_{eff}, which account for the effect of gas diffusion into and out of the catalyst, is determined by [146-148]:

$$\eta_{\text{eff}} = \frac{3}{\phi^2}\left(\phi \coth \phi - 1\right) \Big/ \left(1 + \frac{1}{\text{Sh}}\left(\phi \coth \phi - 1\right)\right) \tag{68}$$

where Sh is Sherwood number expressed in equation (68)

Thiele modulus, $\phi = \Phi\sqrt{k^{"} A_s / D_m}$

$k^{"}$ is rate constant

D_m is combined Knudsen and ordinary diffusivity defined in equation (92), m^2/s

This is to take into consideration that the catalysts in the reactor are porous media. Some of the gases in the main stream will diffuse into the catalyst through the catalyst pores, where reactions will take place, and diffuse back into the main gas stream again.

Since this is a 2-D reactor model, the diffusion term needs to account for both radial and axial direction. The radial dispersion of the gas flow due to catalyst, D_r, is expressed as [149]:

$$D_r(r) = \delta_{bed} + \frac{1}{8}\left[1 + \frac{3}{(Pe_{o,c})^{0.5}}\right]^{-1} Pe_o \frac{w_c}{\overline{w_o}} f(R-r)\delta \qquad (69)$$

where $f(R-r) = \begin{cases} \left(\dfrac{R-r}{0.44d_p}\right)^2 & \text{for } 0 < R-r \le 0.44d_p \\ 1 & \text{for } 0.44d_p < R-r \le R \end{cases}$

w_c is superficial velocity, m/s

$\overline{w_o}$ is average superficial velocity, m/s

δ is diffusion coefficient, eq. (85), m^2/s

δ_{bed} is effective bed diffusion coefficient, m^2/s

$Pe_o = \dfrac{\overline{w_o} d_p}{\delta}$ (ratio of convective to diffusive term)

while axial diffusion of the gas, D_{ax}, is expressed as [149]:

$$D_{ax} = \delta_{bed} + \frac{Pe_o}{2}\delta \qquad (70)$$

Similarly, the conduction term needs to account for both radial and axial direction. The radial conduction in the catalyst bed, K_r, is determined by [149]:

$$K_r(r) = \lambda_{bed} + Pe_o \frac{w_c}{w_o} f(R-r)\lambda_f \tag{71}$$

where $$f(R-r) = \begin{cases} \left(\dfrac{R-r}{\left(0.44 + 4\exp\left(-\dfrac{\mathrm{Re_o}}{70}\right)\right)d_p} \right)^2 & \text{for } 0 < R-r \le \left(0.44 + 4\exp\left(-\mathrm{Re_o}/70\right)\right)d_p \\ 1 & \text{for } \left(0.44 + 4\exp\left(-\mathrm{Re_o}/70\right)\right)d_p < R-r \le R \end{cases}$$

$$\mathrm{Pe_o} = \frac{\overline{w_o} d_p \rho_f c_f}{\lambda_f}$$

λ_f is thermal conductivity of fluid, W/mk

λ_{bed} is thermal conductivity of bed, W/mk

while axial conduction of the catalyst bed, K_{ax}, is calculated by [149]:

$$K_{ax} = \lambda_{bed} + \frac{Pe_o}{2}\lambda_f \tag{72}$$

For heat transfer coefficient in eq. (62) and (64), it is expressed as:

$$h_t = \frac{\mathrm{Nu} \cdot \lambda_f}{\Phi} \tag{73}$$

The correlation for Nusselt number (ratio of convective to conductive terms), Nu, is obtained from Churchill [150], which is valid for $0 \le \mathrm{Pr} \le 10^6$ and $10 \le \mathrm{Re} \le 10^6$, spanning the laminar, transition and turbulent flow regimes. The Nusselt number is defined as:

$$(\mathrm{Nu})^{10} = (\mathrm{Nu}_l)^{10} + \left\{ \frac{e^{(2200-\mathrm{Re})/365}}{(\mathrm{Nu}_l)^2} + \frac{1}{(\mathrm{Nu}_t)^2} \right\}^{-5} \tag{74}$$

where $\mathrm{Nu}_t = \mathrm{Nu}_0 + \dfrac{0.079\left(f/2\right)^{0.5} \mathrm{Re}\,\mathrm{Pr}}{\left(1+\mathrm{Pr}^{4/5}\right)^{5/6}}$

$$\mathrm{Nu}_0 = 6.3$$

$$\mathrm{Nu}_l = 4.364$$

The Reynolds number (ratio of inertial to viscous forces) used in this model, Re, is computed as:

$$\mathrm{Re} = \frac{\rho w_o \Phi}{\mu} \tag{75}$$

where ρ is density of fluid, kg/m^3

μ is dynamic viscosity of fluid, Pa.s

w_o is local superficial velocity, m/s

and the Prandtl number (ratio of momentum to thermal diffusivity), Pr, is expressed as:

$$\mathrm{Pr} = \frac{\mu C_p}{\lambda_f} \tag{76}$$

For mass transfer coefficient in eq. (63) and (65), it is defined by:

$$h_m = \frac{\mathrm{Sh} \cdot D_m}{\Phi} \tag{77}$$

The Sherwood number (ratio of length-scale to the diffusive boundary layer thickness) for the above equation is as follows [151]:

$$\mathrm{Sh} = 0.023\,\mathrm{Re}^{0.5}\,\mathrm{Sc}^{1/3} \tag{78}$$

where the Schmidt number (ratio of momentum diffusivity to mass diffusivity), Sc, is expressed as:

$$Sc = \frac{\mu}{\rho D_m} \tag{79}$$

The mass diffusivity, D_m, used in this model considered the combined effects of Knudsen and binary ordinary diffusion. Ordinary diffusion occurs when the pore diameter of the material is large in comparison to the mean free path of the gas molecules. Conversely, molecular transport through pores that are small in comparison to the mean free path of the gas is regarded as Knudsen type of diffusion. For Knudsen diffusion, molecules collide more frequently with the pore walls than with other molecules. Upon collision, the atoms are instantly adsorbed onto the surface and are then desorbed in a diffused manner. As a result of frequent collisions with the wall of the pore, the transport of the molecule is impeded.

The Knudsen diffusion coefficient can be predicted from kinetic theory by relating the diameter of the pore and the mean free path of the gas by the following expression [152]:

$$D_{\mathrm{Ak}} = 97\bar{r}\sqrt{T/M_{\mathrm{A}}} \qquad (80)$$

where mean pore radius, $\bar{r} = \dfrac{2\varepsilon}{A_{\mathrm{s}}\rho_{\mathrm{b}}}$

ρ_{b} is the bulk density of the material

According to Chapman-Enskog theory of prediction [153], the ordinary diffusion coefficient is defined as follows:

$$D_{AB} = 0.000018583\left(\frac{1}{M_A} + \frac{1}{M_B}\right)^{0.5} \frac{T^{3/2}}{P\sigma_{AB}^2 \Omega_{D,AB}} \quad (81)$$

where M_A is the molecular weight of specie A

M_B is the molecular weight of specie B

σ_{AB} is the collision diameter, Å

P is pressure, atm

Ω_{AB} is the collision integral based on Lennard-Jones potential obtained from energy of molecular interaction, e_{AB}

The collision diameter in equation (71), σ_{AB}, is computed by:

$$\sigma_{AB} = \frac{(\sigma_A + \sigma_B)}{2} \quad (82)$$

To account for the tortuous path of the molecule rather than along the radial direction and the porosity of the catalyst, the Knudsen diffusion and ordinary diffusion is modified to become:

$$D_{Ak(eff)} = D_{Ak}\frac{\varepsilon}{\xi} \quad (83)$$

$$D_{AB(eff)} = D_{AB}\frac{\varepsilon}{\xi} \quad (84)$$

The resulting combined effect of Knudsen and ordinary diffusion is expressed as:

$$D_{\mathrm{m}} = \frac{1}{\frac{\xi}{\varepsilon}\left(\frac{1}{D_{\mathrm{AB(eff)}}} + \frac{1}{D_{\mathrm{Ak(eff)}}}\right)} \tag{85}$$

The overall heat transfer coefficient through the reactor wall, α, is determined from [154-156]:

$$\frac{1}{\alpha} = \frac{1}{h_{\mathrm{in}}} + \frac{b}{\lambda_{steel}} + \frac{1}{h_{\mathrm{out}}} \tag{86}$$

where b is the thickness of the wall, m

λ_{steel} is thermal conductivity of steel = 19 W/mk

internal heat transfer coefficient, $h_{in} = \frac{0.027 C_c \lambda_f}{\Phi}\left(\frac{\Phi w \rho_g}{\mu_g}\right)^{0.8}\left(\frac{\mu_g c_{pg}}{\lambda_f}\right)^{0.33}$, W/m^{2}K

external heat transfer coefficient, $h_{\mathrm{o}} = \frac{k_{\mathrm{a}}}{\Phi}\left(0.6 + \frac{0.387\mathrm{Ra}^{1/6}}{\left[1 + (0.559/\mathrm{Pr})^{9/16}\right]^{8/27}}\right)^2$, W/m^{2}K

The Rayleigh number (ratio of conduction to convection), Ra, in the above equation is defined as:

$$\mathrm{Ra} = \frac{g\beta}{\nu\lambda_{air}}(T_s - T_a)\Phi^3 \qquad (87)$$

where g is acceleration due to gravity = 9.812 m/s^2

β is thermal expansion coefficient = 0.0032418

λ_{air} is thermal conductivity of air = 0.0261 W/mk

ν is kinematic viscosity = 0.0000157 m/s

T_s is surface temperature, K

T_a is ambient temperature = 298 K

A flow process of the kinetic fuel reforming simulation program is shown in the following figure 11.

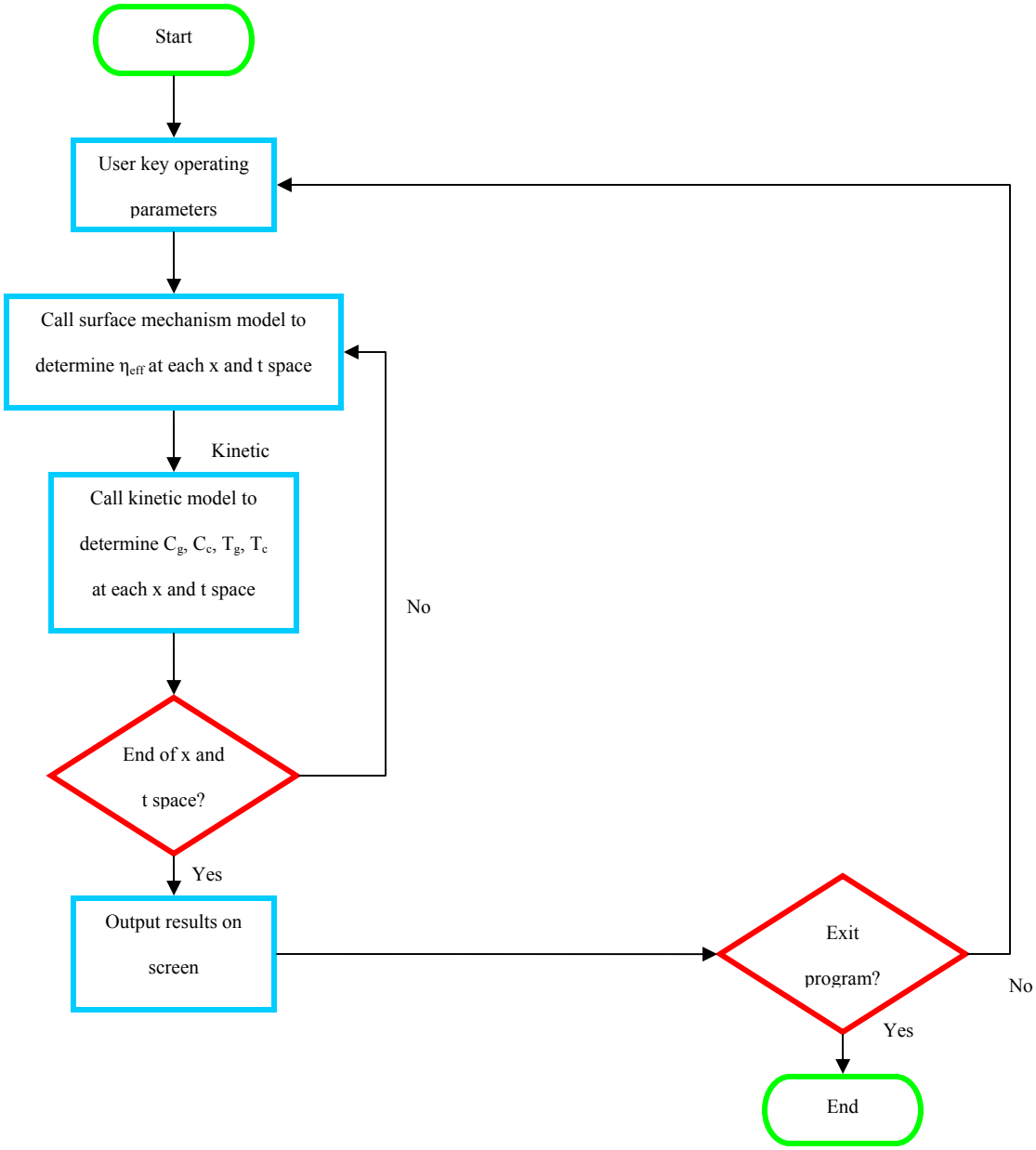

Figure 11: Process flow of kinetic fuel reforming program

The kinetic fuel reforming program, written in Visual Basic programming language, allows various operating variables such as gas inlet temperature, gas pressure, gas flow rate, molar air-fuel ratio and molar water-fuel ratio to be set. In addition to this, the

chemical kinetic model can be run with or without WGS reforming; if WGS reforming is selected, the user can specify the dimensions of the WGS reformer and whether it is insulated. After the variables and options have been set, the program begins to compute the partial pressure, concentration, radial and axial diffusive of each gas species and the radial and axial conductivity of the catalysts. The program also determines the heat and mass transfer coefficient between the gas and catalyst as well as the diffusion of gases into the porous catalysts. The final results of the chemical kinetic model are then displayed in numerical form on-screen.

4.2.6 Summary

Kinetic rates of ATR were abstracted from the massive POX and STR experiment data. These are applied in the simulation model, coupled with general energy and concentration equations, to determine the amount of gas products and temperatures. Additional considerations such as 1) gas diffusion in the catalysts, 2) velocity profile, and 3) porosity profile are also applied in the simulation model. With heat transfer along the wall and gas-to-wall heat transfer integrated into the 2D model, the simulation model is unique and comprehensive.

The kinetics parameters and constants of ATR and WGS reactions used in the simulation model are listed as follows:

Table 9 Equilibrium constants (ATR)

Reaction	Equilibrium constant K_{ej}	
2	$5.75\times10^{12}\times e^{-11476/T}$ (bar^2)	Adopted from STR
3	$1.26\times10^{-2}\times e^{4639/T}$	
4	$7.24\times10^{10}\times e^{-21646/T}$ (bar^2)	

Table 10 Kinetic parameters (ATR)

Reaction	k_{oj} (mol/kgcat·s)	E_j (J/mol)	
1	3.287×10^{2} bar$^{-1.5}$	204000	Adopted from POX
2	9.048×10^{11} bar$^{0.5}$	209500	Adopted from STR
3	5.43×10^{5} bar^{-1}	70200	
4	2.14×10^{9} bar$^{0.5}$	211500	

Table 11 Adsorption constants (ATR)

Species	K_{oi} (bar^{-1})	ΔH_i (J/mol)	
CH_4 (Combustion)	2.02×10^{-3}	30800	Adopted from POX
O_2 (Combustion)	7.4×10^{-5}	-36330	
CH_4	1.995×10^{-3}	-36650	Adopted from STR
CO	8.11×10^{-5}	-70230	
H_2	7.05×10^{-9}	-82550	
H_2O	1.68×10^{4}	85770	

Table 12 Kinetic parameter (WGS)

Reaction	k (mol/kgcat·s)	E (J/mol)
1	748.824 bar $^{-2}$	53821

Table 13 Adsorption constants (WGS)

Species	K_{oi} (bar $^{-1}$)	ΔH_i (J/mol)
CO_2	0.036	-9795
CO	2.222	23616
H_2	2.197×10^{-5}	-63540
H_2O	2.006×10^{-5}	-66104

5 Results

The results of the experimental works, chemical equilibrium model and kinetic model are presented in this section. The sequence of presentation is in this order: chemical equilibrium, experimental works and kinetic model, as results from equilibrium model can be used to size the reactor before its fabrication and subsequent experiments, using the in-house developed reactor, were carried out to extract the kinetics for the kinetic model.

5.1 Chemical Equilibrium Results

To show how the operating conditions affect the performance of each thermochemical reforming process, the results are presented in H_2/CO ratio, C number and H_2 yield as a function of operating conditions such as air-fuel ratio, water-fuel ratio, pressure and temperature. H_2/CO ratio is an indication of selectivity towards H_2 should CO be considered as a poison to the low-temperature fuel cell which has to be reduced to no more than 20 ppm by preferential oxidation method. It is important to reduce the CO level (or to achieve high H_2/CO ratio) in the reforming stage before entering gases clean up or purification. C number is defined as the amount of total "harmful" carbon in the reaction products which, in this study, refers to carbon and carbon monoxide. For reliable operation of reformers, the optimal operating conditions should be chosen under no carbon formation condition. H_2 yield refers to H_2 mole number produced per mole of CH_4

supply. In ATR case, it is an indication of the reformer's performance as ATR operates under thermal-neutral condition.

5.1.1 Partial oxidation

Figure 12 shows the H_2/CO ratio, C number and H_2 yield of POX at various temperature and pressure. At 900 K and 1atm, the selectivity towards H_2 increases dramatically with the decrease of AF ratio, especially at very low AF ratios. It reaches the minimum of 2.58 at AF ratio of 4; further increase in AF ratio from this point shows only marginally improvement in the selectivity. The C number declines steadily with increasing AF ratio with no carbon formation when AF ratio is above 4. The H_2 yield maintains at around 1.43 moles per mole of feedstock CH_4 supply in a wide range of AF ratio. Unfortunately, for AF above 4 where no carbon would form, the selectivity towards H_2 formation is low. It is obvious that, when the AF is below 4, the C number is mainly contributed by carbon as the CO decreases with decreasing AF ratio. Thus, the optimal AF ratio should be chosen at greater than and closer to 4.

At 900 K and 2 atm, the results show that with the increase of pressure, the selectivity towards H_2 formation increases, but both C number and H_2 yield decrease. The H_2 yield maintains at around 1.21 moles per mole of feedstock CH_4 supply in a wide range of AF ratio, indicating that the increase in selectivity when AF ratio decreases is due mainly to the decrease of CO. Compared to the case operating at 1 atm, increase in pressure would suppress the CO formation. Though the C number is in general lower than the case

operating at lower pressure, the carbon formation is actually higher with increased pressure at 900 K. For POX operating at 900 K and 2 atm, the AF ratio corresponding to no carbon formation is also above 4.

When compared the results at 1000 K and 1 atm to the case at 900 K and 1 atm, the selectivity towards H_2 is significantly lower, but both the C number and H_2 yield are moderately higher. The lower H_2 selectivity but improved H_2 yield means that the CO has increased significantly with the increase of temperature. For POX operating at 1000 K and 1 atm, the AF ratio corresponding to no carbon formation is above 3.

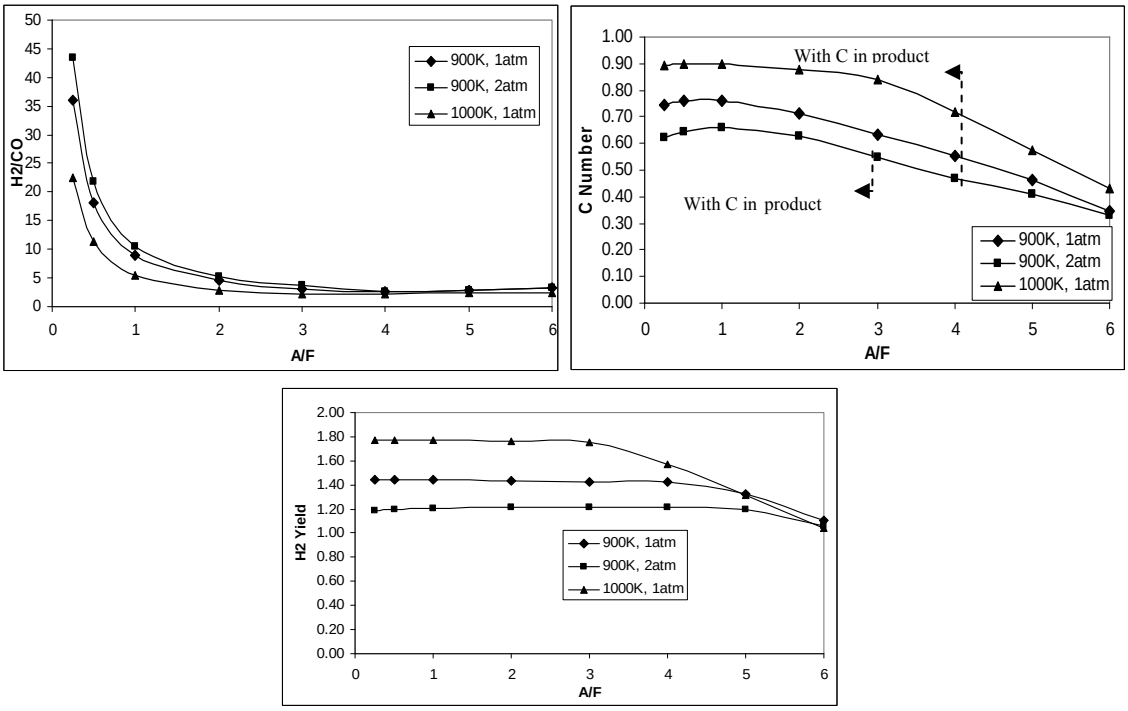

Figure 12: Selectivity, C number & H_2 yield of POX at different temperature and pressure

5.1.2 Steam reforming

Figure 13 shows the H_2/CO ratio, C number and H_2 yield of STR at various temperature and pressure. At 900 K and 1 atm, the results show that for WF ratio above 1.4, there is no carbon formation. The H_2/CO ratio and H_2 yield at WF ratio of 1.4 are 5.38 and 2.09, respectively. It is of great interest to note that, when WF ratio is greater than 1.4, both H_2/CO ratio and H_2 yield increase significantly, while C number decreases marginally. This indicates that if high H_2 concentration is a critical requirement and waste heat is available for reaction, operating the reformer at high WF ratio will bring the advantage of high H_2 but low CO mole numbers.

When compared the results at 900 K and 2 atm to the case at 1 atm, the selectivity towards H_2 is higher, while the C number and H_2 yield are lower. The increase of pressure does not affect threshold of the WF (=1.4), beyond which no carbon formation can occur and the C number remains almost unchanged. This indicates that the increase of H_2/CO ratio at WF ratio above 1.4 is due mainly to the decrease of CO. The H_2/CO ratio and H_2 yield at WF ratio of 1.4 are 6.29 and 1.67, respectively. If the size of the reformer is not a critical requirement to achieve a certain throughput, operating the reformer at nominal pressure (1 atm) will bring the advantage of higher H_2 yield.

When compared the results at 1000 K and 1 atm to the case at 900 K and 1 atm, the selectivity towards H_2 is lower, while both C number and H_2 yield are higher. The

increase of temperature would affect slightly the threshold of the WF (=1.3), beyond which no solid carbon would form. The H_2/CO ratio and H_2 yield at WF ratio of 1.3 are 3.64 and 2.75, respectively. Though CO mole number is higher with increased temperature, operating the reformer at high WF ratio shows a more pronounced decrease in CO. Thus, to gain the advantage of high H_2 yield with low CO mole number in the products, the reformer could operate at suitably high temperature and high WF ratio.

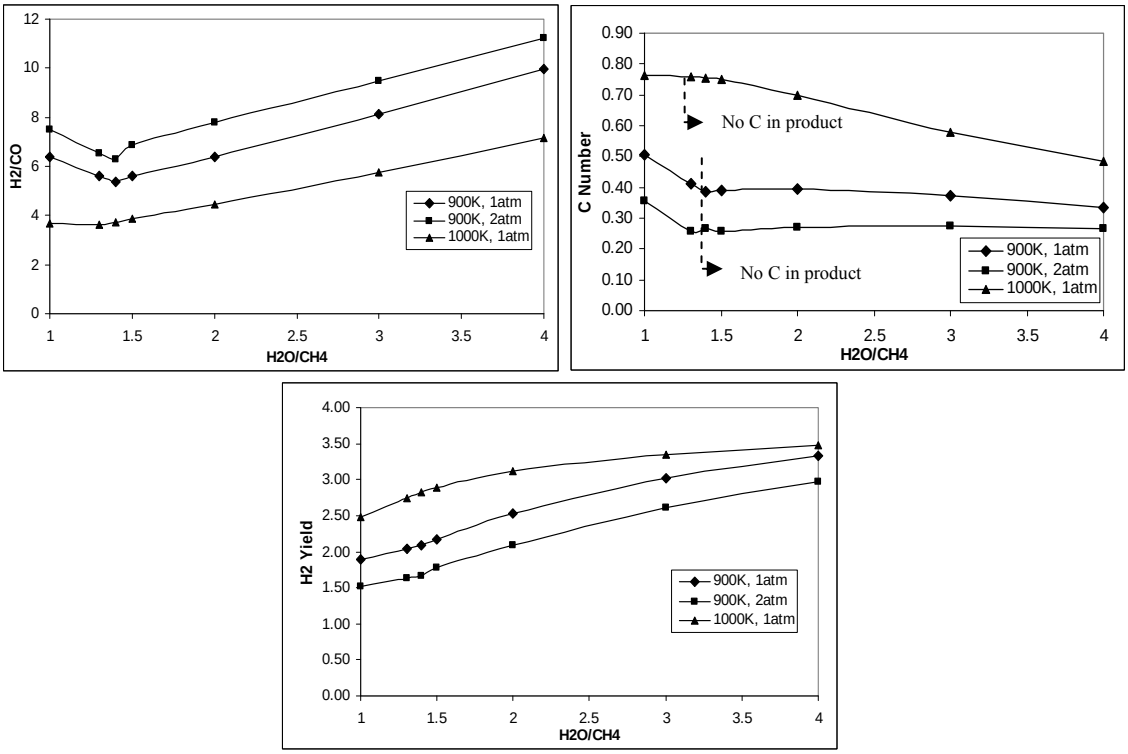

Figure 13: Selectivity, C number & H_2 number of STR at different temperature and pressure

5.1.3 Autothermal reforming

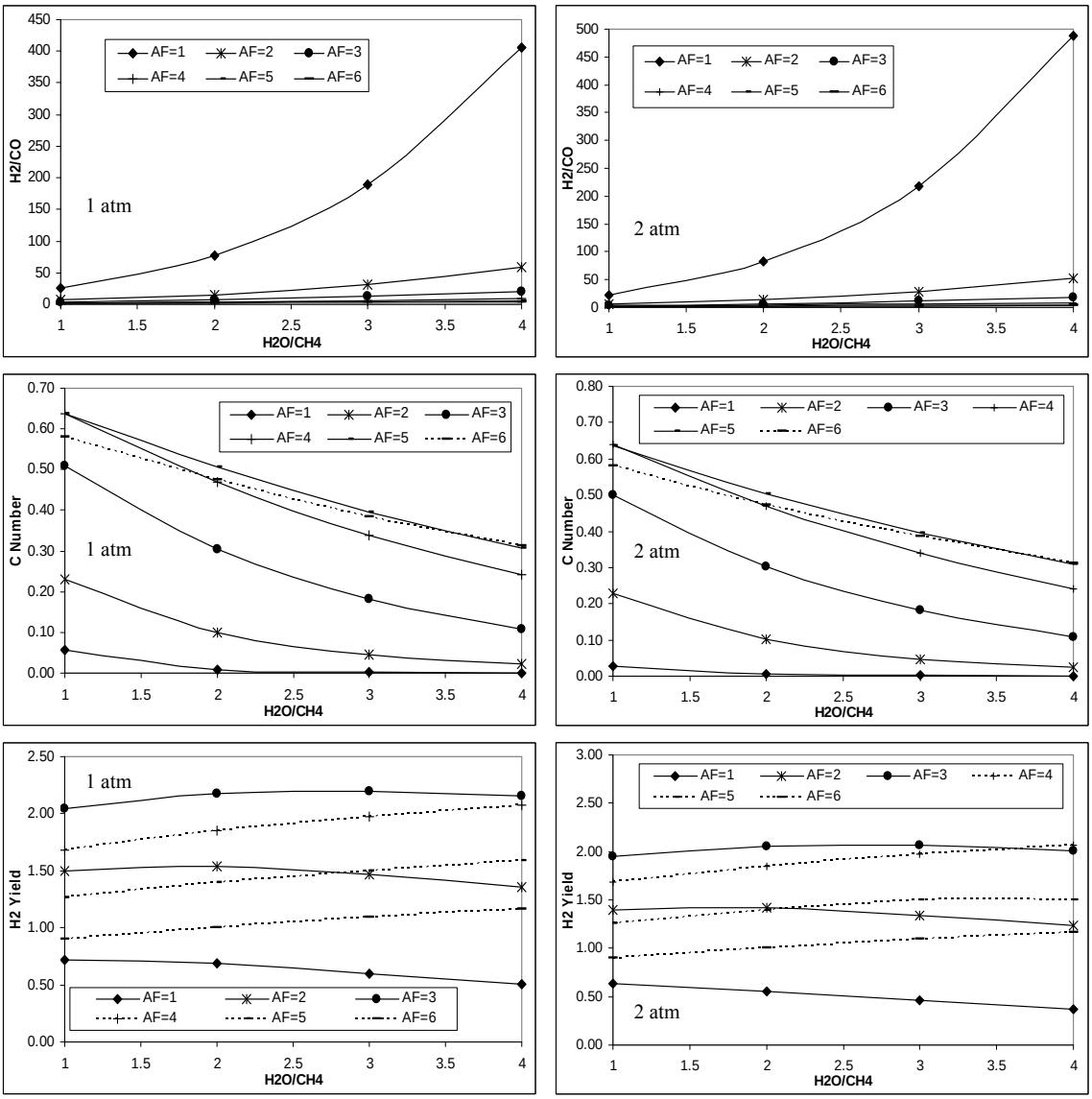

Figure 14: Selectivity, C number & H_2 number of ATR at 1 and 2 atm

Figure 14 shows the H_2/CO ratio, C number and H_2 yield of ATR at 1 and 2 atm, respectively, under thermal-neutral condition. Results at 1 atm show that H_2/CO ratio increases with increasing WF ratio but decreases with increasing AF ratio. This suggests

that operating the ATR at high WF and low AF ratios will bring the advantage of high selectivity towards H_2 yield. The C number decreases with increasing WF ratio, thus verifying that steam (water) is the key parameter in controlling CO. The C number exhibits a rising trend for AF ratio from 1 to 5 but slips lower at AF ratio of 6, which is due to the oxidation of CO to CO_2.

The results from H_2 yield figure show a mixed tendency of the impact of WF and AF ratios on the H_2/CO ratio. From AF ratio of 1 to 2, the gradient of H_2 yield is negative, a neutral gradient at AF ratio of 3 and a positive gradient from AF ratio of 4 onwards. This finding, together with the decreasing trend observed in C number figure, leads to the conclusion for ATR that increasing the amount of steam in the feedstock would not enhance the H_2 yield for AF ratio lower than 3, however, the selectivity towards H_2 is promoted especially at lower AF ratios.

Compared to the ATR operating at 1 atm, it is found that the selectivity towards H_2 at 2 atm is higher for AF ratio of 1, however, there is not much difference in selectivity for higher AF ratios. In addition, it is observed that H_2 yield is in general lower with the increase of pressure. Thus, operating ATR at higher pressure does not seem beneficial unless certain H_2 throughput is required.

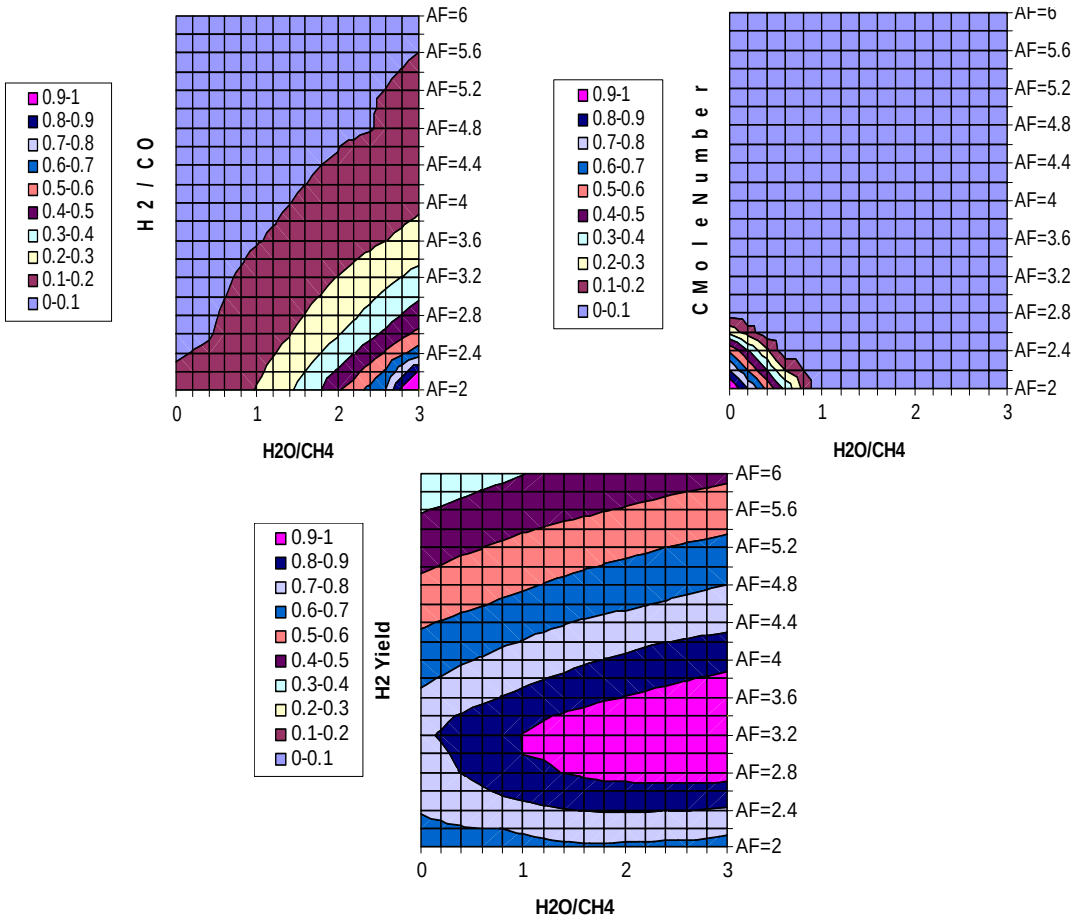

Figure 15: Contour graphs of selectivity, C mole number & H_2 mole number for ATR at 1 atm

Unlike POX or STR, it is rather difficult to determine the AF and WF ratios for achieving a trade-off between H_2 yield and selectivity towards H_2 for ATR under no carbon formation condition. Thus, the results in figure 14 are plotted in contour graphs with WF ratio range of 0 – 3 and AF ratio range of 2 – 6 as shown in figure 15. The C mole number is used instead of C Number, which would help to locate regions where no carbon is formed. In addition, taking the H_2/CO ratio of 31.31, C mole number of 0.38 and H_2 yield of 2.27 as the base values, all results are normalised by their respective base

value. It is with great interest to note that the highest H_2 yield (2.7<AF<3.9 and 1<WF<3) appears in the region where no solid carbon is formed, however, the selectivity towards H_2 corresponding to the highest H_2 yield is poor. As the highest H_2/CO ratio is located at high WF and low AF ratios, the AF ratio should be chosen at around 2.7 with WF ratio close to 3 for high H_2 yield.

5.1.4 Comparison of steam reforming, partial oxidation and autothermal reforming

In comparing the results between POX, STR and ATR from figure 12, 13, 14, and 15, respectively, it is evident that ATR has the overall highest selectivity to H_2 in the range of AF and WF ratios under study. This is followed by POX and STR. In addition, the results show that ATR is capable of producing low C number with no solid carbon in the products within the range of AF and WF ratio under study. Coupled with relatively high H_2 yield and thermally neutral, ATR is a superior process than STR and POX which is worth further investigation and analysis.

5.1.5 Water Gas Shift

5.1.5.1 Effect of Temperature

Figure 16 shows the effect of temperature on WGS in relative percentage change of CO and H_2 from 473K (baseline) to 523K with ATR operating at 1000K and 1 atm. The figure clearly shows that CO concentration increases with WGS temperature, which varies from 0.00% to 18.41% for different molar AF and WF ratios. In addition, H_2 concentration reduces up to 14.40% for various molar AF and WF ratios. The compositions remain unchanged for molar AF ratio below 3 and WF ratio of 1.

These results imply that increase of WGS temperature deteriorates the performance of WGS, i.e., low-temperature WGS is favoured by lower temperatures, subject to the lowest operating temperature of the WGS catalyst.

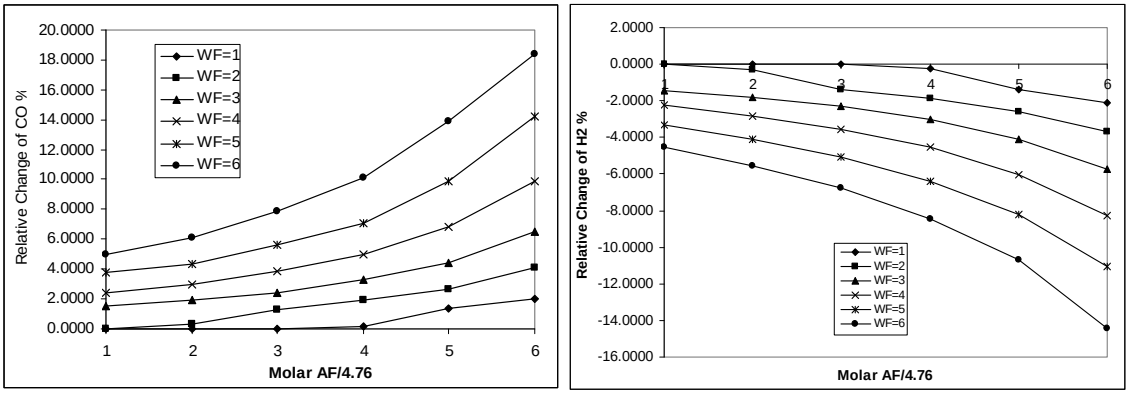

Figure 16: Effect of temperature on CO and H_2 yield (WGS)

5.1.6 Effect of combining autothermal reforming with water gas shift

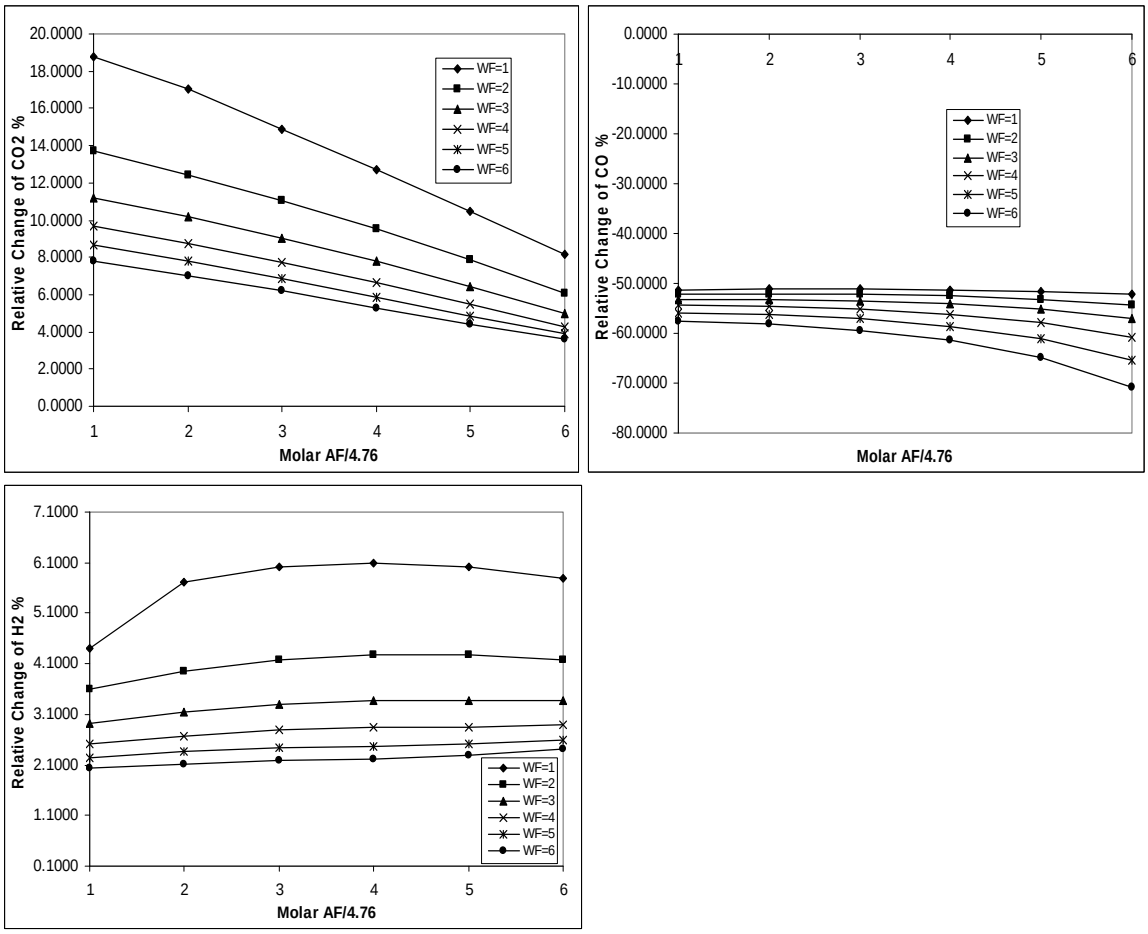

Figure 17: Effect of WGS (473K, 1atm) on ATR (800K, 1atm)

The figure above (Figure 17) presents the relative changes of CO_2, CO and H_2 when WGS is coupled with ATR running at 800K, 1atm. For various molar AF ratio and WF ratio, CO concentration can be potentially reduced from 51.10% up to 70.83%, while CO_2 is increased by 3.60% to 18.77%. Correspondingly, H_2 concentration can be increased by 2 to 6.1% after performing WGS.

5.1.7 Adiabatic reactor temperature

5.1.7.1 Autothermal reforming

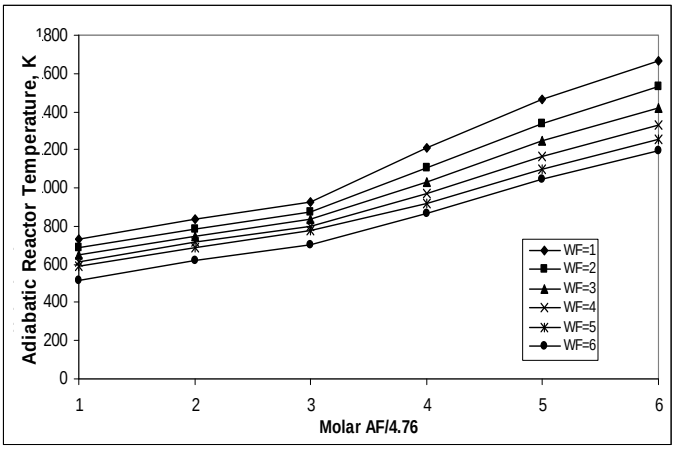

Figure 18: ATR adiabatic reactor temperature for various molar A/F and W/F ratio

Figure 18 presents the adiabatic reactor temperature under different molar AF and WF ratios. As seen from the figure, adiabatic reactor temperature increases with increasing molar AF ratio and decreases with increasing molar WF ratio. In addition, it is observed that the rate of increase of the adiabatic reactor temperature is lower for molar AF ratio 1 to 3 than for 3 to 6. This occurrence is due to the fact that the ATR reaction leans toward POX for molar AF ratio greater than 3 and shifts more to STR for molar AF less than 3. The exothermic nature of POX would cause the rate of adiabatic reactor temperature increment to be much higher than that for STR, which is endothermic in nature. The results also show that the change of molar AF ratios have greater influence on the adiabatic reactor temperatures than the change of molar WF ratios.

5.1.7.2 Water gas shift

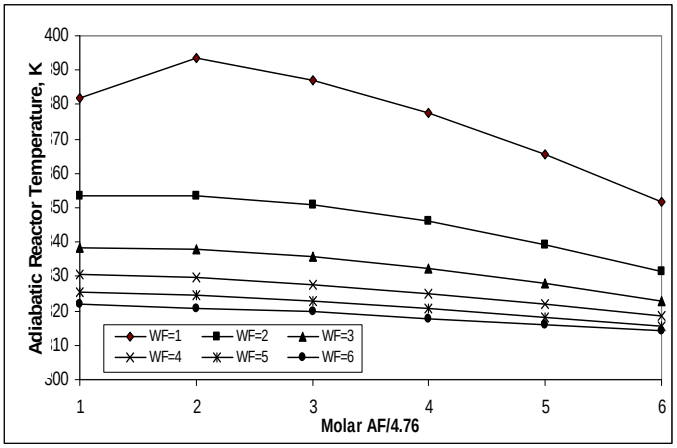

Figure 19: WGS adiabatic reactor temperature for various molar A/F and W/F ratio

The figure above (Figure 19) depicts the WGS adiabatic reactor temperature under different molar AF and molar WF ratios. In comparison with the ATR adiabatic reactor temperature, the WGS adiabatic reactor temperature has a rather flat profile. A peak WGS adiabatic reactor temperature of 393.5K is noted at molar AF ratio of 2 and molar WF ratio of 1. In general, it is found that the WGS adiabatic reactor temperature decreases with increasing molar AF and WF ratio.

5.1.7.3 Relationship between water gas shift adiabatic reactor temperature and water per carbon monoxide

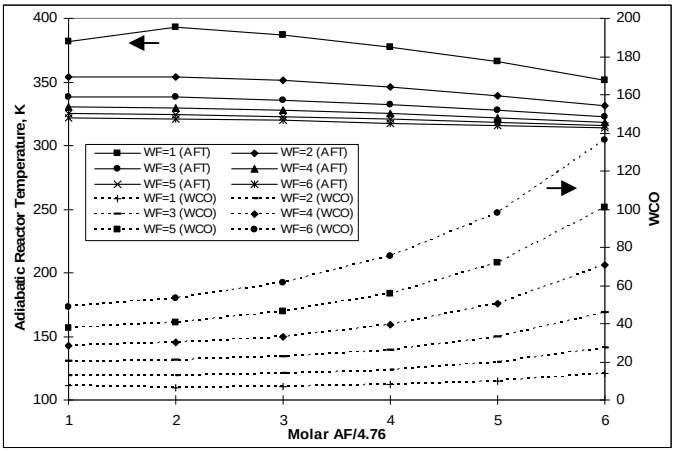

Figure 20: Relationship between adiabatic reactor temperature and WCO

Figure 20 shows the relationship of WGS adiabatic reactor temperature with WCO (mole of water per molar carbon monoxide). From the result, it is found that for WCO less than 40, there is significant difference in WGS adiabatic reactor temperature. This implies that there is a relationship between the adiabatic reactor temperature and the amount of CO present in the products of ATR. As the result suggests, the greater the amount of CO present in the reformed product, the higher is the WGS adiabatic reactor temperature. This is because WGS is slightly exothermic in nature. Conversely, the higher WCO implies that there is more water in the product and therefore dampen the temperature change.

5.1.8 Summary

Equilibrium studies on the STR, ATR, POX and WGS have been carried out to understand the processes better.

The results show that the optimal AF ratio for POX operating at 900 K should be chosen at greater than but closer to 4 where no carbon is formed. Although, for AF ratio above 4, the H_2 yield for POX is still high, but the H_2/CO ratio is low. The study also shows that the CO and H_2 decrease with the increase of pressure, but they increase with the increase of temperature.

For STR operating at a given temperature, high H_2/CO ratio and H_2 yield are observed at high WF ratios. If waste heat or external heat source is available and the H_2 concentration is not a critical requirement, the reformer should operate at suitably high WF ratio. More advantages can be obtained for STR operates at high temperature and high pressure, which could maintain the high H_2 yield and low CO as well as high H_2 throughput.

In ATR, the AF and WF range corresponding to high H_2 yield do not match with the high H_2/CO ratio. To achieve a high H_2 yield with reasonable H_2/CO ratio, the AF should be chosen at low end of the AF ratio range corresponding to the highest H_2 yield, while the WF ratio should be chosen at high end of the WF ratio corresponding to the highest H_2 yield. The study showed that H_2 yield is in general lower with the increase of pressure, though the H_2/CO ratio is improved especially at low AF ratios.

For WGS, the studies showed that low temperature and pressure favours the process. With integration of WGS into ATR process, the CO reduction can as high as 70.83% with the H_2 yield increase by up to 6.1%.

5.2 Experimental Results

5.2.1 Autothermal reforming

Extensive experiments have been conducted to determine the performance of the reformer developed in this project under different temperatures, WF and AF molar ratio and contact time (different CH_4 flow rates at the same catalyst loading). The results under the CH_4 flow rate of 120 l/hr are presented in figures 21 to 29, respectively, showing the effect of air to fuel ratio (AF) and molar water to fuel ratio (WF) on the performance of the autothermal reactor. Other experiment results will be placed in the appendix as they show similar trend to the results at 120 l/hr.

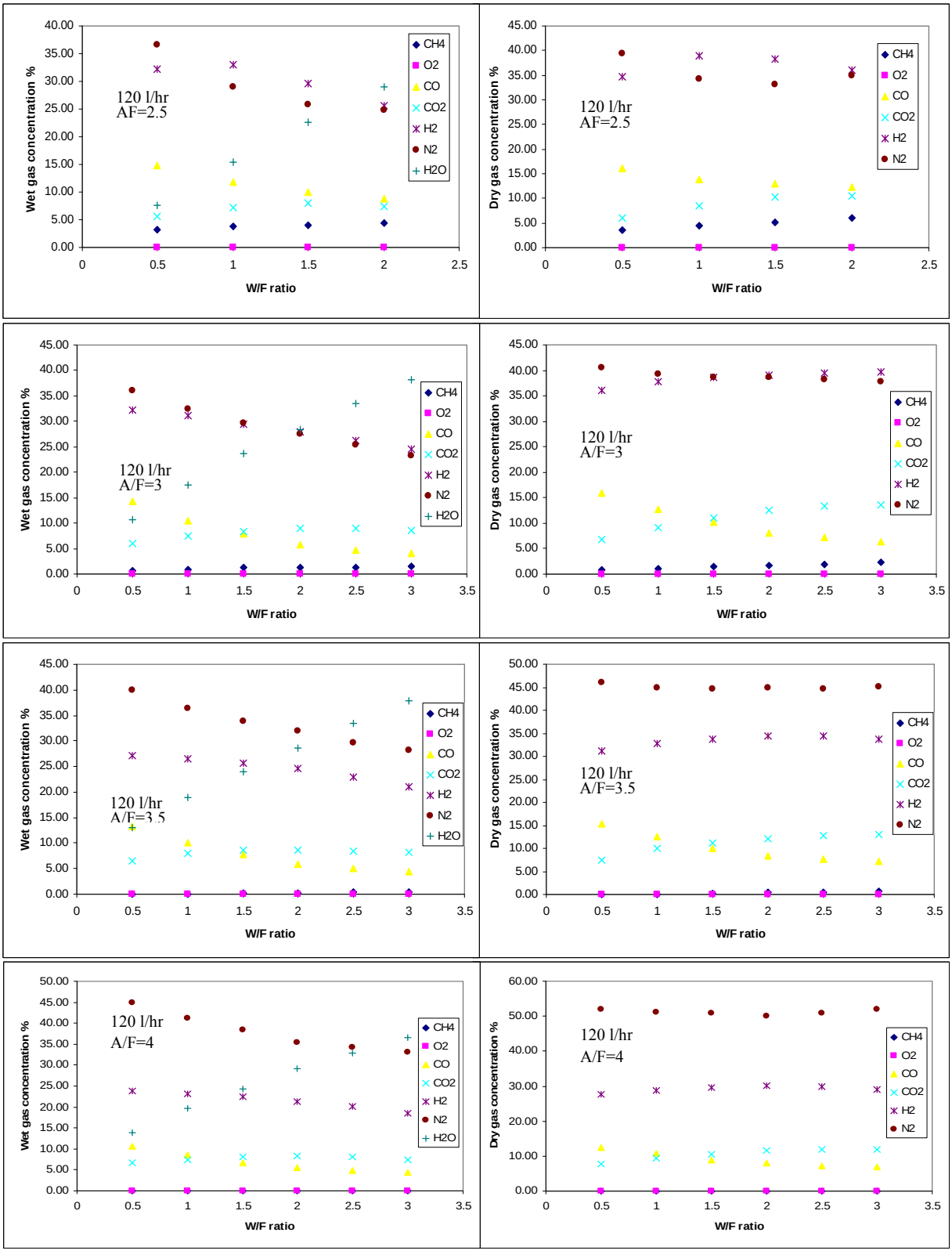

Figure 21: Wet and dry product gas concentrations at different WF and AF ratios (120 l/hr)

Figure 21 shows the variation of wet and dry product gas concentrations against a range of WF and AF ratios under methane flow rate of 120 l/hr. It can be seen from the results that within the range of WF ratio where the autothermal reactions sustains, the methane (CH_4) residue increases (CH_4 conversion decreases) marginally with increasing WF ratio. This is especially evident with the low AF ratios of 2.5 to 3.5; at high AF ratio of 4, the CH_4 is fully converted for all WF ratios. In addition, it is noted that carbon monoxide (CO) decreases gradually with increasing WF ratio while carbon dioxide (CO_2) increases. This is due to the improved water gas shift reaction. However, with the increase of WF ratio, the water vapour content in the wet product increases dramatically as the rate of steam reforming reaction is not directly proportional to the increase of WF ratio. As a result, the wet hydrogen (H_2) concentration decreases although its concentration increases in the dry product. Nitrogen (N_2) concentration, on the other hand, decreases mainly due to the increase of water vapour and CO_2 concentration in the products.

Figure 22 shows the CH_4 conversion efficiency at different AF and WF ratios under methane flow rate of 120 l/hr. The figures show that CH_4 conversion increases with increasing AF ratio and hits full conversion at about 3.5 AF ratio. The results also show that CH_4 conversion is higher at lower WF ratios. This is likely due to the higher reactor temperature at these operating points.

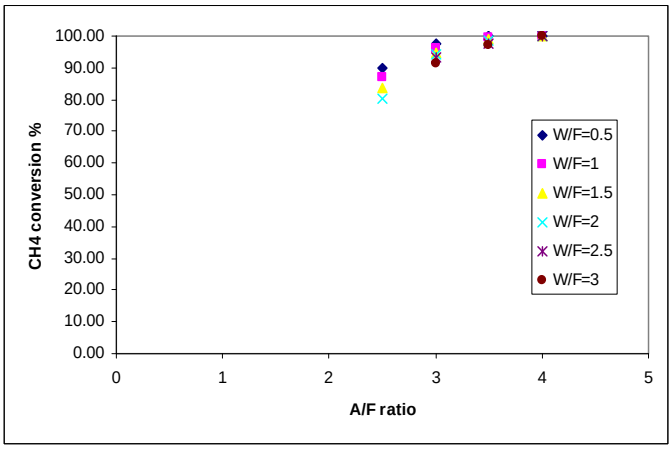

Figure 22: CH_4 conversion at different AF and WF ratios (120 l/hr)

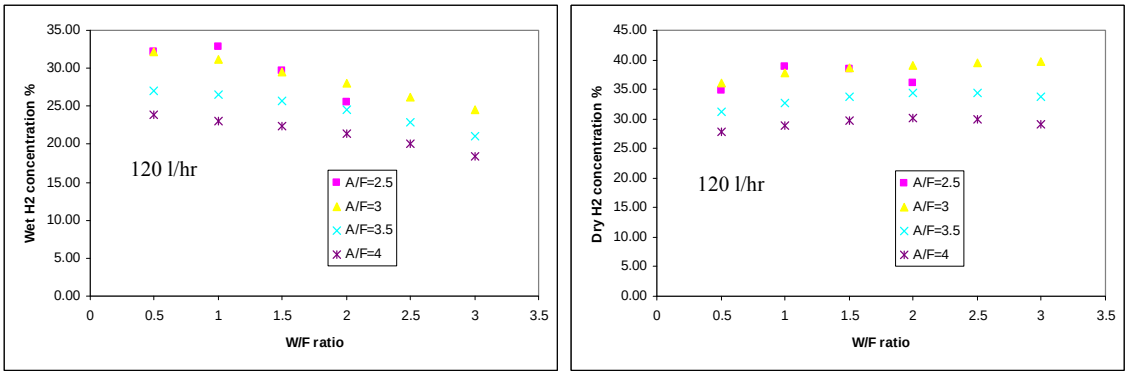

Figure 23: H_2 concentration at different AF and WF ratios (120 l/hr)

The relationship between H_2 concentration versus different AF and WF ratios at methane flow rate of 120 l/hr is shown in figure 23. It can be seen that the H_2 concentrations in both wet and dry products decrease with increasing AF ratio due to the increase of N_2 in the product. With a fixed AF ratio, the wet H_2 concentration decreases with increasing WF ratio within the studied range, at which the reactor can sustain autothermal reactions. However, this does not imply that the amount of H_2 produced decreases with increasing WF ratio; the increase of vapour content in the products is the reason behind this observed trend. With the water vapour removed from the products, it can be seen that the dry H_2 concentration increases with WF ratio as shown in the above figures. It is also

observed that the dry H_2 concentrations reached the peak at AF ratio of 3 at WF ratio of 2 to 3. In addition to these findings, the highest wet and dry H_2 concentration is noted at AF ratio of 2.5 and 3.

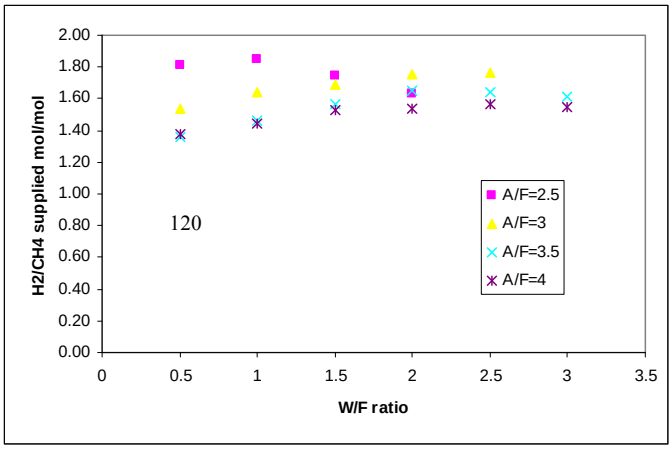

Figure 24: Mole of H_2 produced per mole of CH_4 supplied at different AF and WF ratios (120 l/hr)

The effect of WF and AF ratio on the amount of H_2 produced can be seen in figure 24 for methane flow rate of 120 l/hr. It shows a general trend that the mole number of H_2 produced per mole of CH_4 supplied increases with increasing WF ratio. With lower AF ratio, the maximum WF ratio at which the reactor can sustain autothermal reaction is lower due to lower heat release from exothermic reactions to vaporise water and compensate endothermic steam reforming reactions. This explains the trend observed at AF ratio of 2.5; the mole of H_2 produced reaches a peak at WF ratio of 1, which is the highest mole number of H_2 per mole of CH_4 supplied for all cases. Under this operating condition, the maximum H_2 yield is about 1.85 moles per mole of CH_4 supplied; wet and dry H_2 concentrations reach 32.92% and 38.89%, respectively. For other AF ratios, the peak occurs around WF ratio of 2 to 3.

For the effects of AF at all flow rates, it is generally noted that high AF ratio (in this case AF=4) is detrimental to the mole number of H_2 produced per mole of CH_4 supplied. The likely reason for this is because POX is more dominant than STR at this AF range, hence, less H_2 is produced.

The variations of CO concentrations and CO produced against AF and WF ratios are shown in figure 25 and 26 for methane flow rate of 120 l/hr. It can be seen that both wet and dry CO concentrations and mole of CO produced per mole number of CH_4 supplied drastically decrease with increasing WF ratio. This is due to the increase of water gas shift reaction in the total reaction. The effect of AF ratio on CO concentration is similar to that of H_2 concentration mentioned previously.

It is observed that CO concentrations at AF ratios greater than 3 with WF ratio above 2 do not differ significantly. This could be the limitation of the high temperature WGS reaction at these operating conditions.

At methane flow rate of 120 l/hr with AF ratio of 4 and WF of 3, the wet CO concentration is as low as 4.44%, dry CO concentration is 7%, and CO produced is as low as 0.37 mole per mole of CH_4 supplied.

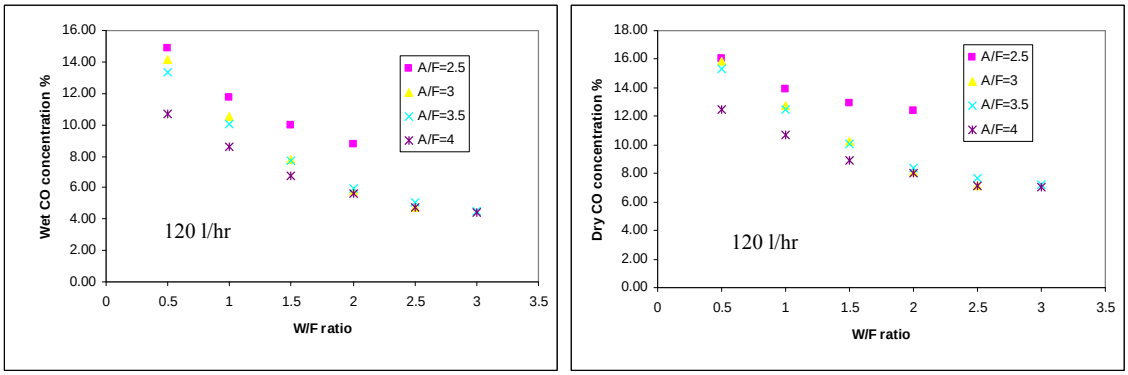

Figure 25: Wet and dry CO concentration at different AF and WF ratios (120 l/hr)

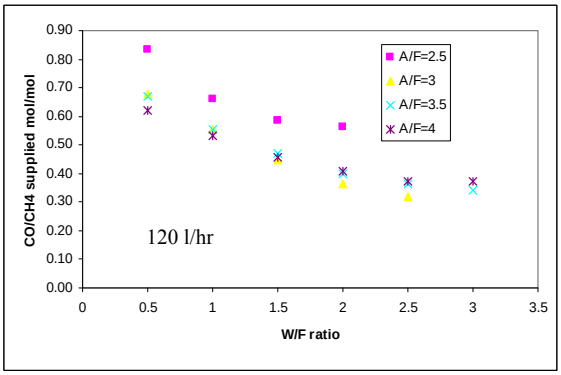

Figure 26: Mole of CO produced per mole of CH_4 supplied at different AF and WF ratios (120 l/hr)

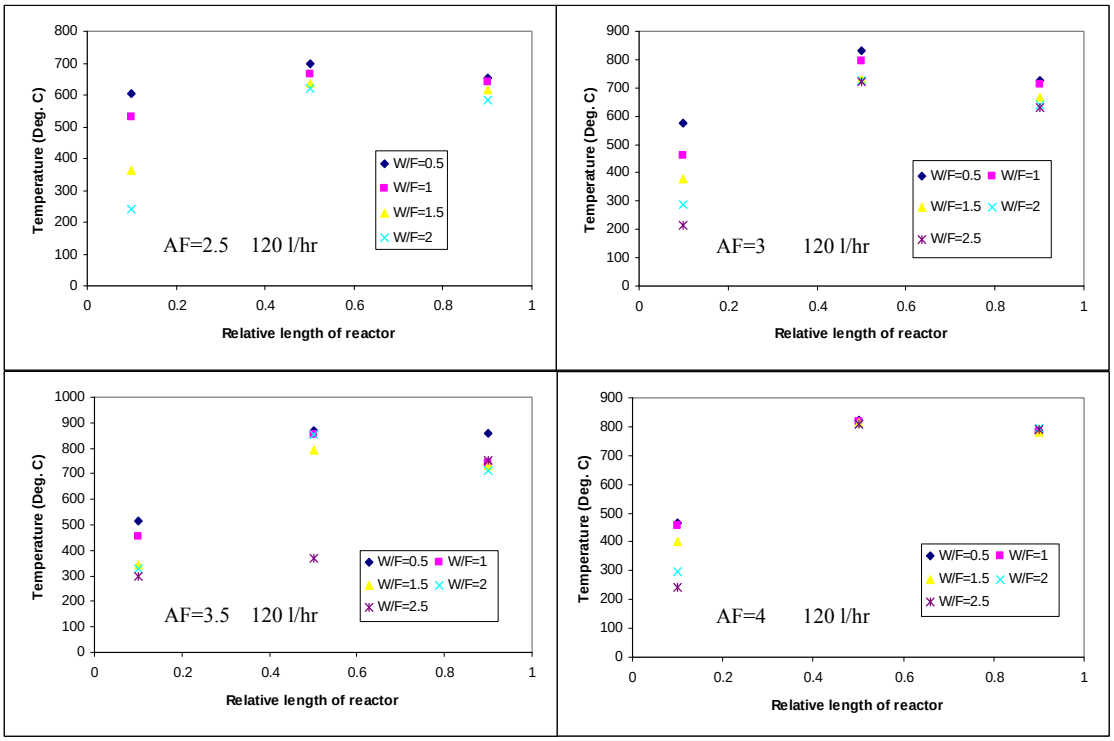

Figure 27: Catalyst temperature along reactor at different AF and WF ratios (120 l/hr)

The distribution of catalyst temperatures in the reactor at different AF and WF ratios are presented in figures 27 for methane flow rate of 120 l/hr. It can be seen that in general the catalyst temperature is lowest in the front part, highest in the middle part and lower in the rear part of the reactor. This can be explained as that the front part is cooled by the inlet mixture of low temperature; the middle part is heated by heat release from the total oxidation of methane while in the rear part the endothermic steam reforming reaction is prominent. Increasing WF ratio leads to more cooling of the front part, causing the temperature in this area to decrease. As a result, more total oxidation reaction of CH_4 shifts towards the rear end, resulting in increased temperature there. At a fixed WF ratio, the increase of AF ratio means increasing of CH_4 oxidation rate and heat release, and hence the reactor temperature increases.

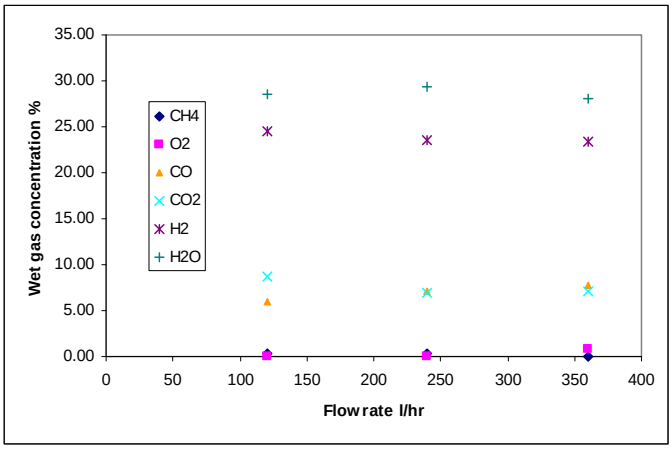

Figure 28: Wet gas product concentration at different CH_4 flow rate (AF=3.5 WF=2)

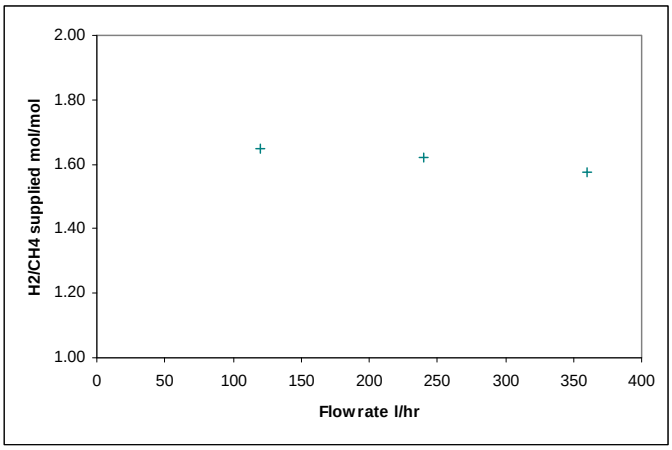

Figure 29: Mole of H_2 produced per mole of CH_4 supplied at different flow rate (AF=3.5 WF=2)

The effect of inlet CH_4 flow rate on the reforming performance are presented in figures 28 and 29, which show the gas concentrations in wet basis and mole number of H_2 produced per mole of CH_4 supplied, respectively, at AF ratio of 3.5 and WF ratio of 2. It can be seen that the increase in rate of CH_4 supply causes a decrease in the H_2 concentration and hence, a drop in CH_4 conversion, this results in a decrease in the mole number of H_2 produced per mole of CH_4 supplied. The experimental results also show that CO concentration increases with increasing CH_4 flow rate. These phenomena are mainly due to the change of temperature profile of the reactor. With the flow rate of supply gas exceeding a limit value, higher flow rate will cause more cooling of the front part of the reactor, resulting in more inactive catalyst and hence lower chemical reaction rate there.

Based on the results presented and discussed above, it can be concluded that based on the current reactor configuration, there is an optimum operating conditions for each flow rate to achieve high H_2 yield, high CH_4 conversion and high flow of H_2 produced per mole of

CH_4 supplied. In general, AF ratio of 2.5-3 and WF ratio of 2-2.5 under the flow rate of CH_4 supply of 120-240 l/hr should satisfy all the criteria. Under these feeding conditions, CH_4 conversion can reach 80.20-94.05%; H_2 concentration can reach 35.56%-42.78% in dry basis (25.57%-28.22% in wet basis); H_2 flow can reach 1.54-1.77 mole per mole of CH_4 supplied; CO concentration can be as low as 7.11%-12.38% in dry basis (5.87%-7.86% in wet basis) and CO flow can be as low as 0.32-0.86 mole per mole of CH_4 feeding. Under the mentioned feeding condition, the maximum catalyst temperature does not exceed 728˚C.

5.2.1.1 Validation of autothermal predicted results

As mentioned in the previous section, the kinetics of the ATR were extracted from numerous experiment data conducted and used in the kinetic model for prediction.

Figure 30 shows a typical case of predicted and ATR experiment results at 3.5 AF for methane flow rate of 120 l/hr while figure 31 depicts the comparison of the predicted results versus ATR experiment results for methane flow rate of 120 and 240 l/hr. As seen from these figures, the predicted results match the experiment results fairly well with a maximum error of 7% and a mean difference of ±2.47%. This implies that the kinetic model can be confidently used for parametric studies.

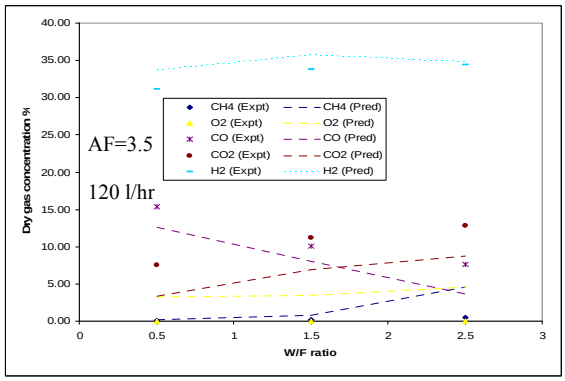

Figure 30: Kinetic model predicted results compared with experiment results for ATR at 3.5 AF

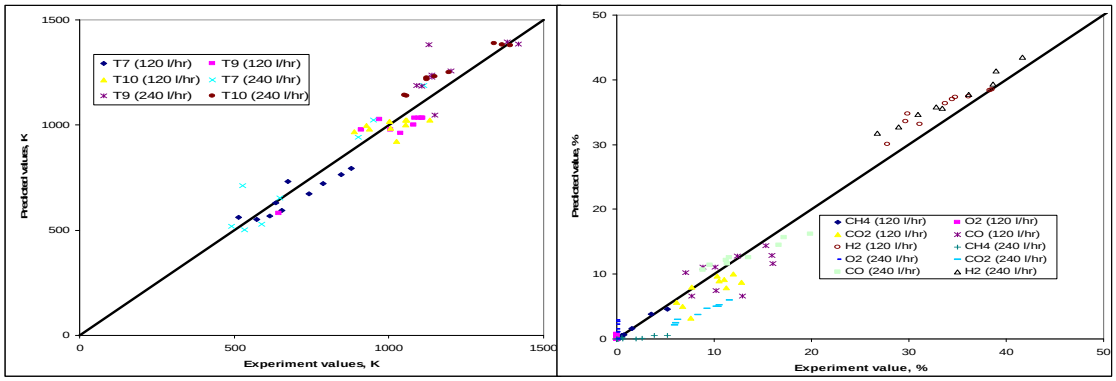

Figure 31: Kinetic model predicted results against experiment results for ATR

5.2.2 Water gas shift

Extensive experiments have been conducted to determine the performance of WGS reactor under different temperatures, molar H_2O/CO ratio and contact time (different CO flow rates at the same catalyst loading).

The results under different temperature are presented in figures 32, showing the effect of flow rates and molar H_2O/CO ratio on the performance of the WGS reactor. From these experimental results, one can see that the WGS reaction increases (that is, greater CO reduction and H_2 increase with increasing H_2O/CO ratios. It is also noted that there are

only marginal difference in CO reduction and H_2 increase between medium flow rate and high flow rate, with better CO reduction and H_2 increase at medium flow rate. These results indicate that there is an optimum flow rate and temperature for WGS reaction. In addition, it is observed that the conversion of WGS reaction for different temperatures at low flow rate is lower by 5-45 % for H_2 increment and 2-45 % for CO reduction than that at medium and high flow rate. From these results, one can deduce that the change in temperature has greater positive effect on WGS reaction carried out at low flow rate.

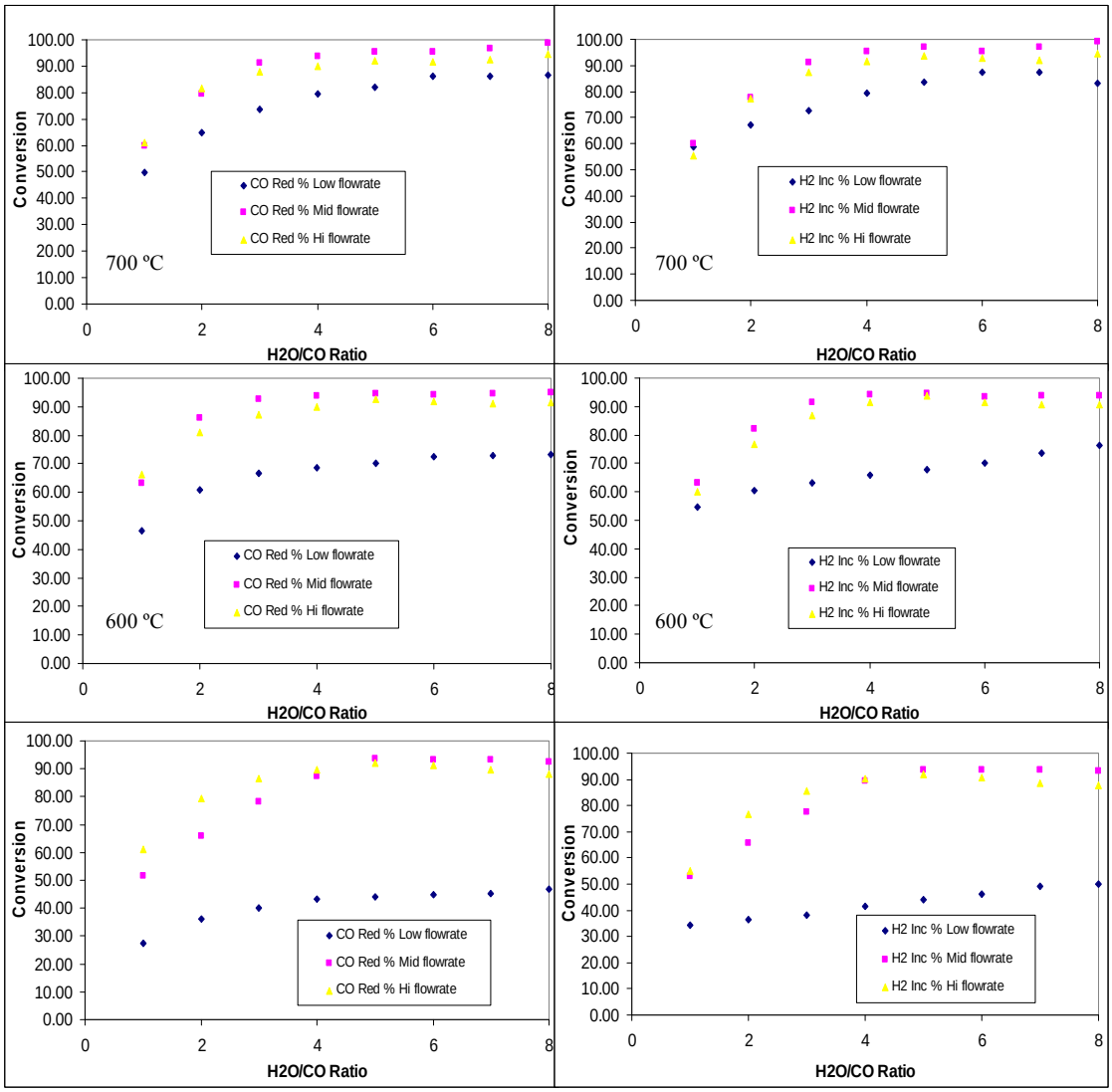

Figure 32: H_2 and CO conversion at different flow rate for various temperatures

5.2.2.1 Validation of WGS predicted results

As mentioned in the previous section, the kinetics of the WGS were extracted from numerous experiments and used in the kinetic model.

Figure 33 shows a typical case of predicted and WGS experiment results at low space velocity for different temperatures while figure 34 depicts the comparison of the predicted results versus experiment results for WGS. As seen from the figures, the predicted results match the experiment results very well with a maximum error of 0.56% and a mean difference of ±0.15%. Thus, this implies that the kinetic model can be confidently used for parametric studies.

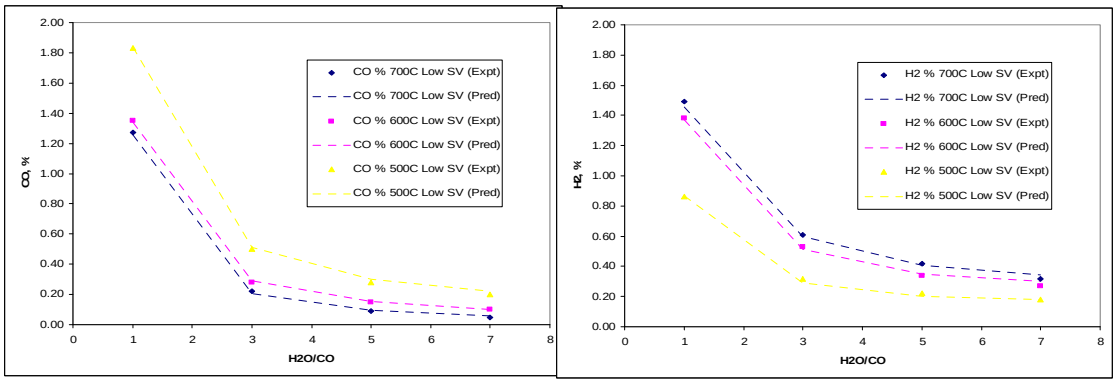

Figure 33: Kinetic model results compared with experiment results for WGS at different temperature (Low space velocity)

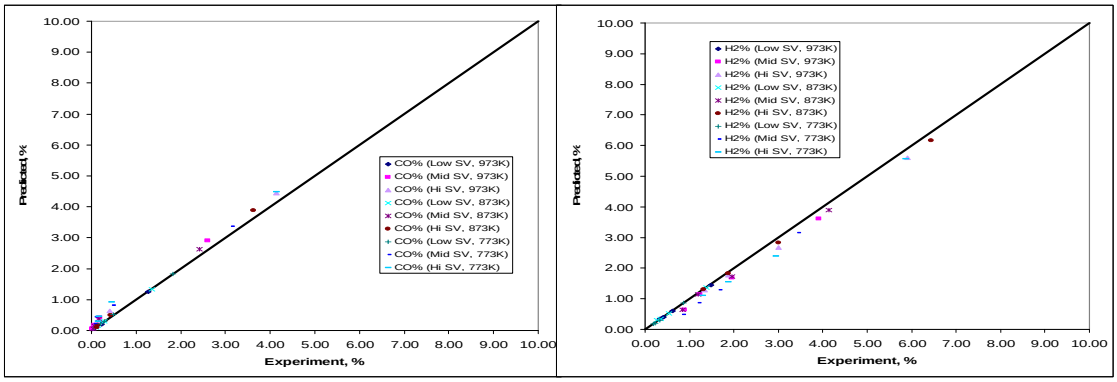

Figure 34: Kinetic model predicted results against experiment results for WGS

5.2.3 Water gas shift assisted autothermal reforming

Several operating points at methane flow rate of 240 l/hr were selected to perform the ATR-WGS (WGS assisted ATR) reaction to record the improvements in reforming performance. The improvement in reforming for AF ratio of 3 and 3.5 are presented in figure 35. The results show that a lower CO and higher H_2 content in the products is achieved with ATR-WGS; up to 4 % (in absolute value) reduction in CO content and 3.08 % (in absolute value) increase in H_2 content are noted while in relative form, up to 38.38 % CO reduction and 11.94 % H_2 increase are noted. From the data, the lowest CO content observed is 4.31 % at AF ratio of 3 and WF ratio of 2.5.

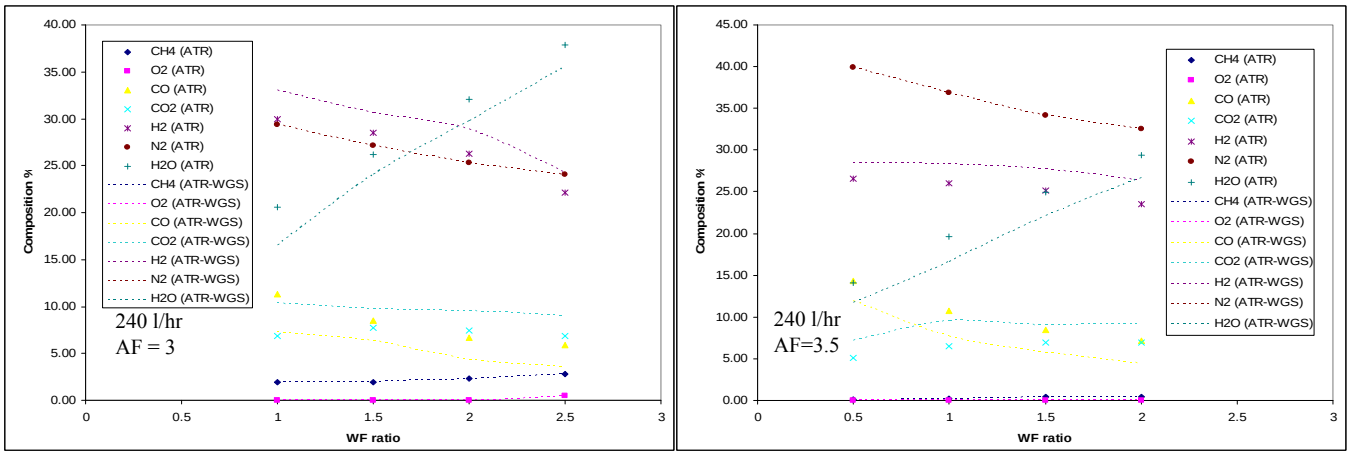

Figure 35: Wet gas product concentration of ATR and ATR-WGS at CH_4 flowrate of 240 l/hr

5.2.3.1 Validation of water gas shift assisted autothermal reforming results

With the kinetics of WGS and ATR extracted from the extensive experimental data, a kinetic model of ATR-WGS is coded for the prediction of ATR-WGS performance.

Figure 36 shows the relationship between the predicted and experimental data of the ATR-WGS while figure 37 shows the difference before and after WGS has been performed on the ATR products.

As seen from figure 36, the predicted results match the experiment results quite well with a maximum error of 4.99% and a mean difference of 2.65%. Thus, this implies that the predictive capability of the kinetic model is reasonable and can be used subsequently for parametric studies.

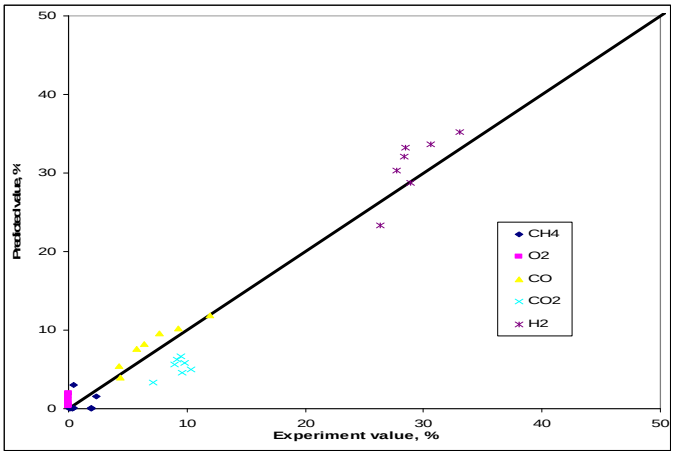

Figure 36: Kinetic model predicted results against experiment results for ATR-WGS

Further results from figure 37 prove that the predicted results match the experiment results quite well with a maximum error of 0.99% and a mean difference of 0.62%.

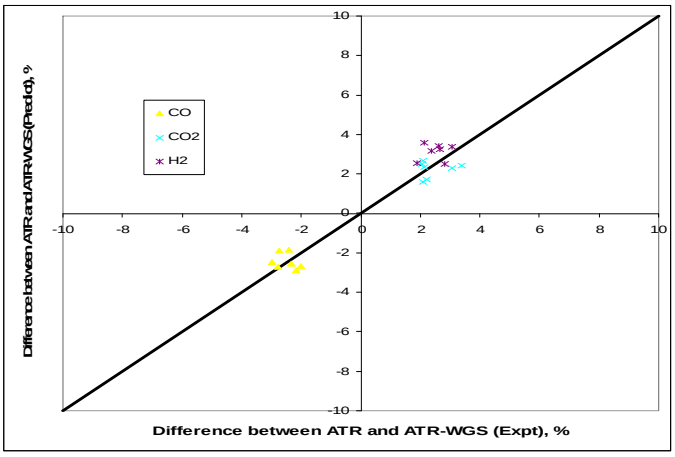

Figure 37: Kinetic model predicted results versus experiment results for ATR-WGS

5.3 Kinetic Model Results

Having verified the predicted results from ATR and WGS kinetic model with the experiment data, the next phase of research is to perform analytical studies on the ATR and WGS reactors which include parameter study, cold start behaviour and transient behaviour.

5.3.1 Autothermal reforming

A study on the effect of parameters on the ATR performance is performed in this section. The baseline of this study is carried out at these operating and geometric parameters:

Flow rate (l/hr):	120
AF ratio:	2.5
WF ratio:	1
Catalyst temperature (K):	873
Gas inlet temperature (K):	423
Pressure (Bar):	1
Reactor radius (m):	0.015
Reactor length (m):	0.2

Table 14: Operating conditions of ATR study

The baseline study is chosen at these conditions as it produced the highest H_2/CH_4 ratio among the experiment points.

Figure 38 shows the relationship between H_2 and the reactor length. From the figure, one can see that H_2 increases with increasing length. It is also observed that there is a slight increase in H_2 towards the end of the reactor. This observation is credited to STR and WGS reaction taking place at this part. The opposite, that is, decrease in CO towards the end of reactor is observed in figure 39, and thus concluding that STR and WGS reaction is the reason behind the observations. In figure 39, it is generally found that the CO increases with increasing length. The CO at the end of each reactor length are: 0.32, 0.4, 0.41 and 0.41 moles, respectively. The relationship between CH_4 conversion and reactor length is shown in figure 40. From this figure, it is observed that the CH_4 conversion increases with increasing length. A conversion of above 99 % is reached around 0.26 m,

which could implies that any longer reactor length will not help much in conversion of CH_4. Figure 41 and 42 shows the catalyst and gas temperature profile, respectively, along the reactor at different length. It can be seen that the gas temperature follows the catalyst temperature closely and it is seen that in general the catalyst temperature is lowest in the front part, highest in the middle part and lower in the rear part of the reactor. This, as explained in the ATR experiment section, is because the front part is cooled by the inlet mixture of low temperature; the middle part is heated by heat release from the total combustion of methane while the rear part is dominated by the endothermic steam reforming reaction, which absorbed the heat from the catalyst. Furthermore, from this figure, one can easily identify the reaction process that is dominant at each section of the reactor. For example, in figure 41, for the reactor length of 0.2 m, the front section is dominated by POX (as characterised by the increasing temperature) and the rear section is dominated by STR (as characterised by the decreasing temperature), while the middle section is in thermal neutral, i.e., neither POX nor STR is dominant in this section, which is a typical temperature profile of ATR reactor when it has reached steady state. Such ATR temperature profile was also shown by Hoang and Chan [125] in their work.

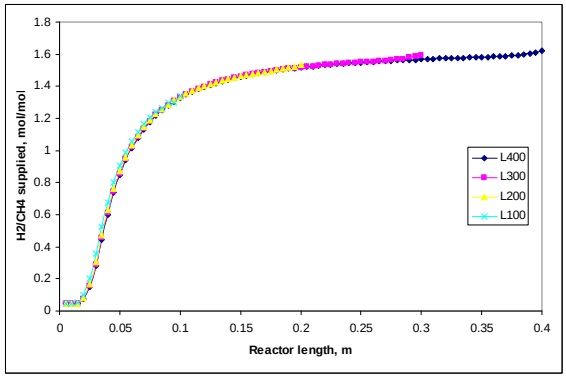

Figure 38: Relationship between H_2 and reactor length

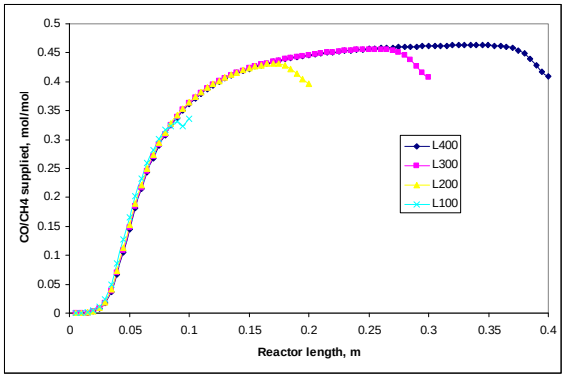

Figure 39: Relationship between CO and reactor length

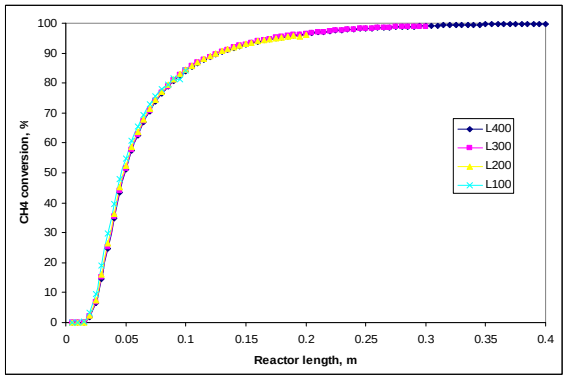

Figure 40: Relationship between CH_4 conversion and reactor length

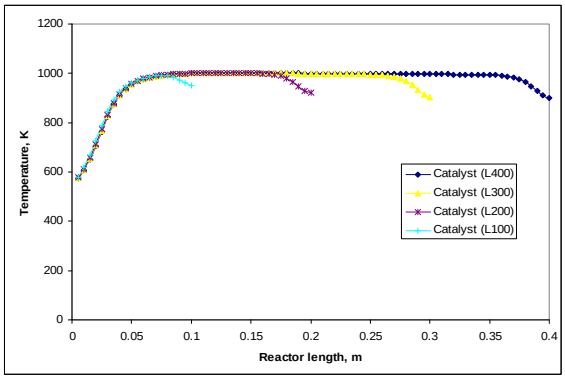

Figure 41: Relationship between catalyst temperature and reactor length

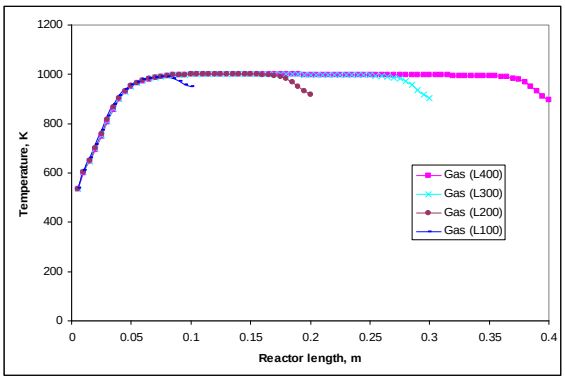

Figure 42: Relationship between gas temperature and reactor length

Figure 43 to 47 presents the effect of length on the performance of reactor with respect to time. In figure 43 and 44, one can see that the time for H_2 and CO to reach steady state (defined as less than 1% change in H_2 and CO) increases with length. For the length of 0.1 m, the steady state is reached at about 150 secs while it takes about 450 secs to reach steady state for a reactor length of 0.4 m. From these two figures, one can also see that for reactor length more than 0.2 m, the CO is much lower in the first 100 secs. This could suggest that short duration supply such as pulsating flow may improve the overall performance, that is, low CO and high H_2. Similar observation is also noticed in figure

45, where the relationship between methane conversion and time is shown. The time required for conversion to reach steady state increases with reactor length. It is also noted that high methane conversion is reached within a short duration of 100 secs, thus, suggesting that pulsating flow may improve the overall performance. In figure 46 and 47, the catalyst and gas temperature in the reactor is plotted against time. It is found that the gas temperature follows the catalyst temperature closely and the time for the temperature to reach steady state increases with reactor length. This is so because the volume of reactor is increased and thus requiring longer time to reach a steady state.

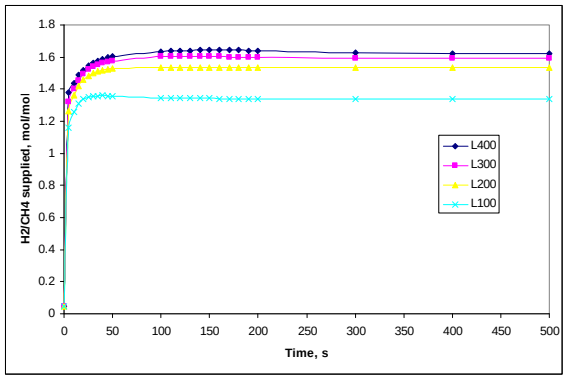

Figure 43: Relationship between H_2 and reactor length

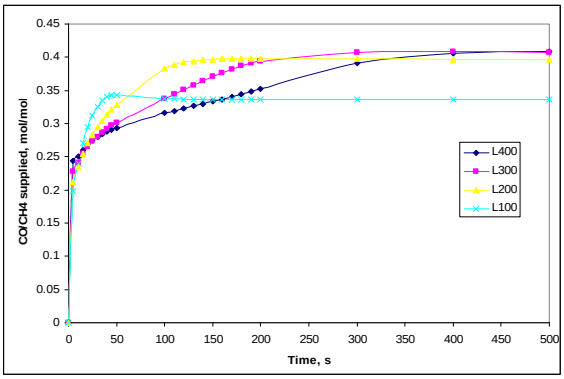

Figure 44: Relationship between CO and reactor length

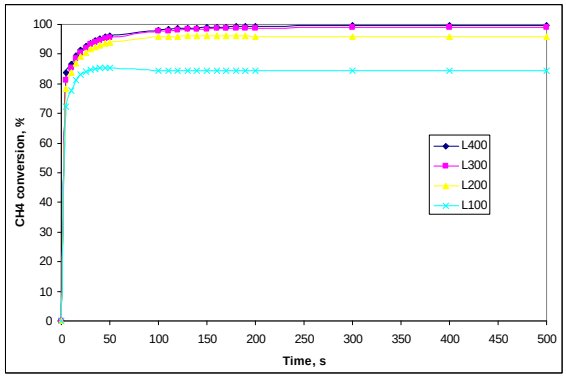

Figure 45: Relationship between CH_4 conversion and reactor length

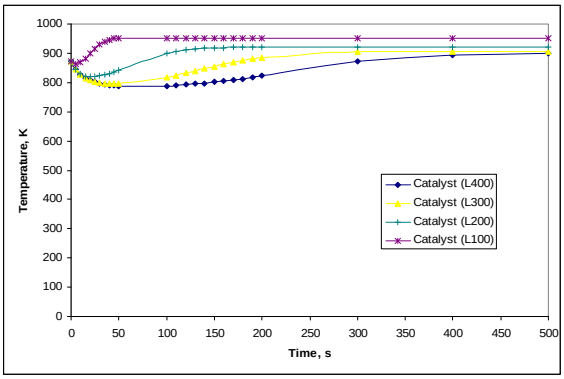

Figure 46: Relationship between catalyst temperature and reactor length

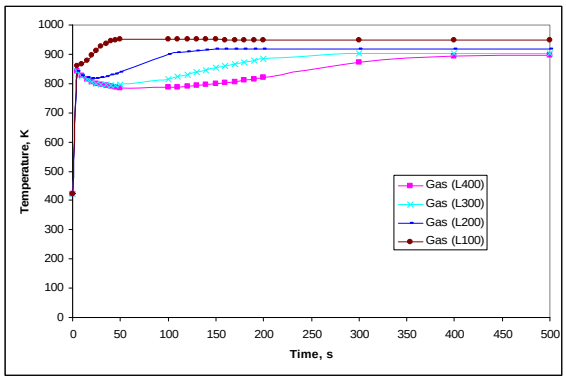

Figure 47: Relationship between gas temperature and reactor length

The effect of flow rate on the performance of ATR is presented in the figures 48 to 55. Figures 48 to 51 show the effect of flow rate on the performance with respect to reactor length while figures 52 to 55 show the effect of flow rate on the performance with respect to time.

In figure 48 and 50, it is observed that the H_2 and CH_4 conversion decreases with increasing flow rate. This can be explained by the temperature profile depicted in figure 51; the higher flow rate caused more cooling in the front portion of the reactor and thus less catalytic reaction in this section, resulting in lower H_2 and CH_4 conversion. Figure 51 also shows that the heated zone shifted to the rear of the reactor. From these observations, one can conclude that an optimum flow rate is required to achieve high performance in ATR. Correspondingly, the CO shows a similar trend to the H_2 (figure 49). However, it is noticed that the CO dips towards the end of the reactor for 60 and 120 l/hr. This could be due to STR and WGS reaction taking place in this section with STR and WGS reaction more prominent at 60 l/hr than at 120 l/hr. At the flow rate of 180 l/hr, the excessive cooling in the front and middle portion of the reactor pushed the

reforming reactions towards the rear. As such, POX is still dominant in this section and no dip in CO is observed at the rear portion.

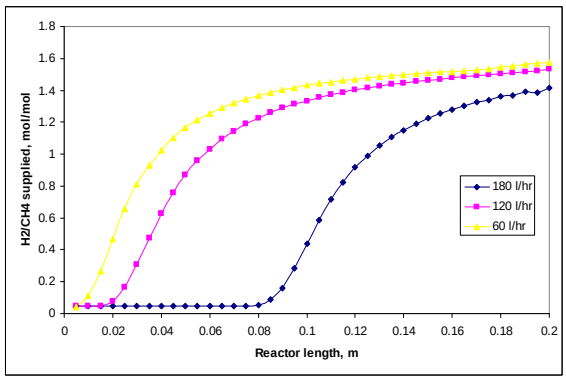

Figure 48: Relationship between H_2 and flow rate

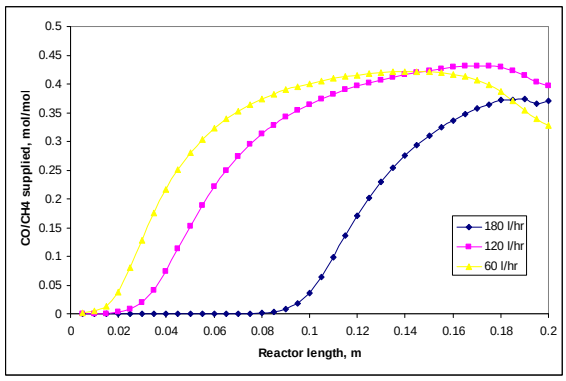

Figure 49: Relationship between CO and flow rate

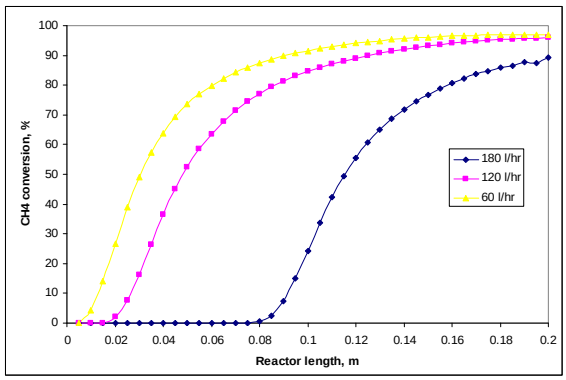

Figure 50: Relationship between CH_4 conversion and flow rate

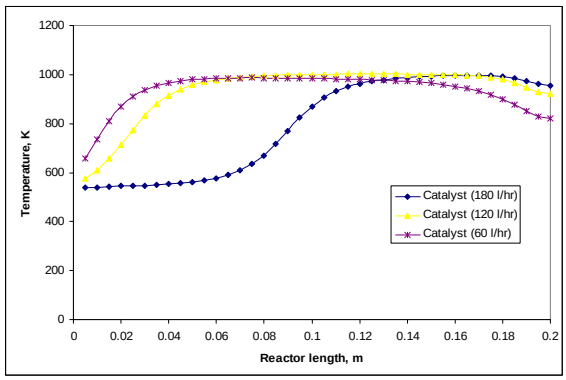

Figure 51: Relationship between catalyst temperature and flow rate

Figure 52 to 55 depicts the effect of flow rate on the performance of ATR with respect to time. Similar to the observations made in the previous paragraph on the effect of flow rate with respect to reactor length, it is found that increasing flow rate has a detrimental effect on the performance of ATR; the H_2 yield and CH_4 conversion decreases with increasing flow rate while CO generally increases with flow rate. In addition, the time required to reach steady state increases with flow rate. It took 400 secs for the reactor to reach steady state at flow rate of 60 l/hr while more than 500 secs is required to reach steady state for flow rate 120 and 180 l/hr. It is noted that CO at flow rate of 180 l/hr is higher initially but gradually drop to the level below that of 120 l/hr. This is because the front and middle portion is progressively cooled, causing reduced catalyst activity as reaction is temperature dependent. In figure 55, the effect of flow rate on the temperature profile is shown. As seen from the figure, the reactor temperature increases with higher flow rate as POX is dominant at higher flow rate.

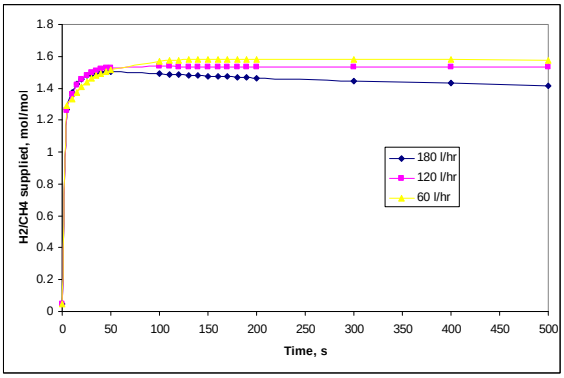

Figure 52: Relationship between H_2 and flow rate

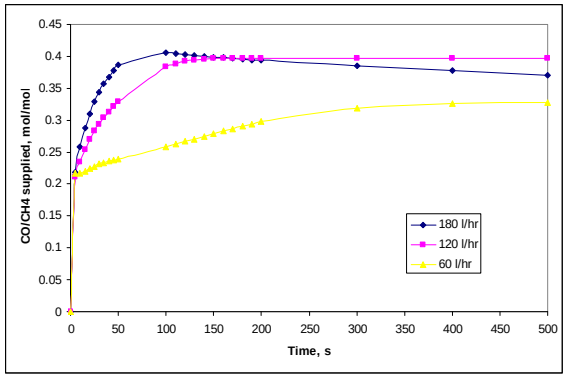

Figure 53: Relationship between CO and flow rate

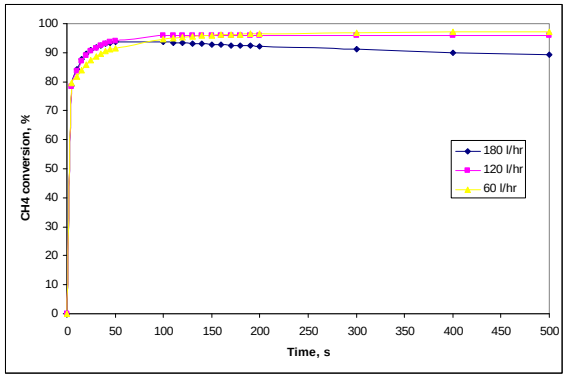

Figure 54: Relationship between CH_4 conversion and flow rate

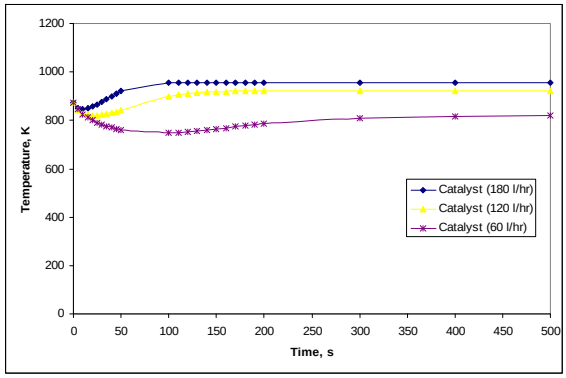

Figure 55: Relationship between catalyst temperature and flow rate

The next parameter study is conducted on the effect of reactor radius on the ATR performance, which is shown in figures 56 to 63. In figure 56 and 58, the results show that changes in reactor radius do not produce significant effect on the H_2 yield and CH_4 conversion with a maximum difference of 0.03 mole observed at the exit of reactor. However, if one were to consider the results before 0.1 m, it is clear that H_2 yield and CH_4 conversion increases with increasing radius. This is because that during a fixed flow rate and reactor length, the smaller reactor radius would translate into faster flow rate thus cooling the front portion of the reactor, which is similar to the scenario at high flow rate in the study of flow rate effect. However, it is suspected that at the range of radius used in this study, the resident time of the gases is still sufficiently long to negate the difference in radius change and therefore, the H_2 yield is very close at the exit. Figure 57 depicts the relationship between CO production and reactor radius with respect to reactor length. The figure shows that CO reduces with increasing reactor radius at the exit of the reactor. It also shows that STR is more dominant than POX when the reactor radius is increased, hence the lower CO production at smaller radius. This phenomenon is also

evident in figure 59, where the temperature profile of the reactor is presented. It can be seen in figure 59 that the temperature drops with increasing length for radius above 0.03 m, indicating the strong presence of STR and less of POX.

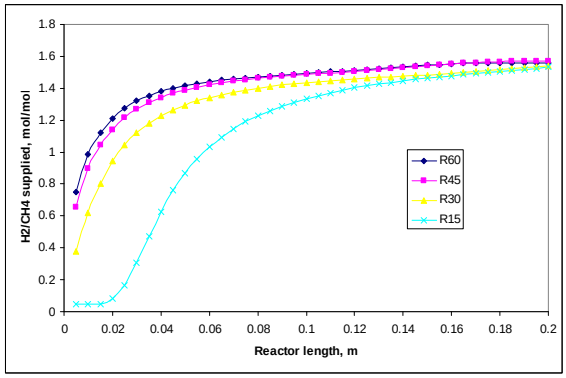

Figure 56: Relationship between H_2 and reactor radius

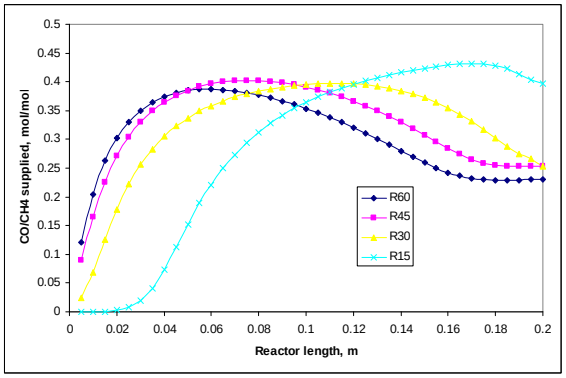

Figure 57: Relationship between CO and reactor radius

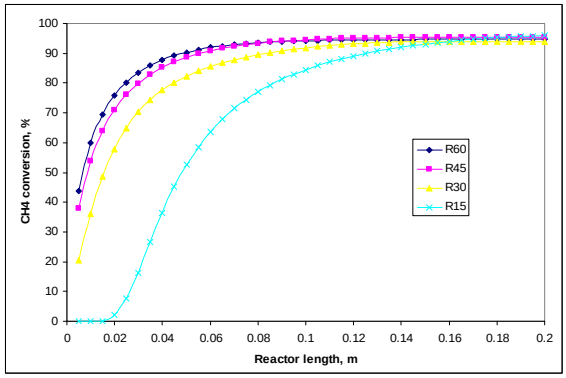

Figure 58: Relationship between CH_4 conversion and reactor radius

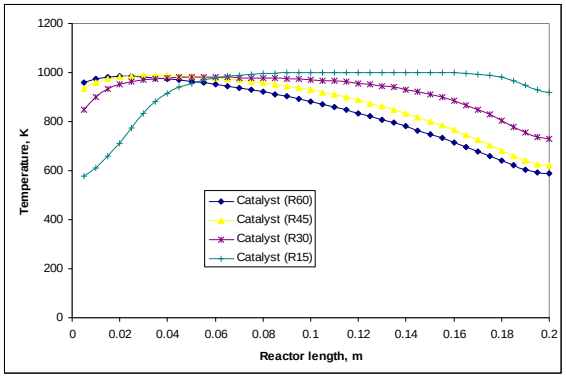

Figure 59: Relationship between catalyst temperature and reactor radius

The effect of change in reactor radius on the ATR performance with respect to time is presented in figure 60 to 63. From these figures, one can see that the time required for the reactor to reach steady state is shorter for smaller radius. The results also show that the transition from STR to POX is dominant in the reaction for radius above 0.03 m at around 50 to 100 secs where CO begins to rise. In addition to this, it is evident that POX is dominant throughout the reaction for reactor radius at 0.015 m as there is no dip in CO and high CO is observed throughout the simulated period. The temperature profile presented in figure 63 further fortifies these observations; the temperature for larger radius decreases in an exponential manner while temperature for radius of 0.015 m increases gradually.

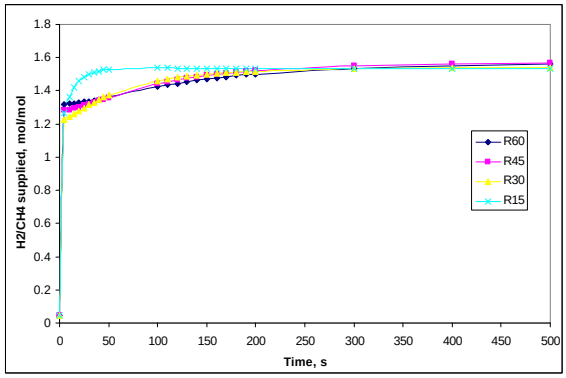

Figure 60: Relationship between H_2 and reactor radius

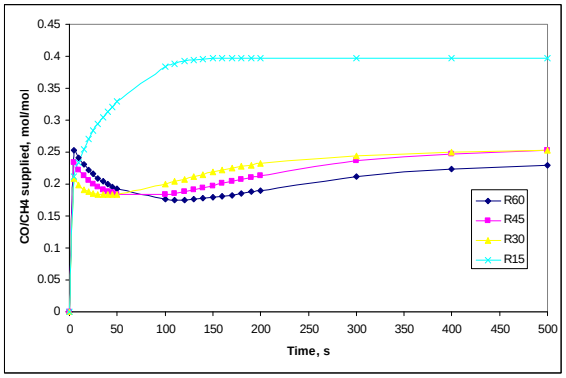

Figure 61: Relationship between CO and reactor radius

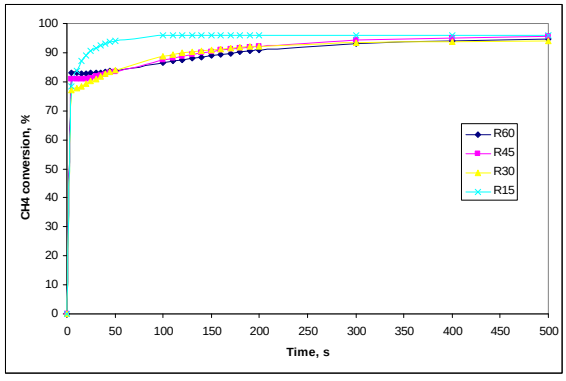

Figure 62: Relationship between CH_4 conversion and reactor radius

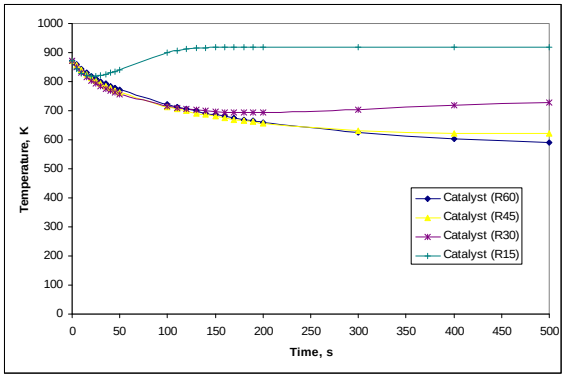

Figure 63: Relationship between catalyst temperature and reactor radius

The effect of inlet gas temperature on the ATR performance is presented in the following figures.

Figure 64 shows the relationship between H_2 yield and inlet gas temperature. It can be seen that increasing inlet gas temperature helps to get higher H_2 yield. The figure also shows that the difference in H_2 yield at different gas temperature is small with no significant effect after the inlet gas temperature is increased to 623 K. This is possibly because the inlet gas temperature mainly affects the front portion of the reactor only, that is, heating or cooling the front portion of the reactor. This is further supported by the evidence in figure 67 where the temperature profile of the reactor is presented. From this figure, one can see that POX is dominant in the front part and thermal-neutral in the middle, with slightly stronger presence of STR at the rear part of the reactor. It is also noted that the heat generated from POX reaction is affected by the inlet gas temperature. From figure 65, one see that CO decrease with increasing temperature at the exit of the reactor due to STR and WGS reaction while CO increases with increasing temperature at the front and middle portion of the reactor due to stronger POX reaction, which is not desired in H_2 production. Hence, the use of higher gas inlet temperature to improve ATR performance is rather limited. In figure 66 where the relationship between CH_4 conversion and inlet gas temperature is shown, similar trend in the figure 64 is observed. The figure shows that the difference in CH_4 conversion at different gas temperature is small with no significant effect after the inlet gas temperature is increased to 623 K. The explanation for this phenomenon is the same as the effect of inlet gas temperature on the H_2 mentioned above. Similar findings were also found in Lin *et al* work [157].

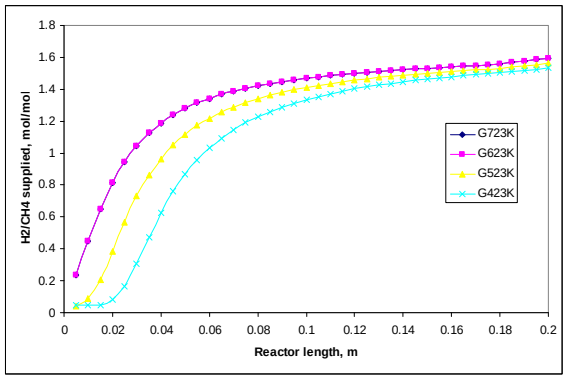

Figure 64: Relationship between H_2 and inlet gas temperature

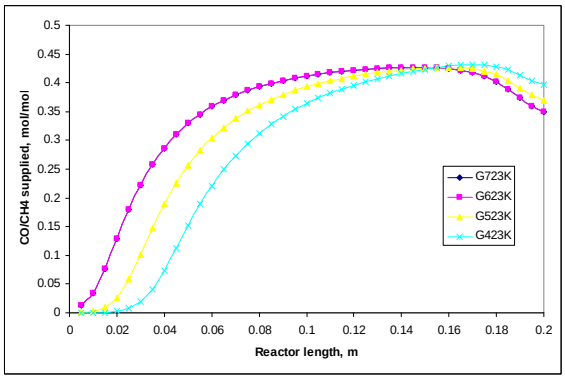

Figure 65: Relationship between CO and inlet gas temperature

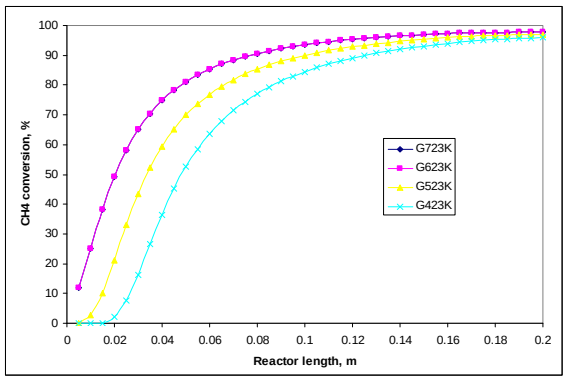

Figure 66: Relationship between CH_4 conversion and inlet gas temperature

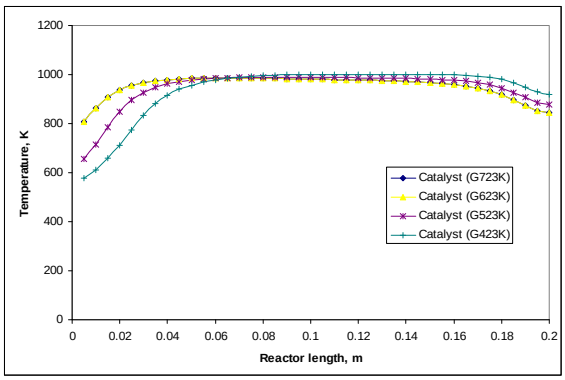

Figure 67: Relationship between catalyst temperature and inlet gas temperature

Figure 68 to 71 show the effect of inlet gas temperature on the ATR performance dependent on time. In these figures, we see similar trends in the results shown previously; H_2 yield and CH_4 conversion increases with inlet gas temperature while CO decreases with increasing inlet gas temperature. In addition, there are no significant effects on the ATR performance after the inlet gas temperature is increased to 623 K for the simulated operating conditions. The results also show that the reactor reaches a steady state at a shorter period of time when the inlet gas temperature is lowered. The lower H_2 yield, lower CH_4 conversion, higher CO and higher reactor temperature

suggests that the strong presence of POX reaction at lower inlet gas temperature contribute to this observation; the opposite is true as STR favoured higher temperature. The temperature profile in figure 71 also shows the transition from STR to POX as the temperature dips initially and increases gradually with time.

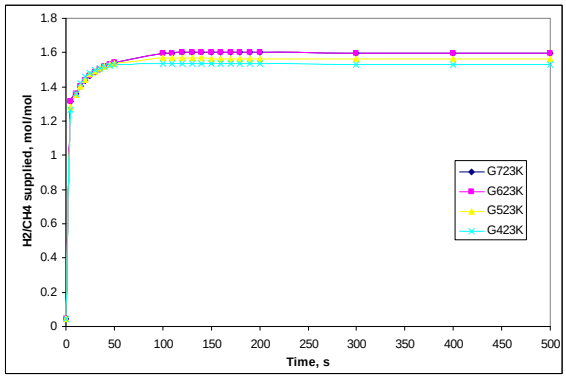

Figure 68: Relationship between H_2 and inlet gas temperature

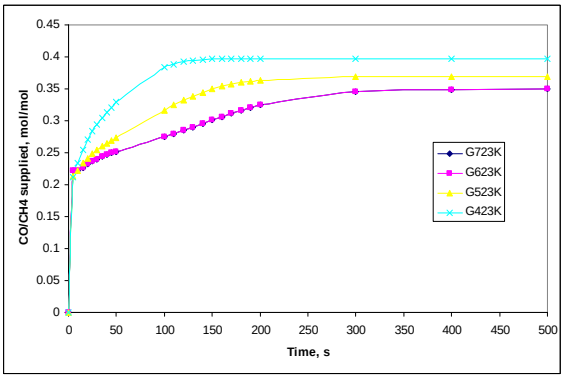

Figure 69: Relationship between CO and inlet gas temperature

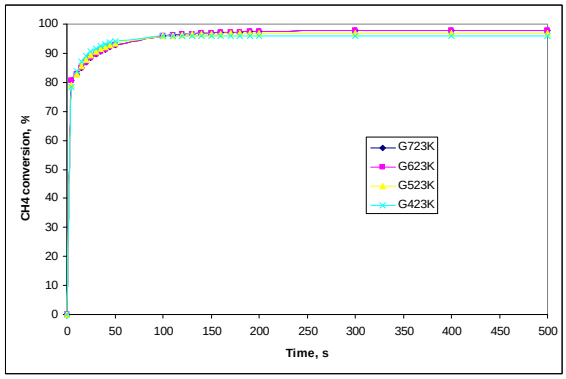

Figure 70: Relationship between CH_4 conversion and inlet gas temperature

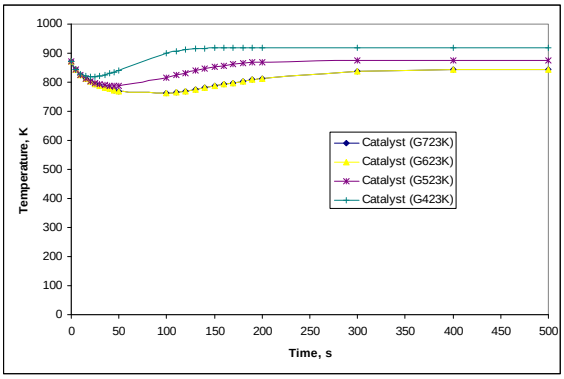

Figure 71: Relationship between catalyst temperature and inlet gas temperature

5.3.1.1 Cold start behaviour of autothermal reforming

A cold start study on ATR is performed to understand the dynamic changes of the composition and temperature in the reactor during the cold start operation. In addition, the amount of time taken for the reactor to reach steady state for a given inlet gas temperature and the light off temperature of the catalyst can also be determined.

In this study, ATR model is carried out at these operating and geometric parameters:

Flow rate (l/hr):	120
AF ratio:	2.5
WF ratio:	1
Catalyst temperature (K):	298
Gas inlet temperature (K):	Variable
Pressure (Bar):	1
Reactor radius (m):	0.015
Reactor length (m):	0.2

Table 15: Operating conditions of ATR cold start study

Under these prescribed conditions, the likelihood of solid carbon formation in the catalyst is greatly reduced as there is sufficient water to suppress the carbon formation in the inlet gas mixture. The results of this cold study are presented in figure 72 to 76 as shown below.

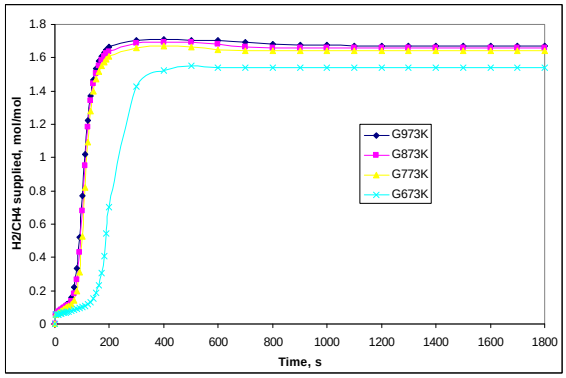

Figure 72: H_2 at various inlet gas temperatures for ATR cold start

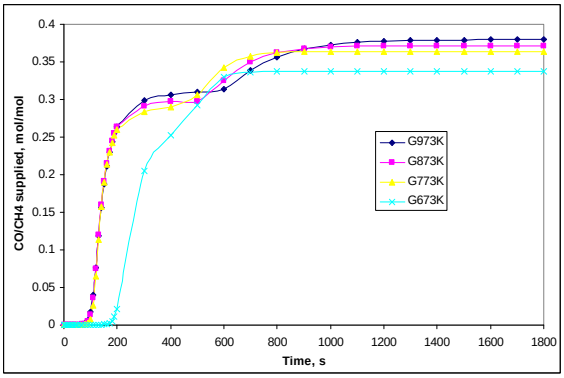

Figure 73: CO at various inlet gas temperatures for ATR cold start

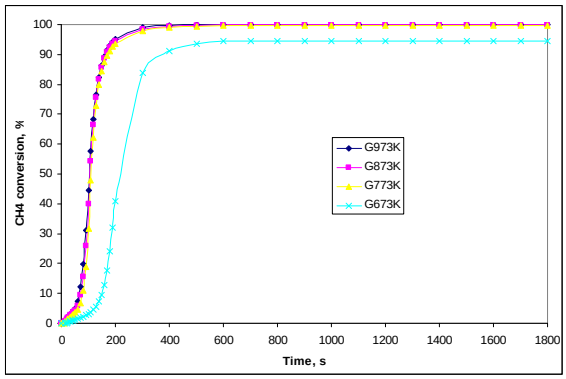

Figure 74: CH_4 conversion at various inlet gas temperatures for ATR cold start

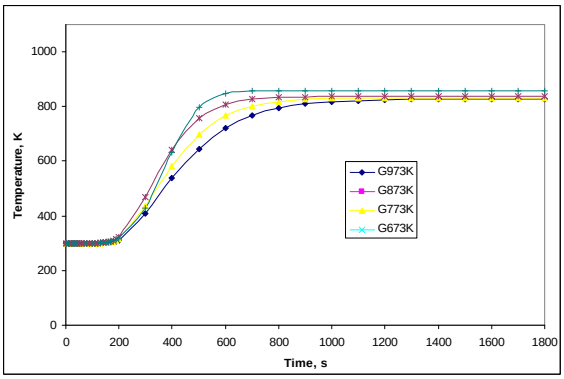

Figure 75: Reactor catalyst temperature profile at various inlet gas temperatures for ATR cold start

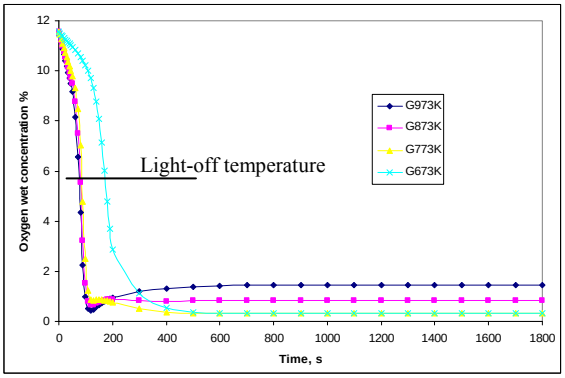

Figure 76: Oxygen concentration at various inlet gas temperatures for ATR cold start

From these results, one can see that H_2 yield and CH_4 conversion increases with inlet gas temperature. However, at about 500 secs, it can be seen that there is a marginal drop in H_2 and a corresponding increase in CO. The reason for this occurrence is likely due to

reverse WGS reaction taking place. In addition, the temperature profiles at different inlet gas temperatures during cold start reveal that a lower inlet gas temperature (but sufficiently high temperature to heat up the cold catalyst bed) can reach the steady state quicker than higher inlet gas temperature. The reason for this phenomenon was explained earlier in the parameter study on the effect of inlet gas temperature. The stronger presence of STR in the reaction contributed to the lower reactor temperature when flow with higher inlet gas temperature is supplied. It should be noted that STR is favoured by high temperature and is an endothermic process.

The light-off temperature for each cold start case can be determined from figure 76. However, there are a number of definitions for light-off temperature in many ways. Ma [158] quotes light-off temperature as the temperature at which 10 % of the fuel is converted while Patterson *et al* [159, 160] introduces T_{50} which is defined as the light-off temperature required for 50% conversion of hydrocarbons. In this study, the definition of "light-off" is adopted from Schmidt [103], i.e., TO_{50}, which is the temperature at which 50 % of the supplied oxygen is consumed.

Having defined light-off temperature, results show that it takes 74, 79, 86 and 177 seconds for the reactor to reach light-off temperature at inlet gas temperature of 973 K, 873 K, 773 K and 673 K, respectively. The results also show that cold starting with inlet gas temperature greater than 773 K gives no major improvement in fuel conversion.

5.3.1.2 Optimisation of autothermal reforming

With the ATR parameter studies done, it is possible to determine the reactor size and flow rate for optimum ATR performance by converting all the parameter studies' results with respect to space velocity. Space velocity, in this case, is defined as the amount of gaseous mixture flowing through the reactor divided by the volume of the reactor and has the unit of hr^{-1}.

Figure 77 presents the performance of ATR with respect to space velocity at 2.5 AF and 1 WF. From this figure, it can be identified that the optimum CH_4 conversion and H_2 yield lies around space velocity of 424.36 hr^{-1}. However, the result also shows that the amount of CO is also high at this point. A good compromise between CH_4 conversion, H_2 and CO can be reached by operating the reactor at around 300 hr^{-1}. With this data, the size of the ATR reactor can be determined to perform optimum performance.

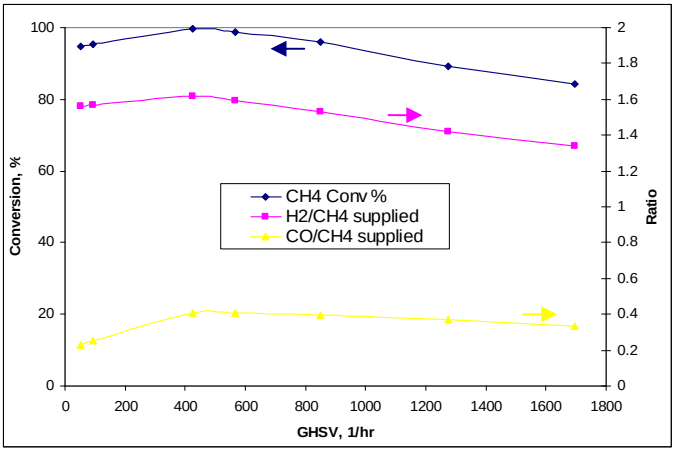

Figure 77: Performance of ATR with respect to GHSV

In comparison, equilibrium model identified 2.7 AF and 3 WF as the optimum operating point for ATR at 1 atm. From the point identified and experiment results, one can see that equilibrium model does not take into consideration the operating temperature that is achievable and sustainable. In addition, the disregard of other operating and geometric parameters such as feedstock flow rate and reactor size is apparent in equilibrium model; these will affects the space velocity, velocity profile, temperature profile and ultimately, the prediction accuracy. As such, optimisation of ATR should be done using kinetic model for predictions that is closer to experiment data.

5.3.2 Water gas shift

5.3.2.1 Parameter study

A parameter study on WGS has been carried out to achieve a better understanding of the process. The main focus of this study is on the steady state as significant changes occur during the first 10 seconds after which the change in composition will be minimal.

The baseline of the WGS study is carried out under these operating and geometric parameters:

Flow rate (l/hr):	120
Inlet CO %:	2.1
Inlet H_2O %:	6.3
Catalyst temperature (K):	973
Gas inlet temperature (K):	423
Pressure (Bar):	1
Reactor radius (m):	0.015
Reactor length (m):	0.2

Table 16: Operating conditions of WGS study

Figure 78 to 82 shows the effect of reactor length on WGS performance. Figure 78 to 80 shows the performance changes with respect to reactor length while figure 81 and 82 present the performance changes with respect to time.

The results in figure 78 to 80 reveal that composition change in CO and H_2 reaches a maximum at 0.2 m, after which the reactor length has no effect on the composition. Although, from wheel *et al* [161], it is expected that there will be increase in CO conversion in achieved by lengthening the reactor, it can be explained that the reaction has already reached equilibrium and further length would not further affect it. Similar observation is noted in the temperature profile of the reactor in figure 80; there are no significant changes in the temperature when the reactor length is increased beyond 0.2 m. These observations are mirrored in figure 81 and 82; the compositions remain unaffected for reactor length above 0.2 m. This suggests that a minimisation of the WGS reactor size is possible without affecting the performance. It is also possible that WGS reaction is not very sensitive to the space velocity.

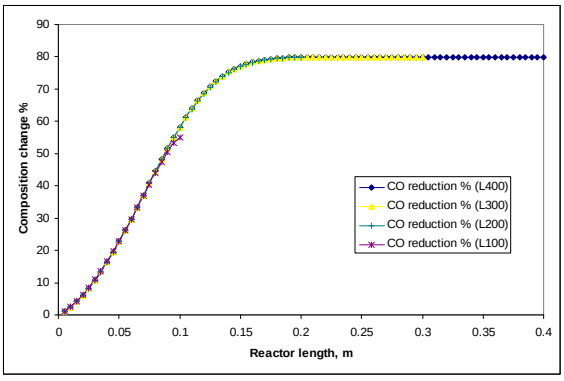

Figure 78: Relationship between CO reduction and reactor length

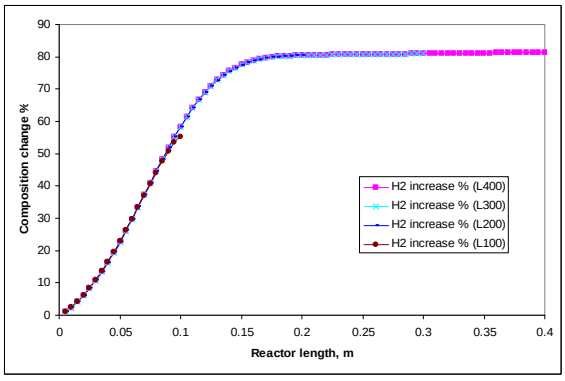

Figure 79: Relationship between H_2 increment and reactor length

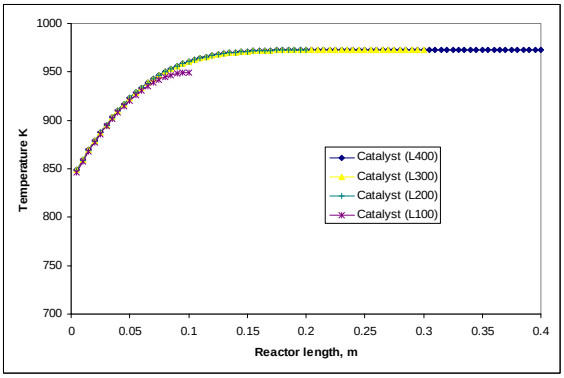

Figure 80: Relationship between catalyst temperature and reactor length

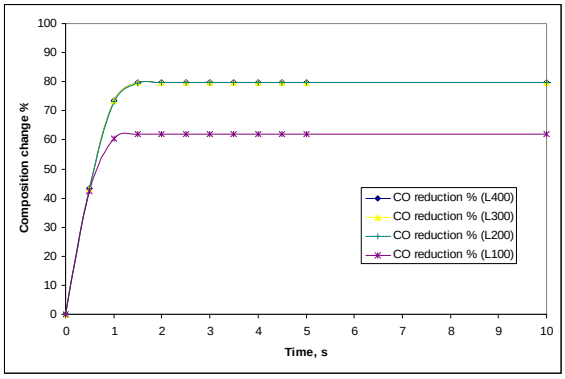

Figure 81: Relationship between CO reduction and reactor length

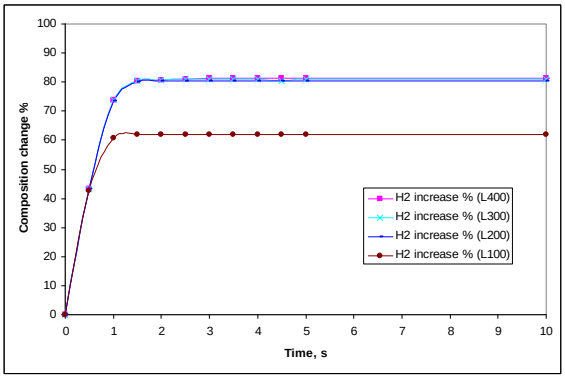

Figure 82: Relationship between H_2 increment and reactor length

Figure 83 to 85 illustrate the effect of reactor radius on the WGS performance. From these figures, one can see that composition change in CO and H_2 increases with reactor radius before the reactor exit. In addition, for the section before the reactor exit, the temperature of the reactor also increases with reactor radius. From these results, one can deduce that smaller radius, which is equivalent to faster space velocity, cools the front portion of the reactor and could lower the performance of the WGS reactor if the space velocity is moderately higher. Furthermore, this indicates that WGS reaction in our study is temperature sensitive.

More importantly, the results from these figures can be used to predict the performance of a WGS reactor with radius dimensions within the study.

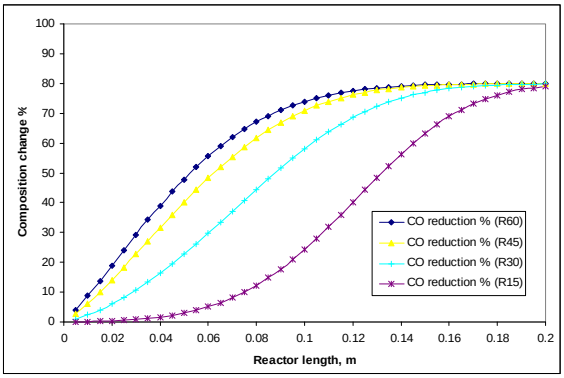

Figure 83: Relationship between CO reduction and reactor radius

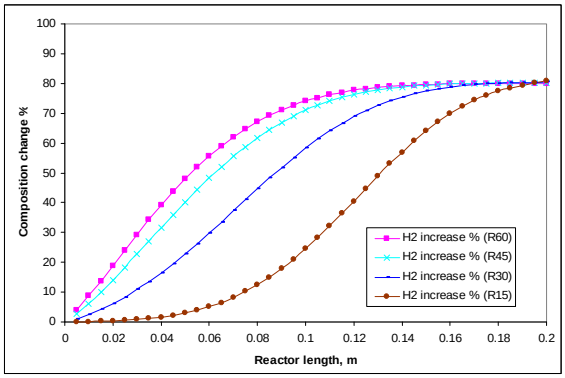

Figure 84: Relationship between H_2 increment and reactor radius

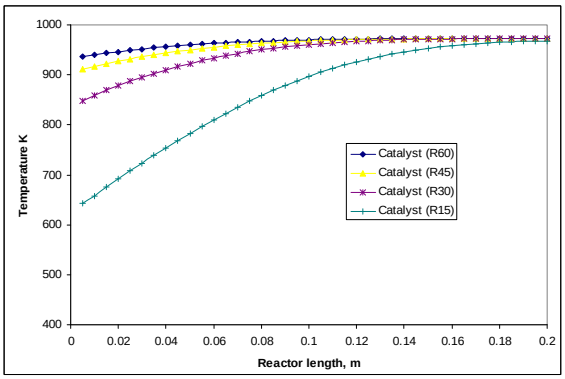

Figure 85: Relationship between catalyst temperature and reactor radius

The effect of flow rate changes on the WGS performance is depicted in figure 86 to 88. The figures show that composition change in CO and H_2 decreases with increasing flow rate. Similarly, the temperature in the reactor decreases with increasing flow rate. The reason for these observations is due to the cooling of the front portion caused by higher flow rate and thus, less reaction in the front portion. Also, faster flow rate would mean that there is lesser resident time between the gases and the catalyst and hence, lower conversion. However, it is evident that for the same reactor length, flow rate slower than

120 l/hr would yield similar results in the gases product. Subsequently, the performance of WGS reactor can only be improved marginally (around 5% for difference of 60 hr^{-1}) by use of slower flow rate down to 120 l/hr.

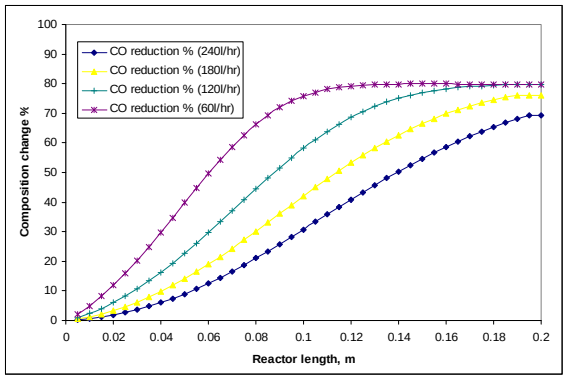

Figure 86: Relationship between CO reduction and flow rate

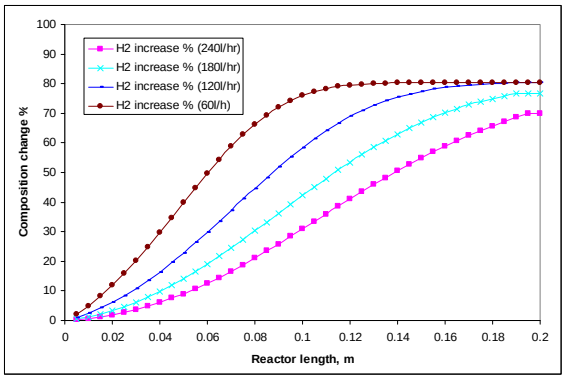

Figure 87: Relationship between H_2 increment and flow rate

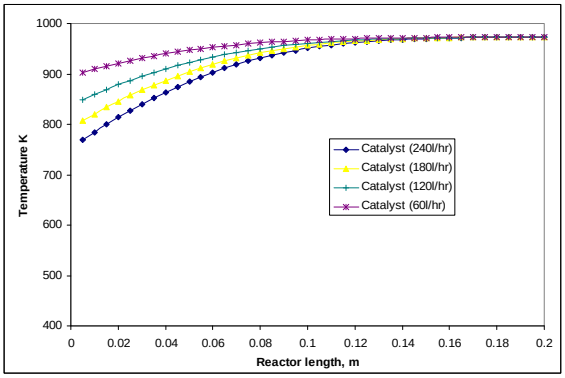

Figure 88: Relationship between catalyst temperature and flow rate

The next parametric study is on the effect of inlet gas temperature on the WGS performance, which is illustrated in figure 89 to 91. Once again, one can see that composition change in CO and H_2 and the reactor temperature is the same at the reactor exit (0.2 m). However, if one considers the section before 0.1 m, it is evident that the performance of the WGS reactor improves with higher inlet gas temperature. This is because the higher inlet gas temperature heats up the front portion of the reactor which in turn increases the reaction rate of WGS. This also demonstrates that the WGS reaction is temperature sensitive and less sensitive to space velocity. Similar observations were made by Li *et al* [75] in their study when they carried an experiment to investigate the effect of temperature on WGS reaction.

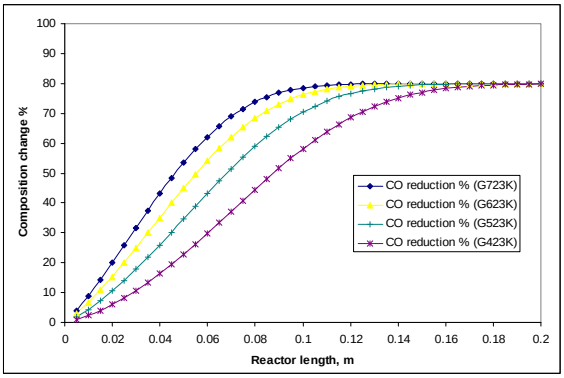

Figure 89: Relationship between CO reduction and inlet gas temperature

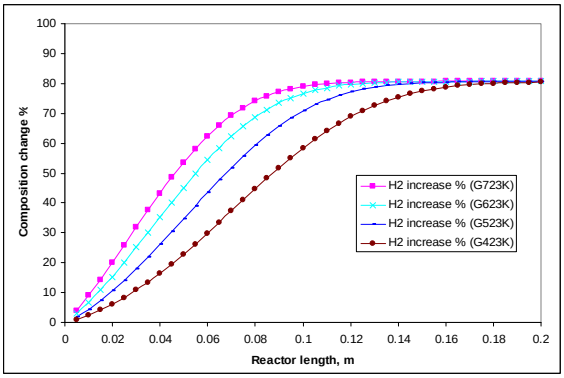

Figure 90: Relationship between H_2 increment and inlet gas temperature

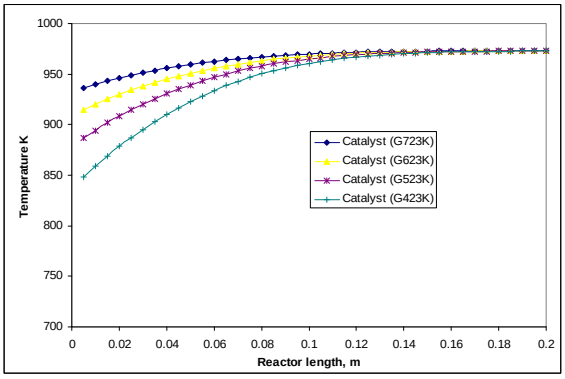

Figure 91: Relationship between catalyst temperature and inlet gas temperature

Figure 92 to 94 present the relationship between the initial catalyst temperature and the WGS performance. Overall, the results show that catalyst temperature and composition change in CO and H_2 increases with temperature. It is also noted that for this operating condition, the performance of WGS reaction is better at 873 K than at 973 K, which is also reflected in the WGS experiment results. These results prove that, for the catalyst used in this study, the WGS reaction is temperature sensitive and favoured by high temperature.

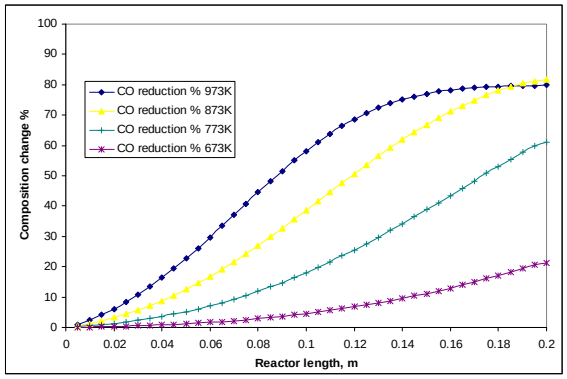

Figure 92: Relationship between CO reduction and initial catalyst temperature

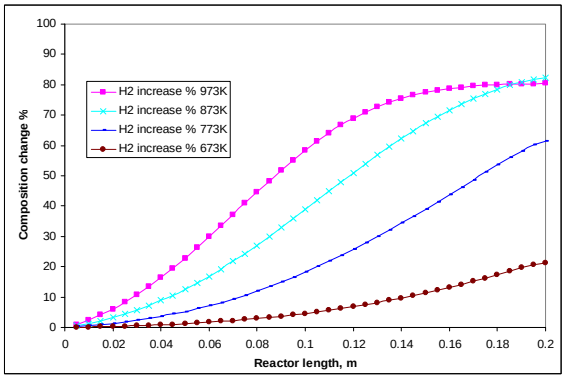

Figure 93: Relationship between H_2 increment and initial catalyst temperature

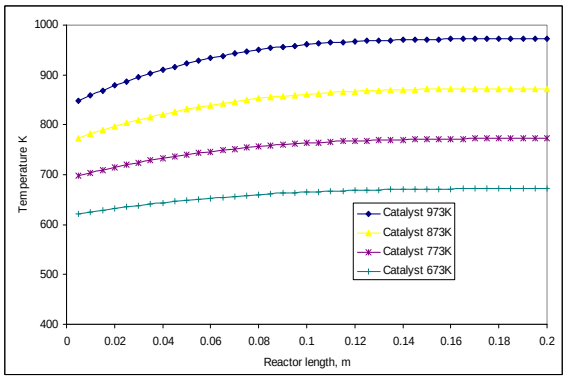

Figure 94: Relationship between catalyst temperature and initial catalyst temperature

5.3.2.2 Optimisation of water gas shift

With the WGS parameter studies done, it is possible to determine the reactor size and flow rate for optimum WGS performance by converting all the parameter studies' results with respect to space velocity.

Figure 95 presents the performance of WGS with respect to space velocity. From this figure, it can be identified that the optimum region for WGS is from 106.09 to 212.18 hr^{-1}. However, as mentioned previously in the parameter study of WGS, WGS is more sensitive to temperature. This evidence is shown as additional data points at 873 K for the same space velocity at 212.18 hr^{-1}.

From the experiment and predicted data, it is determined that the optimum temperature for WGS lies between 873 and 973 K. Hence, with this data, the size of the WGS reactor can be determined to obtain optimum performance.

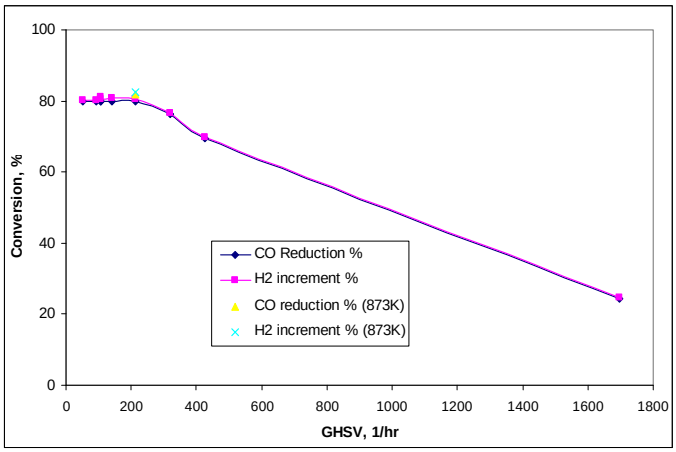

Figure 95: Performance of WGS with respect to GHSV

5.3.3 Water gas shift assisted autothermal reforming

In the project scope, the cold start behaviour of WGS integrated ATR reactor is one of the main area to be studied. Although the dynamic behaviour of the ATR in the ATR-WGS reactor is expected to be the same as a standalone ATR reactor, the dynamic response of WGS in the ATR-WGS reactor is unknown and has not been carried out by other researchers.

5.3.3.1 Cold start behaviour of water gas shift assisted autothermal reforming

A cold start study on ATR-WGS has been performed to understand the dynamic response of the composition and temperature in the ATR-WGS reactor during the cold start operation. In addition, the amount of time taken for the reactor to reach steady state for a fixed inlet gas temperature can also be determined.

For this study, ATR-WGS model is carried out at different cases of operating conditions to understand the cold start behaviour at different conditions. The results of ATR-WGS operating at different conditions are presented below.

Case	1	2	3
ATR Reactor			
Flow rate (l/hr):	240	120	240
AF ratio:	3.5	2.5	2.5
WF ratio:	1	1	1
Catalyst temperature (K):	298	298	298
Gas inlet temperature (K):	Variable	Variable	Variable
Pressure (Bar):	1	1	1
Reactor radius (m):	0.015	0.015	0.015
Reactor length (m):	0.2	0.2	0.2
WGS Reactor			
Maximum inlet gas temperature (K):	873	873	873
Catalyst temperature (K):	variable	variable	variable
Reactor radius (m):	0.015	0.015	0.015
Reactor length (m):	0.2	0.2	0.2

Table 17: Operating and geometric parameters of ATR-WGS cold start study

Figure 96 to 98 illustrate the cold start behaviour of ATR-WGS reactor with the operating conditions stated for case 1 in Table 17. The ATR results show an initial increase in H_2 yield follow by a drop in H_2 before reaching steady state. Similarly, the CO in ATR experiences a sharp increase and suffers a drop before increasing sharply with a slight

overshoot to reach the steady state. The phenomenon observed in this result can be explained as follows: In the initial start-up, the reaction process consisted of POX and STR with POX dominating the reactions. However, as the reaction continues, the oxygen in the reactor is depleted and STR became the dominant process (thus the drop in CO) until Reverse-WGS (RWGS) took effect before the reactions reached a steady state.

Since WGS is integrated with ATR reactor, the trend of composition change follows ATR reactor albeit with a slightly higher H_2 and a lower CO; the difference in H_2 and CO is 0.15-0.18 mole and 0.19-0.22 mole, respectively, for the range of different inlet gas temperature studied. It is observed that the time required to reach light-off temperature for WGS catalyst affects the time at which WGS reaction began to take place. As such, it can be seen that for the case with initial gas temperature of 673 K, CO starts to decrease between 200 to 300 secs while other cases starts around 300 secs.

In addition, it is noted that the time for the ATR-WGS reactor to reach a steady state is longer as WGS is a slower reaction than ATR; it took about 200 secs longer to reach steady state. This is evident in the gradual change of CO and H_2 in WGS reactor as compared to the composition change in ATR reactor. The temperature profile of both ATR and WGS in figure 98 further illustrates the longer time required to reach steady state.

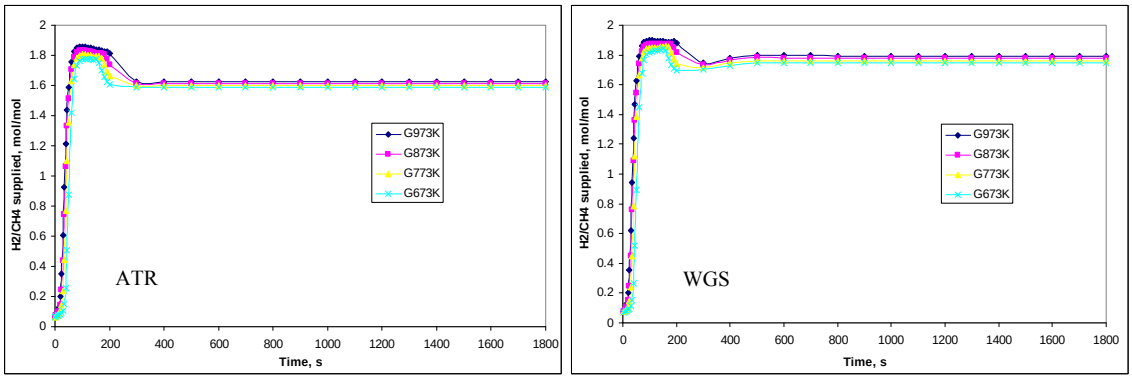

Figure 96: H_2 at various inlet gas temperatures for ATR-WGS cold start (case 1)

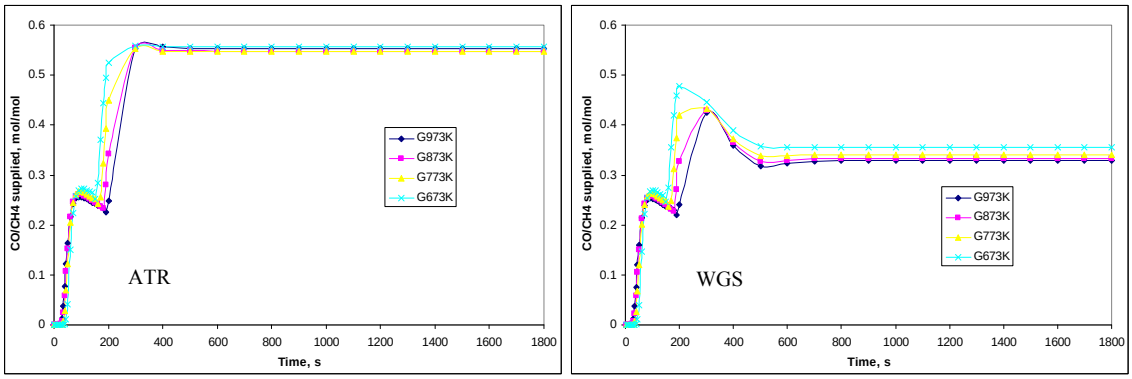

Figure 97: CO at various inlet gas temperatures for ATR-WGS cold start (case 1)

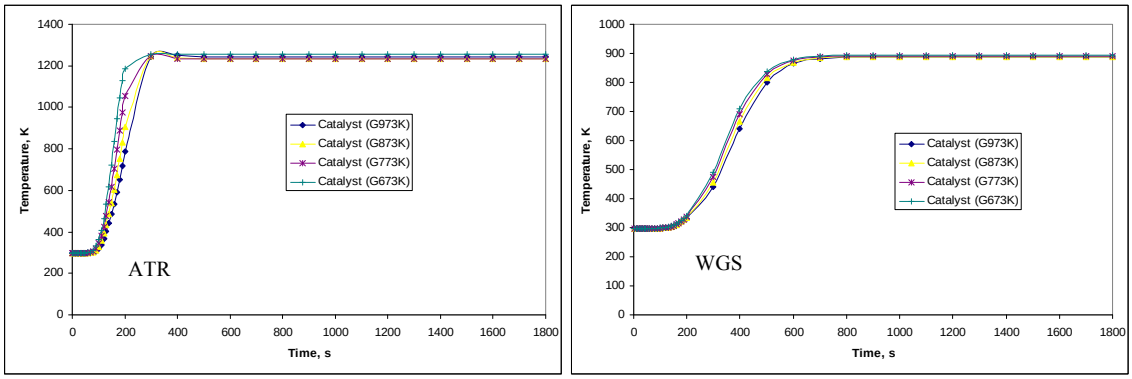

Figure 98: Reactor temperature profile at various inlet gas temperatures for ATR-WGS cold start (case 1)

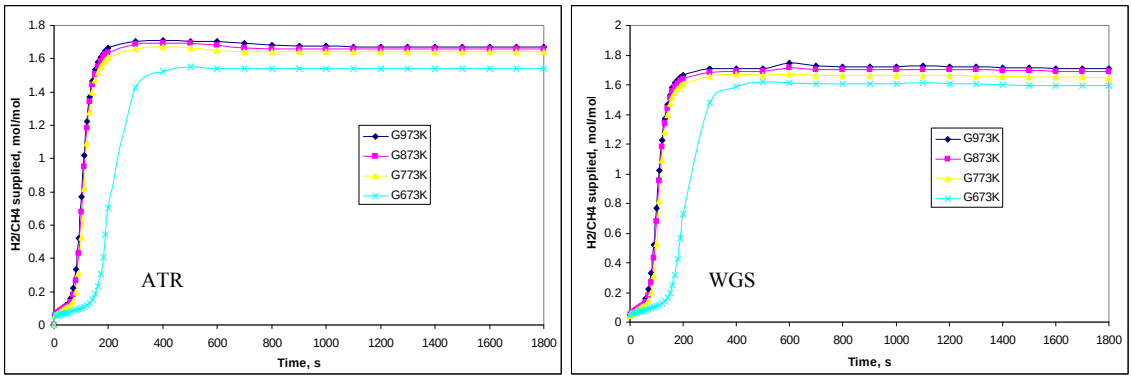

Figure 99: H_2 at various inlet gas temperatures for ATR-WGS cold start (case 2)

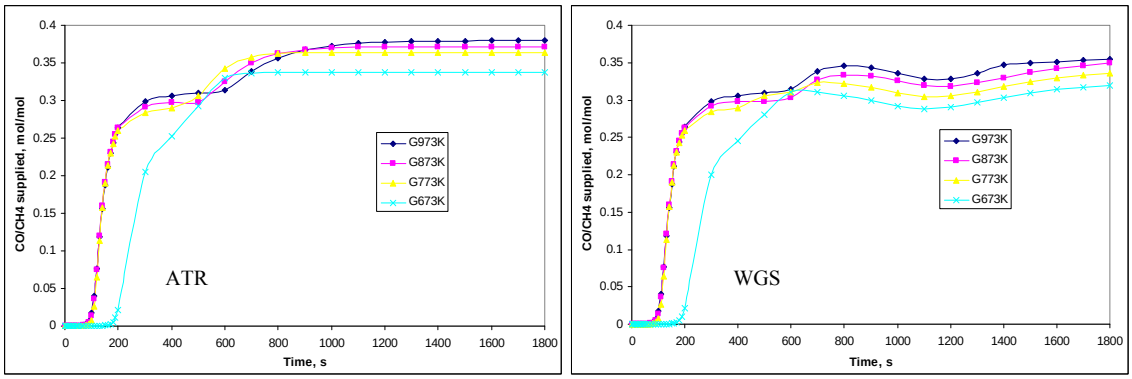

Figure 100: CO at various inlet gas temperatures for ATR-WGS cold start (case 2)

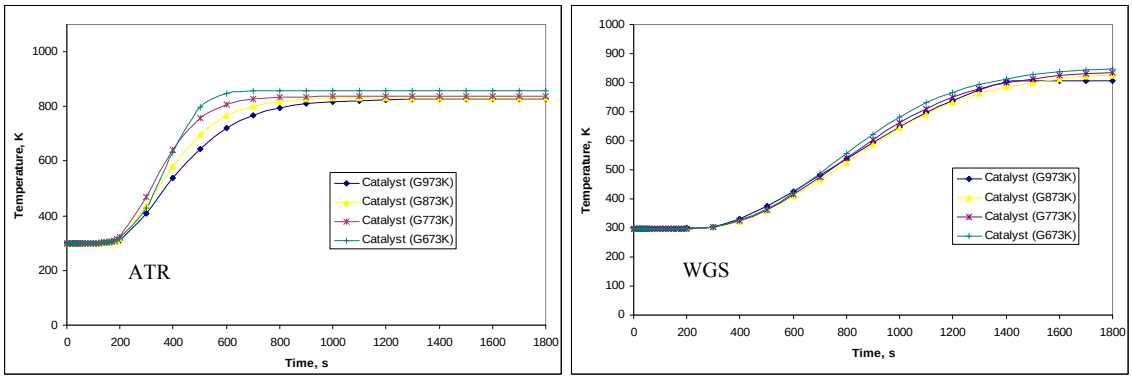

Figure 101: Reactor temperature profile at various inlet gas temperatures for ATR-WGS cold start (case 2)

The cold start behaviour of ATR-WGS reactor with operating conditions stated for case 2 in Table 17 is shown in figure 99 to 101. The results for ATR had been shown and explained in the cold start section of ATR and will not be discussed any further.

With the WGS integrated, the reformate shows a slightly higher H_2 yield and a lower CO; the difference in H_2 and CO is 0.04-0.05 mole and 0.02-0.03 mole, respectively, for the range of different inlet gas temperature studied. It is also observed that there is a slight dip in CO between 750 secs and 1200 secs before increasing gradually. This abnormal behaviour is credited to the temperature of the WGS catalyst which is still unsteady. Due to the unsteady catalyst temperature, it could be that the temperature during the period between 750 and 1200 secs is the favourable temperature for better WGS reaction and thus improved CO reduction and H_2 yield.

In addition, it is noted that for period studied, the ATR-WGS reactor has yet to reach steady state. It is estimated that it would take another 300 secs for the ATR-WGS reactor to reach steady state. The temperature profile of both ATR and WGS in figure 101 further illustrates the longer time required to reach steady state.

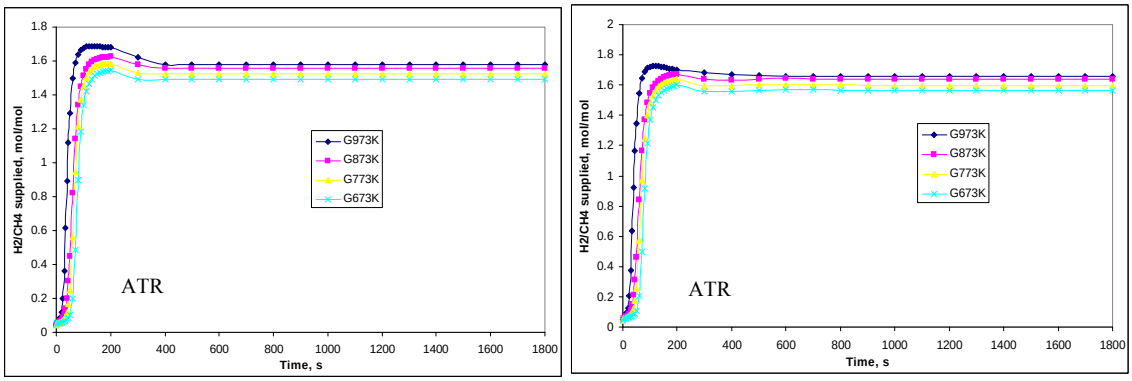

Figure 102: H_2 at various inlet gas temperatures for ATR-WGS cold start (case 3)

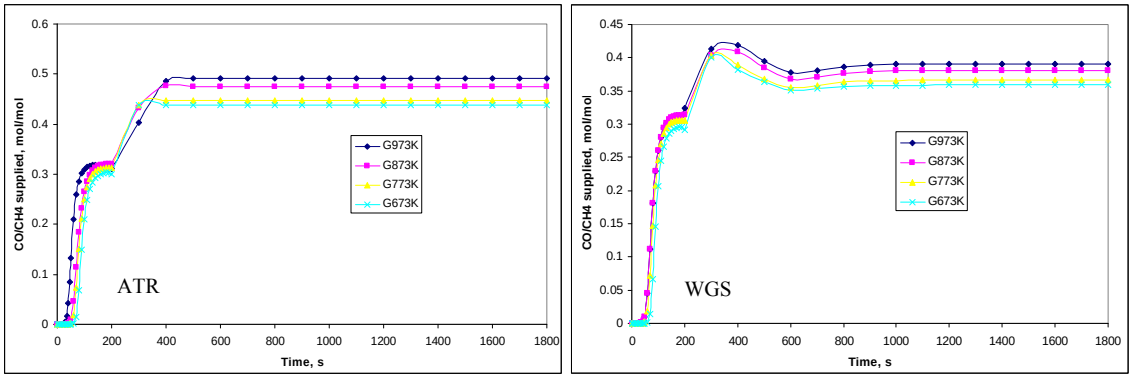

Figure 103: CO at various inlet gas temperatures for ATR-WGS cold start (case 3)

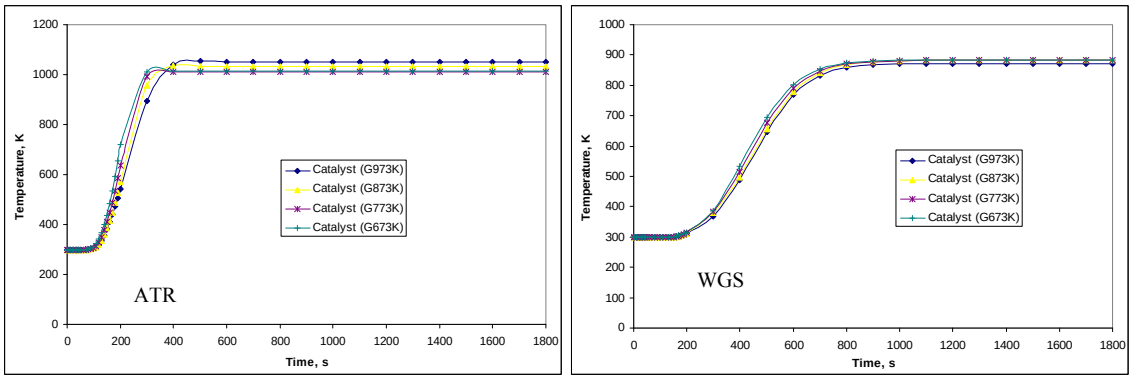

Figure 104: Reactor temperature profile at various inlet gas temperatures for ATR-WGS cold start (case 3)

The results of the third case study are presented in figure 102 to 104. The ATR results show an initial increase in H_2 yield follow by a drop in H_2 before reaching steady state. Similarly, the CO in ATR experiences a sharp increase and suffers a drop before increasing sharply with a slight overshoot to reach the steady state. The phenomenon that is observed in this result has already been explained in case 1, which runs at same flow rate but different AF and WF ratio.

However, in this case, the reformate of ATR-WGS reactor shows a difference of 0.07-0.08 mole and 0.08-0.1 mole in H_2 and CO, respectively, for the range of different inlet gas temperature studied.

The performance of WGS assisted ATR reactor for the 3 cases are summarised in the table 18 below:

Case	Flow rate (l/hr)	AF ratio	H_2 (ATR)	CO (ATR)	H_2 (WGS)	CO (WGS)	H_2 increase %	CO reduction %
1	**240**	**3.5**	1.589-1.620	0.557-0.547	1.744-1.793	0.329-0.356	9.75-10.68	36.09-39.85
2	**120**	**2.5**	1.539-1.669	0.337-0.380	1.591-1.711	0.320-0.349	2.75-3.13	5.188-7.96
3	**240**	**2.5**	1.490-1.577	0.438-0.490	1.564-1.659	0.359-0.391	4.96-5.14	18.01-20.29

Table 18: Summary of ATR-WGS cold start study

From this table, we can see that case 1 has the highest H_2 increment, CO reduction. This is followed by case 3 and 2. In absolute values, case 1 produced highest H_2 yield, followed by case 2 and 3. In terms of absolute values of CO, case 2 has the lowest CO followed by case 1 and 3.

Consequently, the author can conclude from these results that the performance of WGS assisted ATR depends on the heating rate of WGS catalyst and the flow rate supplied. For a fixed operation period, higher flow rate is required to bring the WGS catalyst to its light-off temperature faster in order to obtain respectable gains. The results also highlight that different reactor size for ATR and WGS should be explored in order to operate each reactor at its optimised space velocity, as mentioned in the optimisation studies.

5.3.3.2 Transient study of water-gas shift assisted autothermal reforming

In this section, the performance of a WGS assisted ATR subjected to 3 different feedstock square-pulse flows is investigated. This study would show how the ATR-WGS reactor would respond to a critical change in feedstock flow rate. The operating conditions of the WGS assisted ATR are listed as follows:

ATR Reactor	
AF ratio:	2.5
WF ratio:	1
Catalyst temperature (K):	873
Gas inlet temperature (K):	423
Pressure (Bar):	1
Reactor radius (m):	0.015
Reactor length (m):	0.2
WGS Reactor	
Maximum inlet gas temperature (K):	873
Catalyst temperature (K):	873
Reactor radius (m):	0.015
Reactor length (m):	0.2

Table 19: Operating and geometric parameters of WGS-ATR for transient study

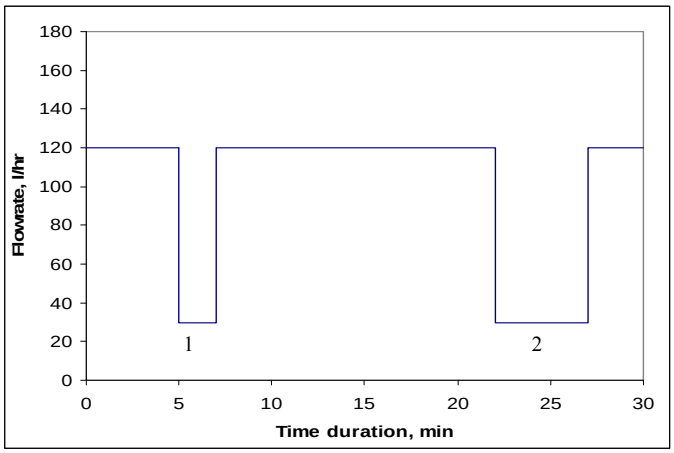

Figure 105: Pulse diagram of flow rate supplied (case 1)

As shown in figure 105, the WGS-ATR reformer is subjected to square-pulse flow rate change with two pulse changes. The first pulse is a small pulse with a pulse width of 2 min follow by a long dwell time of 15 min to isolate the interactions between the first and second pulse. The second pulse is a big pulse with pulse width of 5 min; this is followed by a short dwell of 2 min.

The transient results of the above case are shown below. The gauge to measure the transient performance at each pulse is taken to be the point at which the pulse takes place, i.e., for this case, at 300 and 1320 secs (5 and 22 minutes). Although extensive simulation results are available, only the product gas temperature, CH_4 conversion efficiency, H_2 yield and CO are discussed. In addition, to focus on the overshoot/undershoot of the above parameters during transients; the following study puts emphasis on the temporal variation of these parameters at the exit of the reformers.

It can be seen that when the WGS assisted ATR is subjected to a square-pulse change in flow rate from 120 l/hr to 30 l/hr and back to 120 l/hr, the overshoots (positive peaks) associated with larger pulse width (5 min) are much more severe than those with small pulse width (2 min). The product temperature of the ATR overshoots by 0.38 % (931.37 K prior to pulsing), H_2 overshoots by 4.16 % (1.32 prior to pulsing), CO overshoots by 7.03 % (0.313 prior to pulsing) and CH_4 conversion overshoots by 3.22 % (82.25 % prior to pulsing) for smaller pulse width as compared to the product temperature which overshoots by 2.06 % (928.36 K prior to pulsing), H_2 overshoots by 6.64 % (1.3 prior to pulsing), CO overshoots by 10.70 % (0.3 prior to pulsing) and CH_4 conversion overshoots by 5.07 % (80.57 % prior to pulsing) for larger pulse width. As for undershoots (negative peaks), all parameters show lower undershoot values in the case of bigger pulse width, i.e., gas temperature: 760.77 K (931.37 K prior to pulsing), H_2: 1.32 (1.32 prior to pulsing), CO: 0.16 (0.313 prior to pulsing) and CH_4 conversion: 79.94 % (82.25 % prior to pulsing) for smaller pulse width as against gas temperature: 679.28 K (928.36 K prior to pulsing), H_2: 1.28 (1.3 prior to pulsing), CO: 0.144 (0.3 prior to pulsing) and CH_4 conversion: 78.09 % (80.57 % prior to pulsing) for larger pulse width. In addition, it is observed that at each point of pulsing, there is an overshoot follow by an undershoot and overshoot again. For instance, in CO graph for the smaller pulse, there is a slight overshoot of 2.88 % before plunging to 47.92 % and recover with another overshoot of 7.03 %. This observed trend is true for all parameters except temperature. This case of study on ATR also indicates a number of interesting phenomena: (1) overshoot is more severe than undershoot during transients, (2) step decrease in flow rate

causes CO undershoot that would be beneficial on the subsequent CO cleanup, and (3) step increase in flow rate causes an temporal increase in CH_4 conversion and H_2.

In the WGS reformer, the shapes of the transient results are similar to that of ATR; the values of H_2 in WGS reformer are larger than that of ATR results while CO in WGS reformer are smaller than that of ATR results. However, it is noticed that the relative change of the amplitude during pulse change is either amplified or attenuated. This is evident when one compares the amplitude change of H_2 of WGS with ATR's. At the instance of pulsing, the first overshoot is larger and the second overshoot is smaller than what is seen in ATR results. For the CO, it is noted that there are some differences between the first pulse and the second pulse. In the first pulse, there is no overshoot (2.88% in ATR) before the CO plunge 56.34 % (47.92 % in ATR) and recover with another overshoot of 5.63 % (7.03 % in ATR) while in second pulse, there is an overshoot of 11.86 % (2.00 % in ATR) before plunging 17.00 % (51.84 % in ATR) and recover with an overshoot of 14.23 % (10.70 % in ATR). The difference in the transient behaviour between the first and second pulse can be attributed to the temperature of the WGS catalyst. From the WGS temperature graph, one can see that the occurrence of first pulse is in the unsteady state while the second pulse occurred when the temperature is at steady state. Therefore, we can draw the conclusion that the differences in the transient behaviour of the two pulses are due to state of the WGS catalyst temperature.

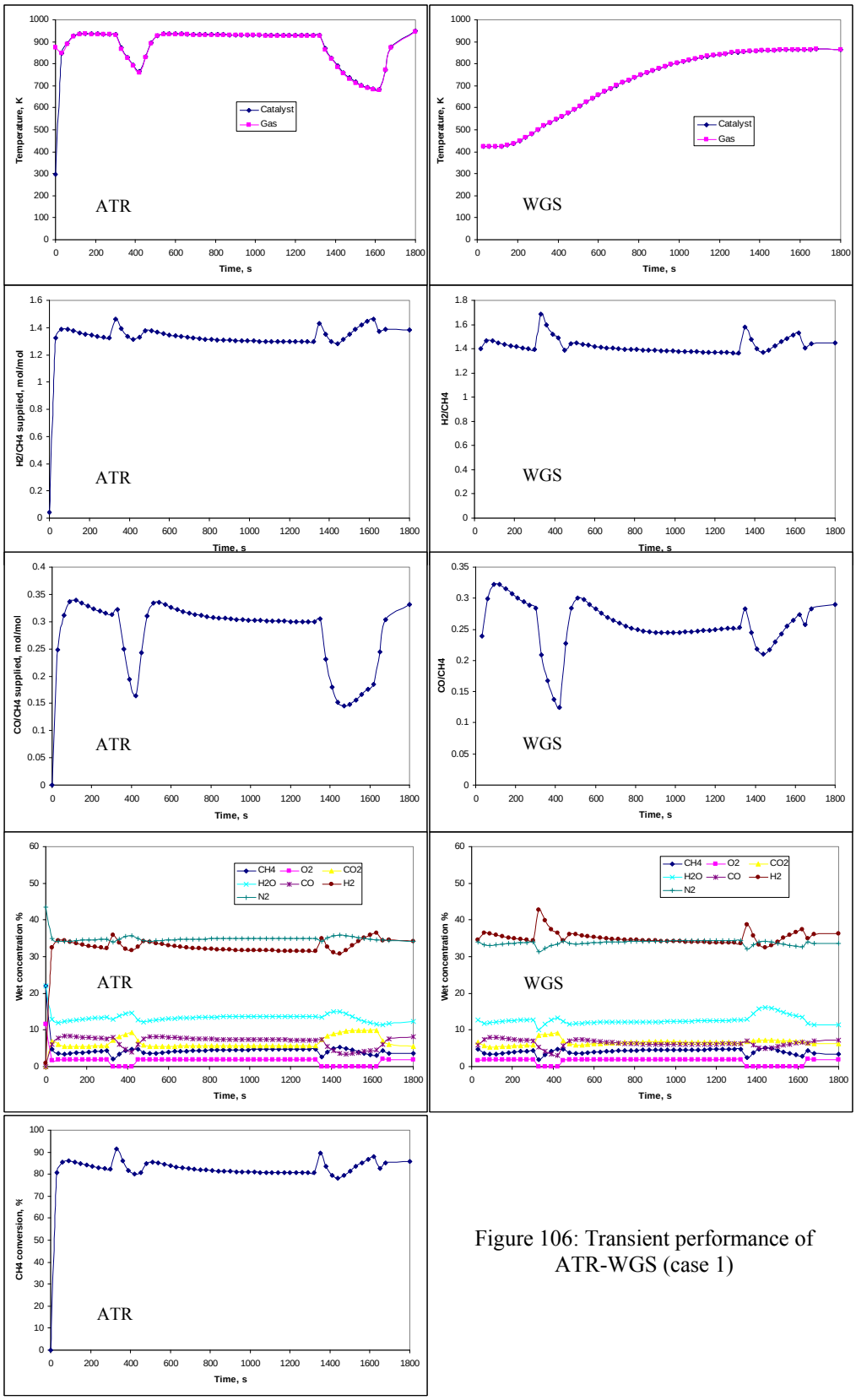

Figure 106: Transient performance of ATR-WGS (case 1)

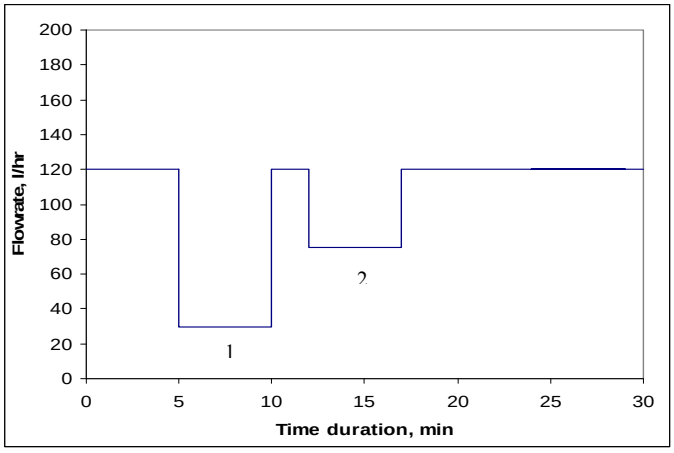

Figure 107: Pulse diagram of flow rate supplied (case 2)

In the second case, the WGS-ATR reformer is subjected to square-pulse flow rate change with two pulse changes as shown in figure 107. The first pulse is a big pulse with a pulse width of 5 min follow by a long dwell time of 2 min. The second pulse, which has half the amplitude of the first pulse, is a big pulse with pulse width of 5 min. This case study would serve the purpose of understanding the transient behaviour due to 2 closely time-spaced step pulse change with different amplitude.

The results of this case study are shown in the figures below. It is noted that 2 min of dwell time is sufficient to resolve the two pulses clearly. There are very slight overshoots of performance parameters in the first pulse as they have already been picked up by the second pulse effect before they could increase further. Results clearly indicate that the bigger the pulse step, the more overshoot/undershoot one would encounter. In addition, it is found that the production of H_2 stabilised faster than production of CO after a step change by 60 to 90 secs, which could be due to a combined effect of gas diffusivity

difference and reaction mechanisms. Also, it is noticed that the relative change of CO in WGS (negative peak at 19% versus 7.40% in ATR) is larger for the second pulse change as opposed to what was observed in the first case study. Furthermore, it is observed that the combination of a large pulse width and a small pulse width step change prolonged the time that the WGS reactor required to reach steady state. Other than these observations, the phenomenon that occurred in this case study is the same as case 1.

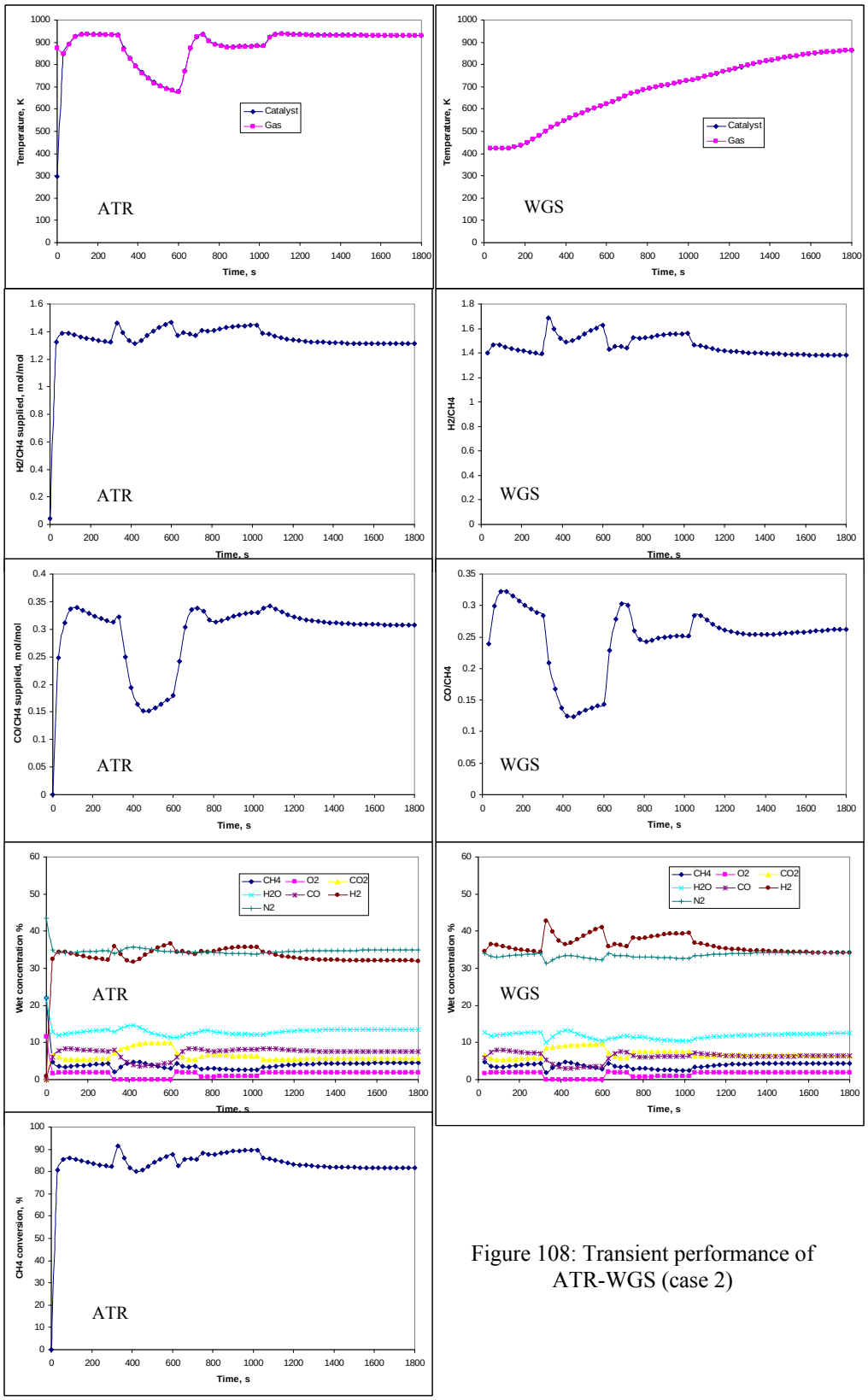

Figure 108: Transient performance of ATR-WGS (case 2)

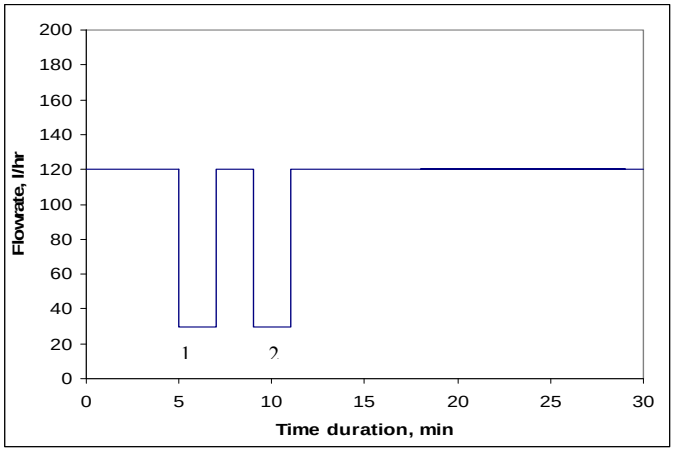

Figure 109: Pulse diagram of flow rate supplied (case 3)

In the final case, the WGS-ATR reformer is subjected to square-pulse flow rate change with two close pulse changes. Both pulses are a small pulse with a pulse width of 2 min with a short dwell of 2 min in between, which is similar to case 2, except that both pulses have the same amplitude. With this case study performed, the transient behaviour of 2 closely time-spaced pulse changes with same amplitude can be observed and analysed.

From the results obtained, it is clear that the short dwell between the 2 pulse change is sufficient to separate the effects between them; the performance parameters in the first pulse was given enough time to respond (evident by the slight overshoot in H_2 after the first pulse change) since the pulse width of first pulse is only 2 min. The shape of the ATR transient behaviour in second pulse is similar to the first pulse; however, the relative change in magnitude is considerably smaller than the first pulse change. In the WGS, the transient behaviour is identical for both pulse change in the CO curve; the undershoots and negative peaks are amplified while the overshoots are attenuated.

Based on the above three cases of study, the author could summarise that the overshoot/undershoot of the performance parameters at any point of time during transients are closely related to the temperature and, may be, the water concentration as the latter has high specific heat that would affect the "stored energy" of the WGS assisted ATR reactor and thus the gas temperature for reactions. One can also see that the WGS reactor amplified/attenuated the values of performance parameters although the shape of the performance parameters remains similar to the ATR reactor. Besides these, it is interesting to note that there is a momentarily increase in H_2 yield and CH_4 conversion with a sharp drop in CO during a step down change. Although the situation is reversed during the step up change, the relative decrement in the H_2 yield and increment in CO is smaller as compared to the relative change during step down change. This could imply that pulsating feedstock could generate much higher H_2 with lower CO.

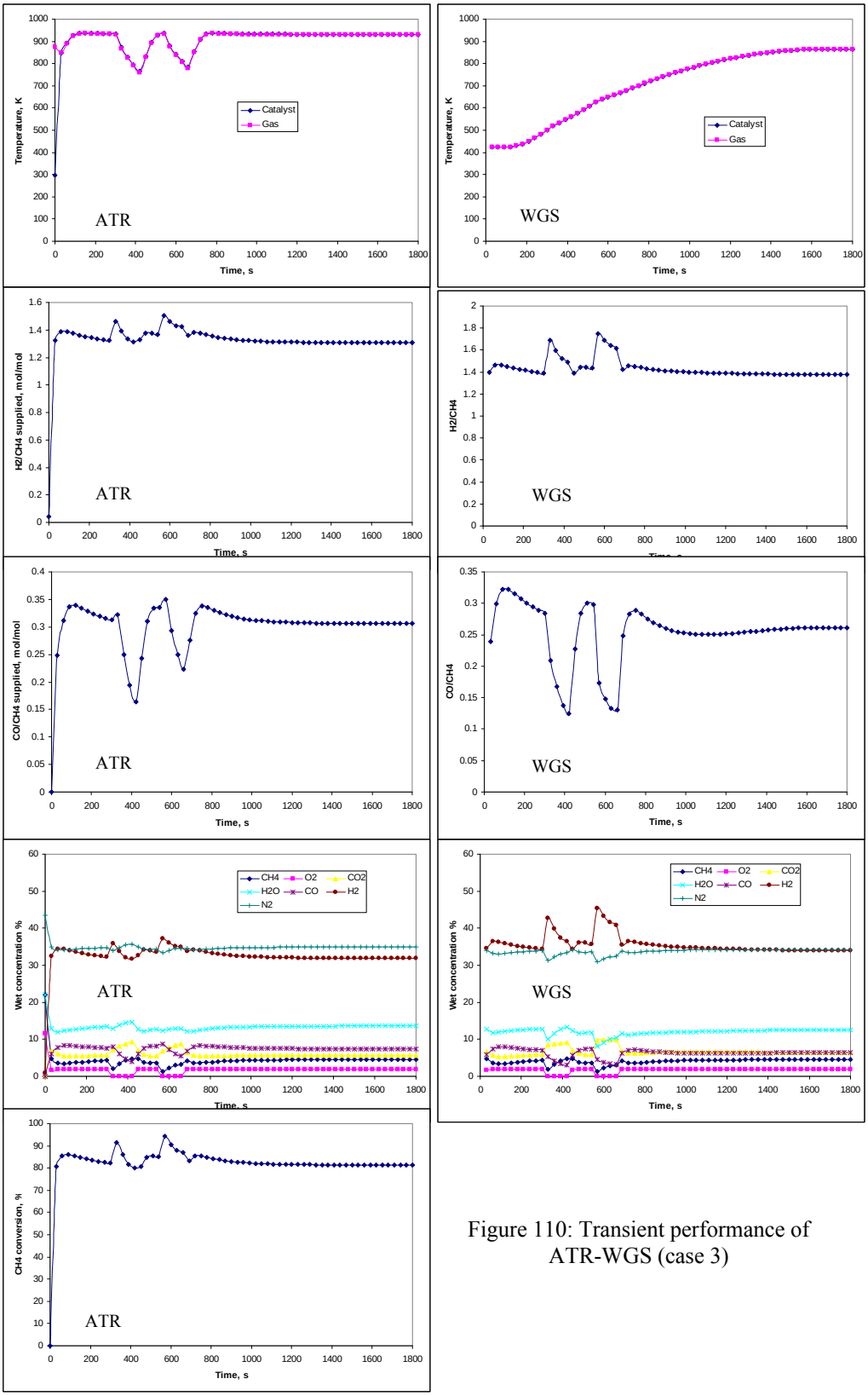

Figure 110: Transient performance of ATR-WGS (case 3)

6 Conclusions and recommendations

A project has been carried out to study the behaviour of water-gas shift (WGS) assisted autothermal reforming (ATR), which is essentially a combined process of steam reforming (STR) and partial oxidation (POX) processes under thermal-neutral condition, to enhance the concentration of hydrogen product without any external heat supply to the reformer. A comprehensive study of ATR, WGS and WGS-assisted ATR reformer which covers literature reviews, equilibrium study, design and fabrication works, experiments and mathematical modelling was successfully completed to achieve this purpose.

Experiments and thermodynamic analysis of STR, POX and ATR have been carried out to understand the complex relationships in the processes. From these experimental results, the kinetics of each process was extracted to perform 2-D simulation of ATR, WGS and ATR-WGS, which agreed with the experimental results well.

In the mathematical modelling, additional considerations such as the non-plug flow gas velocity profile, the catalyst porosity profile, diffusion of gases into and out of the porous catalyst pallets, heat transfer along the wall and gas-to-wall heat transfer were included to make the comprehensive simulation model unique and closer to reality. In addition, further studies on cold start study and transient performance of ATR were performed to understand the dynamic changes of the composition and temperature in the reactor during the cold start and transient operations as there are no studies done.

Using the simulation model, parameter studies of ATR and WGS were performed and its results were used to optimise each reaction process. Under current reactor design, the recommended space velocity for ATR to have high H_2 and moderately low CO is around 300 hr^{-1}. For WGS, it determined that the optimum range of space velocity is between 106.09 hr^{-1} and 212.18 hr^{-1}. However, it should be noted WGS is more temperature sensitive. Hence, it should operate between 873 and 973 K. Cold start time for ATR-WGS reactor was found to be longer than ATR reactor due to the addition of a slower WGS process. It was also observed that WGS plays an important role in the final products of the reaction. In addition to these findings, an investigation in the transient performance of a WGS assisted ATR, subjected to different feedstock square-pulse flows, showed that there are serious overshoot/undershoot of performance related parameters in the transients, whose values are quite different from those under steady state conditions. The overshoot/undershoot of the performance parameters during transients are closely related to temperature and, may be, water concentration as the latter has high specific heat that would affect gas temperature for reactions. Results also showed that there is a momentarily increase in H_2 and CH_4 conversion with a sharp drop in CO during a step down change. Although the situation is reversed during the step up change, the relative decrement in the H_2 and increment in CO is smaller as compared to the relative change during step down change. Such results could imply that pulsing feedstock could generate much higher H_2 with lower CO.

From the findings and work done, the achievements of this research are summarised as follows:

- Comprehensive study of ATR, WGS and ATR-WGS reaction
- Inclusion of velocity profile, catalyst porosity profile and diffusion of gas in porous catalyst in the non plug flow, 2-D simulation model
- Obtain kinetics of ATR and WGS reaction
- Parameter studies on ATR and WGS reaction
- Optimisation of ATR and WGS reactor
- Cold start study on ATR-WGS reactor
- Transient study on ATR-WGS reactor

In conclusion, the project on the development and optimization of WGS assisted ATR with methane as gas feed had been successfully completed which allows us to have better understanding on the complexity of the integrated system. In addition, it is concluded that the reforming models developed in this study can replicate the characteristics of the reformer under different operating conditions and parameters related to the transport phenomena occurred in the reformer.

Although a comprehensive study on WGS-assisted ATR had been performed, there are areas which can be improved or included to make the study more comprehensive. The author recommends developing the current kinetic model into a full 2-D model, which considers the momentum equation and pressure distribution in the model. With these

additional considerations, the velocity, temperature and concentration profile in the radial direction can be predicted more accurately and closer to reality.

7 References

1. The electric revolution, Leaders, The Economist Newspaper Limited, 5th August 2000
2. The dawn of micropower, Science and Technology, The Economist Newspaper Limited, 5th August 2000
3. Sustainable development - A few green shoots, Science & Technology, The Economist Newspaper and The Economist Group, 29th August 2002, Story ID No.1301796
4. A real energy policy? Or just hot air?, Professional Engineering, Volume 16 Number 5, Pg36 – 37, 12th March 2003
5. W.W. Clark II, E. Paolucci, J. Copper, Commercial development of energy – environmentally sound technologies for the auto-industry: the case of fuel cells, *J. Cleaner Production* **11**, pg.427-437, 2003
6. S. Sawayama, N. Yokota, Development of highly efficient hydrogen-methane fermentation process using organic wastes, in 15th Hydrogen Energy Conference proceedings, Yokohama, 2004
7. Y. Ueno, H. Fukui, M. Goto, Hydrogen fermentation from organic waste, in 15th Hydrogen Energy Conference proceedings, Yokohama, 2004
8. P.D. Clausen, D.H. Wood, Research and development issues for small wind turbines, *Renewable Energy* **16**, pg.922-927, 1999
9. R. Sebastian, J. Quesada, Distributed control system for frequency control in a isolated wind system, *Renewable Energy* **31**, pg.285-305, 2006

10. A. Thakker, F. Hourigan, Modeling and scaling of the impulse turbine for wave power applications, *Renewable Energy* **29**, pg.305-317, 2004
11. A.A. Temeev, V.P. Belokopytov, S.A. Temeev, An integrated system of the floating wave energy converter and electrolytic hydrogen producer, *Renewable Energy* **31**, pg.225-239, 2006
12. M.G. Goumas, V.A. Lygerou, L.E. Papayannakis, Computational methods for planning and evaluating geothermal energy projects, *Energy Policy* **27**, pg.147-154, 1999
13. I.B. Fridleifsson, Geothermal energy for the benefit of the people, *Renewable & Sustainable Energy Reviews* **5**, pg.299-312, 2001
14. U. Bach, D. Lupo, P. Comte, J.E. Moser, F. Weissortel, J. Salbeck, H. Spreitzer, M. Gratzel, Solid-state dye-sensitized mesoporous TiO_2 solar cells with high photon-to-electron conversion efficiencies, *Nature* **395**, pg.583-585, 1998
15. C.J. Brabec, N.S. Sariciftci, J.C. Hummelen, Plastic solar cells, *Advanced Functional Materials* **11(1)**, pg.15-26, 2001
16. C. Song, Fuel processing for low-temperature and high-temperature fuel cells: Challenges and opportunities for sustainable development in the 21st century, *Catalysis Today* **77**, pg.17-49, 2002
17. Bush touts hydrogen fuel cells, People and Technology, 7th February 2003, Page ID No. news070203-03
18. US and Europe enter into fuel cell agreement, Professional Engineering, Volume 16 Number 11, pg.11, 25th June 2003

19. Singapore Initiative in New Energy Technology (SINERGY), Singapore Economic Development Board, April 2002

20. SINERGY – A synergy of innovation and development, Singapore Investment News, SINERGY supplement, Singapore Economic Development Board, Pg 2, April 2002

21. NTU's green energy initiative, Singapore Investment News, SINERGY supplement, Singapore Economic Development Board, Pg 7, April 2002

22. S.S. Penner, Steps toward the hydrogen economy, *Energy* **31**, pg.33-43, 2006

23. S. Freni, G. Calogero, S. Cavallaro, Hydrogen production from methane through catalytic partial oxidation reactions, *J. Power Sources* **87**, pg.28-38, 2000

24. S. Galli, E. Calo, G. Monteleone, E. Mancini, Hydrogen production by reforming in fixed-bed catalytic reactor, in 15th World Hydrogen Energy Conference proceedings, Yokohama, 2004

25. K. Otsuka, S. Takenaka, H. Ohtsuki, Production of pure hydrogen through catalytic decomposition of methane on supported-Ni based catalysts by cyclic oxidative-activation of the catalyst, in 15th World Hydrogen Energy Conference proceedings, Yokohama, 2004

26. T. Nozaki, N. Muto, S. Kado, K. Okazaki, Dissociation of vibrationally excited methane on Ni catalyst. Part 1. Application to methane steam reforming, *Catalysis Today* **89**, pg.57-65, 2004

27. K. Shimizu, M. Fukagawa, A. Sakanishi, Development of PEM water electrolysis type hydrogen production system, in 15th Hydrogen Energy Conference proceedings, Yokohama, 2004

28. D. Frank, J. Cargnelli, J. Dogterom, A. Rusta-Sallehy, Status of proton exchange water electrolysis development at hydrogenics, in 15th Hydrogen Energy Conference proceedings, Yokohama, 2004

29. M. Lennartz, M. Lopez, H. Dziallas, S. Hori, MEA technology for PEM-water-electrolysis, in 15th Hydrogen Energy Conference proceedings, Yokohama, 2004

30. M. Laniecki, R. Glowacki, Photocatalysis as a tool in hydrogen generation, in 15th Hydrogen Energy Conference proceedings, Yokohama, 2004

31. C.A. Linkous, D.K. Slattery, M.E. Mraz, Hydrogen production via photocatalysis. Catalysis of O_2 evolution, in 15th Hydrogen Energy Conference proceedings, Yokohama, 2004

32. H. Aoki, H. Kaneko, N. Hasegawa, H. Ishihara, Y. Takahashi, A. Suzuki, Y. Tamaura, Solar H_2 production with two-step water splitting of $NiFe_2O_4$ using concentrated solar heat, in 15th Hydrogen Energy Conference proceedings, Yokohama, 2004

33. K. Fujihara, T. Ohno, M. Matsumura, Splitting of water by electrochemical combination of two photocatalytic reactions in TiO_2 particles, *J. Chem. Soc., Faraday Trans.* **24**, pg.3705-3709, 1998

34. K. Sayama, H. Arakawa, Effect of carbonate salt addition on the photocatalytic decomposition of liquid water over Pt-TiO_2 catalyst, *J. Chem. Soc., Faraday Trans.* **8**, pg.1647-1654, 1997

35. E. Borgarello, J. Kiwi, E. Pelizzetti, M. Visca, M. Gratzel, Photochemical cleavage of water by photocatalysis, *Nature* **289**, pg.158-160, 1981

36. S. Sato, J.M. White, Photodecomposition of water over Pt/TiO_2 catalysts, *Chem. Phys. Lett.* **72**, pg.83-86, 1980

37. J.R. Benemann, A photobiological hydrogen production process, in 15th Hydrogen Energy Conference proceedings, Yokohama, 2004

38. Y. Asada, J. Miyake, Photobiological hydrogen production, *J. Bioscience and Bioengineering* **88(1)**, pg.1-6, 1999

39. T. Mizuno, Y. Tanaka, Anomalous hydrogen generation by plasma electrolysis, in 15th Hydrogen Energy Conference proceedings, Yokohama, 2004

40. C.H. Chien, I.C. Tseng, W.L. Wu, C.Y. Chang, Y.F. Liu, Characterization of hydrogen producing microbial community in the bio-hydrogen reactors, in 15th Hydrogen Energy Conference proceedings, Yokohama, 2004

41. Y. Ueno, H. Fukui, M. Goto, Hydrogen fermentation from organic waste, in 15th Hydrogen Energy Conference proceedings, Yokohama, 2004

42. S. Sawayama, N. Yokota, Development of highly efficient hydrogen-methane fermentation process using organic wastes, in 15th Hydrogen Energy Conference proceedings, Yokohama, 2004

43. Y.B. Chang, T.Y. Jeong, G.C. Cha, S.H. Kim, I.K. Yoo, D.J. Kim, H_2 production from livestock wastewater by rhodobacter sphaeroides, in 15th Hydrogen Energy Conference proceedings, Yokohama, 2004

44. J.R. Rostrup-Nielsen, Conversion of hydrocarbons and alcohols for fuel cells, *Physical Chemistry Chemical Physics* **3**, pg.283-288, 2001

45. F. Gallucci, L. Paturzo, A. Basile, A simulation study of the steam reforming of methane in a dense tubular membrane reactor, *IJHE* **29**, pg.611-617, 2004

46. T. Ioannides, Thermodynamic analysis of ethanol processors for fuel cell applications, *J. Power Sources* **92**, pg.17-25, 2001

47. S. Lin, M. Harada, Y. Suzuki, H. Hatano, Continuous experiment regarding hydrogen production by coal/CaO reaction with steam (I) gas products, *Fuel* **83**, pg.869-874, 2004

48. A. E. Lutz, R.W. Bradshaw, J.O. Keller, D.E. Witmer, Thermodynamic analysis of hydrogen production by steam reforming, *IJHE* **28**, pg.159-167, 2003

49. E. Achenbach, E. Riensche, Methane/steam reforming kinetics for solid oxide fuel cells, *J. Power Sources* **52**, pg.283-288, 1994

50. A.L. Dicks, K.D. Pointon, A. Siddle, Intrinstic reaction kinetics of methane steam reforming on a nickel/zirconia anode, *J. Power Sources* **86**, pg.525-530, 2000

51. N.A. Darwish, N. Hilal, G. Versteeg, B. Heesink, Feasibility of the direct generation of hydrogen for fuel-cell-powered vehicles by on-board steam reforming of naphtha, *Fuel* **83**, pg.409-417, 2004

52. J. Han, I.S. Kim, K.S. Choi, High purity hydrogen generator for on-site hydrogen production, *IJHE* **27**, pg.1043-1047

53. T. Asakura, T. Tanaka, T. Tanaka, T. Azuma, Development of new compact hydrogen production systems from natural gas, in 15th Hydrogen Energy Conference proceedings, Yokohama, 2004

54. K. Venkataraman, E.C. Wanat, L.D. Schmidt, Steam reforming of methane and water-gas shift in catalytic wall reactors, *AIChE Journal* **49(5)**, pg.1277-1284, 2003

55. L.D. Schmidt, D.A. Hickman, Synthesis gas formation by direct oxidation of methane over Pt monoliths, *J. Catalyst* **138**, pg.267, 1992

56. A.K. Avel, D.L. Trimm, Z.I. Onsan, Quantitative investigation of catalytic natural gas conversion for hydrogen fuel cell applications, *Chem. Engrg. Journal* **4027**, pg.1-11, 2002

57. J. Zhu, D. Zhang, K.D. King, Reforming of CH_4 by partial oxidation: thermodynamic and kinetic analyses, *Fuel* **80**, pg.899-905, 2001

58. S.E. Voltz, C.R. Morgan, D. Liederman, S.M. Jacob, Kinetic study of carbon monoxide and propylene oxidation on platinum catalysts, *I & EC Prod. Res. Dev.* **12**, pg.294, 1973

59. N. Muradov, C. Huang, A. T-raissi, F. Smith, Hydrogen production from natural gas with reduced CO_2 emissions, in 15th Hydrogen Energy Conference proceedings, Yokohama, 2004

60. V.R. Choudhary, A.M. Rajput, B. Prabhakar, A.S. Mamman, Partial oxidation of methane to CO and H_2 over nickel and/or cobalt containing ZrO_2, ThO_2, UO_2, TiO_2 and SiO_2 catalysts, *Fuel* **77(15)**, pg.1803-1807, 1998

61. S.H. Chan, H.M. Wang, Thermodynamic analysis of natural-gas fuel reforming for fuel cell applications, *IJHE* **25**, pg.441 – 449, 2000

62. S. Ayabe, H. Omoto, T. Utaka, R. Kikuchi, K. Sasaki, Y. Teraoka, K. Eguchi, Catalytic autothermal reforming of methane and propane over supported metal catalysts, *Applied Catalysis A:General*, **241**, Issues 1-2,pg.261 – 269, 2003

63. A. Qi, S. Wang, D. Wu, On-board hydrogen generator by autothermal reforming of gasoline for PEMFC, in 15th World Hydrogen Energy Conference proceedings, Yokohama, 2004

64. S.H. Chan, H.M. Wang, Carbon monoxide yield in natural gas autothermal reforming process, *J. Power Sources* **101**, pg.188 – 195, 2001

65. S.H. Chan, H.M. Wang, Effect of natural gas composition on autothermal fuel reforming products, *Fuel Processing Technology* **64**, pg221 – 239, 2000

66. D.H. Kim, M.S. Lim, Kinetics of selective CO oxidation in hydrogen-rich mixtures on Pt/alumina catalysts, *Applied Catalysis A: General* **224**,pg.27-38, 2002

67. L.F. Brown, A comparative study of fuels for on-board hydrogen production for fuel-cell-powered automobiles, *IJHE* **26**, pg.381-397, 2001

68. R.M. Laine, E.J. Crawford, Homogenous catalysis of the water-gas shift reaction, *J. Molecular Catalysis* **44**, pg.357-387, 1988

69. G.C. Wang, L. Jiang, Y.H. Zhou, Z.S. Cai, Y.M. Pan, X.Z. Zhao, Y.W. Li, Y.H. Sun, B. Zhong, X.Y. Pang, W. Huang, K.C. Xie, Investigation of the kinetic properties for the forward and reverse WGS reaction by energetic analysis, *Theochem* **634**, pg.23-30, 2003

70. N.A. Koryabkina, A.A. Phatak, W.F. Ruettinger, R.J. Farrauto, F.H. Ribeiro, Determination of kinetic parameters for the water-gas shift reaction on copper catalysts under realistic conditions for fuel cell applications, *JCat* **217**, pg.233-239, 2003

71. Y.T. Choi, H.G. Stenger, Water gas shift reaction kinetics and reactor modeling for fuel grade hydrogen, *J. Power Sources* **124**, pg.432-439, 2003

72. T. Salmi, R. Hakkarainen, Kinetic study of the low-temperature water-gas shift reaction over a Cu-ZnO catalyst, *Applied Catalysis* **49**, pg. 285-306, 1989

73. A.Y. Tonkovich, J.L. Zilka, M.J. LaMont, Y. Wang, R.S. Wegeng, Microchannel reactors for fuel processing applications. I. Water gas shift reactor, *Chem. Engrg. Sci.* **54**, pg. 2947-2951, 1999

74. J. Patt, D.J. Moon, C. Phillips, L. Thompson, Molybdenum carbide catalysts for water-gas shift, *Catalysis Letters* **65**, pg. 193-195, 2000

75. Y. Li, Q. Fu, M. Flytzani-Stephanopoulos, Low-temperature water-gas shift reaction over Cu- and Ni-loaded cerium oxide catalysis, *Applied Catalysis B: Environmental* **27**, pg. 179-191, 2000

76. M. Saito, I. Takahara, K. Murata, M. Inaba, K. Tomoda, The water-gas shift reaction over Cu/ZnO-based multicomponent catalysts, in 15th World Hydrogen Energy Conference proceedings, Yokohama, 2004

77. T. Tabakova, V. Idakiew, D. Andreeva, I. Mitov, Influence of the microscopic properties of the support on the catalytic activity of Au/ZnO, Au/ZrO_2, Au/Fe_2O_3-ZnO, Au/Fe_2O_3-ZrO_2 catalysts for the WGS reaction, *Applied Catalysis A: General* **202(1)**, pg.91-97, 2000

78. T. Himeno, M. Hoshino, T. Sekiba, Y. Iwasaki, M. Sakurai, H. Kameyama, Selective CO oxidation using an anodic oxidized aluminium catalyst for PEMFCs, in 15th Hydrogen Energy Conference proceedings, Yokohama, 2004

79. C.D. Dudfield, R. Chen, P.L. Adcock, A carbon monoxide PROX reactor for PEM fuel cell automotive application, *IJHE* **26**, pg.763-775, 2001

80. S.H. Lee, J. Han, K.Y. Lee, Development of 10-kWe preferential oxidation system for fuel cell vehicles, *J. Power Sources* **109**, pg.394-402, 2002

81. O. Korotkikh, R. Farrauto, Selective catalytic oxidation of CO in H_2: fuel cell applications, *Catalysis Today* **62**, pg.249-254, 2000

82. Y. Choi, H.G. Stenger, Kinetics, simulation and insights for CO selective oxidation in fuel cell applications, *J. Power Sources* **129**, pg.246-254, 2004

83. M.J. Kahlich, H.A. Gasteiger, R.J. Behm, Kinetics of the selective CO oxidation in H_2-rich gas on Pt/Al_2O_3, *J. Catalysis* **171**, pg.93-105, 1997

84. R.C. Shishu, Kinetics of carbon-monoxide oxidation over platinum catalyst, University of Detroit, 1972

85. B. Rohland, V. Plzak, The PEMFC-integrated CO oxidation – a novel method of simplifying the fuel cell plant, *J. Power Sources* **84**, pg. 183-186, 1999

86. P.V. Snytnikov, V.A. Sobyanin, V.D. Belyaev, P.G. Tsyrulnikov, N.B. Shitova, D.A. Shlyapin, Selective oxidation of carbon monoxide in excess hydrogen over Pt-, Ru- and Pd-supported catalyst, *Applied Catalysis A: General* **239**, pg. 149-156, 2003

87. E.L. Sughrue, C.H. Bartholomew, Kinetics of carbon monoxide methanation on nickel monolithic catalysts, *Applied Catalysis* **2**, pg.239-256, 1982

88. K. Ledjeff-Hey, J. Roes, R. Wolters, CO_2-scrubbing and methanation as purification system for PEFC, *J. Power Sources* **86**, pg. 566-561, 2000

89. O. Gorke, P. Pfeifer, K. Schubert, Highly selective methanation by the use of a microchannel reactor, *Catalysis Today* **110**, pg.132-139, 2005

90. S. Uemiya, N. Sato, H. Ando, E. Kikuchi, The water gas shift reaction assisted by a palladium membrane, *Ind. Eng. Chem. Res.* **30**, pg. 585-589, 1991

91. E. Kikuchi, Y. Nemoto, M. Kajiwara, Steam reforming of methane in membrane reactors: comparison of electroless-plating and CVD membranes and catalyst packing modes, *Catalysis Today* **56**, pg.75-81, 2000

92. A. Criscuoli, A. Basile, E. Drioli, O. Loiacono, An economic feasibility study for water gas shift membrane reactor, *J. Membrane Sci.* **181**, pg.21-27, 2001

93. A.S. Lamine, G. Wild, M. Nilles, H. Martin, Heat transfer in heated tubular packed bed reactors with gas or liquid flow, in Heat and mass transfer in porous media, Elsevier, 1992

94. D. Vortmeyer, E. Haidegger, Wall heat transfer in cooled tubular reactors (interaction with flow distribution), in Heat and mass transfer in porous media, Elsevier, 1992.

95. J.N. Papageorgiou, G.F. Froment, Simulation models accounting for radial voidage profiles in fixed-bed reactors, *Chem. Eng. Sc.* **50**, pg.3043, 1995

96. K. Schnitzlein, Modelling radial dispersion in terms of the local structure of packed beds, *Chem. Eng. Sc*. **56**, pg. 579, 2001

97. J.G.H. Borkink, K.R. Westerterp, Significance of radial porosity profile for de description of heat transport in wall-cooled packed beds, *Chem. Eng. Sc.* **49**, pg. 863, 1994

98. M. Levent, Water-gas shift reaction over porous catalyst: temperature and reactant concentration distribution, *IJHE* **26**, pg.551-558, 2001

99. O. Kalthoff, D. Vortmeyer, Ignition/Extinction phenomena in a wall cooled fixed reactor, experiments and model calculation including radial porosity and velocity distributions, *Chem. Eng. Sc.* **35**, pg.1637, 1979

100. O. Bey, G. Eigenberger, Fluid flow through catalyst filled tubes, *Chem. Engrg. Sci.* **52**, pg.1365-1376, 1997

101. J.L.M. Dierickx, W.A. Wijnbergh, H. Tuinenbreijer, Similitude of flow dynamics in downscaling trickle flow experiments, Shell International Chemicals, Shell Research and Technology Centre, Amsterdam, October 2001

102. L.M. Rose, Chemical reformer design in practice, Elsevier scientific publishing company, 1981

103. L.D. Schmidt, The engineering of chemical reactions, Oxford University Press, 1998

104. E. Tracz, R. Scholz, T. Borowiecki, High-resolution electron microscopy study of the carbon deposit morphology on nickel catalysts, *Applied Catalysis* **66**, pg.133-148, 1990

105. A.N. Fatsikostas, X.E. Verykios, Reaction network of steam reforming of ethanol over Ni-based catalysts, *JCat* **225**, pg.439-452, 2004

106. M.C. Demicheli, E.N. Ponzi, O.A. Ferretti, A.A. Yeramian, Kinetics of carbon formation from CH_4-H_2 mixtures on nickel-alumina catalyst, *Chem. Engrg. Journal* **46**, pg.129-136, 1991

107. C.H. Bartholomew, Carbon deposition in steam reforming and methanation, *Catalysis Review* **24(1)**, pg.67-112, 1982

108. T. Shishido, M. Sukenobu, H. Morioka, M. Kondo, Y. Wang., K. Takaki, K. Takehira, Partial oxidation of methane over Ni/Mg-Al oxide catalysts prepared by sold phase crystallization method from Mg-Al hydrotalcite-like precursors, *Applied Catalysis A: General* **223**, pg.35-42, 2002

109. V.R. Choudhary, B.S. Uphade, A.S. Mamman, Partial oxidation of methane to syngas with or without simultaneous CO_2 and steam reforming reactions over $Ni/ALPO_4$, *Microporous and Mesoporous Materials* **23**, pg.61-66, 1998

110. H.S. Roh, K.W. Jun, W.S. Dong, J.S. Chang, S.E. Park, Y.I. Joe, Highly active and stable $Ni/Ce\text{-}ZrO_2$ catalyst for H_2 production from methane, *J. Molecular Catalysis A: Chemical* **181**, pg.137-142, 2002

111. Y. Matsumura, T. Nakamori, Steam reforming of methane over nickel catalysts at low reaction temperature, *Applied Catalysis A: General* **258**, pg. 107-114, 2004

112. K. Otsuka, S. Takenaka, H. Ohtsuki, Production of pure hydrogen through catalytic decomposition of methane on supported-Ni based catalysts by cyclic oxidative-activation of the catalysts, in 15th Hydrogen Energy Conference proceedings, Yokohama, 2004

113. S. Subramanian, R.J. Kudia, M.S. Chattha, Treatment of natural gas vehicle exhaust, Catalyst and Emission Technology, SAE International, SP-968

114. R.L. McCormick, M.B. Al-Sahali, G.O. Alpteken, Partial oxidation of methane, methanol, formaldehyde and carbon monoxide over silica: global reaction kinetics, *Applied Catalysis A: General* **226**, pg.129-138, 2002

115. X.M. Liu, G.Q. Lu, Z.F. Yan, J. Beltramini, Recent advances in catalysts for methanol synthesis via hydrogenation of CO and CO2, *Industrial and Engineering Chemistry Research* **42 (25)**, pg.6518-6530, 2003

116. G.Q. Lu, S. Wang, Ni-based catalysts for carbon dioxide reforming of methane, *CHEMTECH* **29 (1)**, pg.37-43, 1999

117. S. Wang, G.Q. Lu, A comprehensive study on carbon dioxide reforming of methane over Ni/γ-Al2O3 catalysts, *Industrial and Engineering Chemistry Research* **38 (7)**, pg.2615-2625, 1999

118. M.V. Twigg, Catalyst Handbook, 2nd Edition, Manson Publishing, 1996

119. K. Tomishige, Y. Matsuo, Y. Yoshinaga, Y. Sekine, M. Asadullah, K. Fujimoto, Comparative study between fluidized bed and fixed bed reformers in methane reforming combined with methane combustion for the internal heat supply under pressurized condition, *Applied Catalysis A: General* **223**, pg.225-238, 2002

120. Y.Z. Chen, B.J. Liaw, W. Lai, ZrO_2/SiO_2 – and La_2O_3/Al_2O_3 – supported platinum catalysts for CH_4/CO_2 reforming, *Applied Catalysis A: General* **230**, pg.73-83, 2002

121. R. Spinicci, A. Tofanari, A study of the catalytic combustion of methane in non-steady conditions, *Applied Catalysis A: General* **227**, pg.159-169, 2002

122. Y. Liu, T. Hayakawa, K. Suzuki, S. Hamakawa, T. Tsunoda, T. Ishii, M. Kumagai, Highly active copper/ceria catalysts for steam reforming of methanol, *Applied Catalysis A: General* **223**, pg.137-145, 2002

123. J.B. Wang, S.C. Lin, T.J. Huang, Selective CO oxidation in rich hydrogen over CuO/samaria-doped ceria, *Applied Catalysis A: General* **232**, pg.107-120, 2002

124. P. Pantu, G.R. Gavalas, Methane partial oxidation on Pt/CeO_2 and Pt/Al_2O_3 catalysts, *Applied Catalysis A: General* **223**, pg.253-260, 2002

125. D.L. Hoang, S.H. Chan, Modeling of a catalytic autothermal methane reformer for fuel cell applications, *Applied Catalysis A: General* **268 (1-2)**, pg.207-216, 2004

126. D.L. Hoang, S.H. Chan, O.L. Ding, Kinetic and modeling study of methane steam reforming over sulfide nickel catalyst on a gamma alumina support, *Chem. Eng. Journal* **112 (1-3)**, pg.1-11, 2005

127. M.J. Moran, H.N. Shapiro, Fundamentals of engineering thermodynamics, 2nd Edition, Wiley, USA, 1993

128. C.R. Ferguson, Internal combustion engines – Applied thermosciences, Wiley, USA, 1986

129. S. Gordon, B.J. McBride, NASA SP-273, USA, 1971

130. Roger A. Strehlow, Fundamentals of combustion, Robert E. Kreiger Publishing Company, New York, 1979

131. J.E. Dennis JR., Robert B. Schnabel, Numerical methods for unconstrained optimization and nonlinear equations, Prentice-Hall, 1983.

132. Joel H. Ferziger, Numerical methods for engineering applications, Wiley, 1981

133. J. Xu, G.F. Froment, Methane steam reforming, methanation and water-gas shift: I. intrinsic kinetics, *AIChE Journal* **35**, pg.88-96, 1989

134. K. Hou, R. Hughes, The kinetics of methane steam reforming over Nia-Al_2O catalyst, *Chem. Eng. Journal* **82**, pg.311-328, 2001

135. D.L. Trimm, C.W. Lam, The combustion of methane on platinum—alumina fibre catalysts--I : Kinetics and mechanism, *Chem. Eng. Sci.* **35**, pg.1405-1413, 1980

136. L. Ma, D.L. Trimm, C. Jiang, The design and testing of an autothermal reactor for the conversion of light hydrocarbons to hydrogen I. The kinetics of the catalytic oxidation of light hydrocarbons, *Applied Catalysis A: General*, **138**, pg.275-283, 1996

137. C. Callaghan, I. Fishtik, R. Datta, M. Carpenter, M. Chmielewski, A. Lugo, An improved microkinetic model for the water gas shift reaction on copper, *Surf. Sci.* **541**, pg.21-30, 2003

138. I. Fishtik, R. Datta, A UBI-QEP microkinetic model for the water-gas shift reaction on Cu(111), *Surface Sci.* **512**, pg.229-254, 2002

139. C.V. Ovesen, B.S. Clausen, B.S. Hammershoi, G. Steffensen, T. Askgaard, I. Chorkendorff, J.K. Norskov, P.B. Rasmussen, P. Stoltze, P. Taylor, A microkinetic analysis of the Water-Gas shift reaction under industrial conditions, *J. Catalysis* **158**, pg.170-180, 1996

140. I. Fishtik, A. Alexander, R. Datta, Enumeration and discrimination of mechanisms in heterogenous catalysis based on response reactions and unity bond index-quadratic exponential potential (UBI-QEP) method, *Surface Sci.* **430**, pg.1-17, 1999

141. G.C. Chinchen, P.J. Denny, J.R. Jennings, M.S. Spencer, K.C. Waugh, Synthesis of methanol: part 1. catalysts and kinetics, *Appl. Catal.* **36**, pg.1-65, 1988

142. G.F. Froment, K.B. Bischoff, Chemical reactor analysis and design, 2nd edition, John Wiley & Sons Inc., 1990

143. D.L. Hoang, S.H. Chan, O.L. Ding, Kinetic modelling of partial oxidation of methane in an oxygen permeable membrane reactor, *IChemE* **83**, pg.1-10, 2005

144. M.J.G. Linders, E.P.J. Mallens, J.J.G.M. van Bokhoven, F. Kapteijn, J.A. Moulijn, Breakthrough of shallow activated carbon beds under constant and pulsating flow, *AIHA Journal* **16**, pg.173-180, 2003

145. J.D. Hoffman, Numerical methods for engineers and scientists, McGraw-Hill, 1993

146. M.K. Szukiewiez, An approximate model for diffusion and reaction in a porous pellet, *Chem. Eng. Sci.* **57**, pg.1451-1457, 2002

147. M. Levent, G. Budak, A. Karabulut, Estimation of concentration and temperature profiles for methane-steam reforming reaction in a porous catalyst, *Fuel Processing Technology* **55**, pg.251-263, 1998

148. R.B. Bird, W.E. Stewart, E.N. Lightfoot, Transport phenomena, John Wiley & Sons Inc., 2nd edition, 2002

149. M. Winterberg, E. Tsotsas, A. Krischke, D. Vortmeyer, A simple and coherent set of coefficients for modeling of heat and mass transport with and without chemical reaction in tubes filled with spheres, *Chem. Eng. Sci.* **55**, pg.967-979, 2000

150. W.M.R. Senow, J.P. Hartneet, Y.I. Cho, Handbook of heat transfer, McGraw-Hill, 3rd Edition, 1998

151. W.J. Beek, K.M.K. Muttzall, Transport phenomena, Wiley, 1983

152. C.J. Geankoplis, Mass transport phenomena, Holt, Rinehart and Winston, New York, 1972

153. S.H. Chan, K.A. Khor, Z.T. Xia, A complete polarisation model of a solid oxide fuel cell and its sensitivity to the change of cell component thickness, *J. Power Sources* **93 (1-2)**, pg130-140, 2001

154. E.L. Cussler, Diffusion: Mass transfer in fluid systems, Cambridge, New York: Cambridge University Press, 1984

155. H.H.S. Chu, S.W. Churchill, C.V.S. Patterson, Effect of heater size, location, aspect ratio, and boundary conditions on two-dimensional, laminar, natural convection in rectangular channels, *J. Heat Transfer* **98 Ser C (2)**, 1976

156. S.H. Chan, D.L. Hoang, P.L Zhou, Heat transfer and chemical kinetics in the exhaust system of a cold-start engine fitted with a three-way catalytic converter, Proceedings of the Institution of Mechanical Engineers, Part D: Journal of Automobile Engineering, **214(7)**, 2000

157. S.T. Lin, Y.H. Chen, C.C. Yu, Y.C. Liu, C.H. Lee, Modelling an experimental methane fuel processor, *J. Power Sources* **148**, pg.43-53, 2005

158. L. Ma, Hydrogen production from steam reforming of light hydrocarbons in an autothermic system, University of New South Wales, 1995

159. M.J. Patterson, D.E. Angove, N.W. Cant, The effect of carbon monoxide on the oxidation of four C6 to C8 hydrocarbons over platinum, palladium and rhodium, *Applied Catalyst B: Environment* **26**, pg47-57, 2000

160. M.J. Patterson, D.E. Angove, N.W. Cant, The effect of metal order on the oxidation of a hydrocarbon mixture over alumina-supported combined platinum/rhodium catalysts, *Applied Catalyst B: Environment* **34 (1)**, pg53-58, 2001

161. C. Wheeler, A. Jhalani, E.J. Klein, S. Thummala, L.D. Schmidt, The water-gas-shift reaction at short contact times, *J. Catalysis* **223**, pg.191-199, 2004

List of author's publication

1. D.L. Hoang, S.H. Chan, O.L. Ding, Hydrogen production for fuel cells by autothermal reforming of methane over sulfide nickel catalyst on a gamma alumina support, *J. Power Sources* **152 (2)**, pg1248-1257, 2006
2. S.H. Chan, D.L. Hoang, O.L. Ding, Transient performance of an authermal reformer – A 2-D modeling approach, *International Journal of Heat and Mass Transfer* **48 (19-20)**, pg4205-4214, 2005
3. D.L. Hoang, S.H. Chan, O.L. Ding, Kinetic and modeling study of methane steam reforming over sulfide nickel catalyst on a gamma alumina support, *Chem. Eng. Journal* **112 (1-3)**, pg.1-11, 2005
4. D.L. Hoang, S.H. Chan, O.L. Ding, Kinetic modelling of partial oxidation of methane in an oxygen permeable membrane reactor, *IChemE* **83**, pg.1-10, 2005
5. O.L. Ding, S.H. Chan, Autothermal Reforming of Methane Gas - Modeling and Experimental Validation, *IJHE,* In-print, 2007

8 Appendix

8.1 Reformer Design

A fuel cell is an electrochemical device that converts the chemical energy of a fuel directly to usable energy such as heat and electricity without combustion as an intermediate step. Fuel cells are similar to batteries in that both produce a DC current by undergoing an electrochemical process Like batteries, fuel cells are combined into groups, called stacks, to obtain a usable voltage and power output.

The size of fuel cells varies with different applications and power requirements. The size of the fuel cell could range from the size of a cellular phone cell for a several watts cell to the size of a football field for a mega-watt power plant.

In a fuel cell power system, a reactor is required to reform the hydrocarbon feedstock into hydrogen before supplying to the fuel cell. As such, the reactor needs to be sized according to the fuel cell power requirement and satisfy the plug flow criteria listed by Dierickx [101] and the residence times provided by Schmidt [103].

The design calculations and drawings for this reactor are shown below:

Assumptions made in this calculation:

- Fuel cell operating at 0.6 V
- Fuel utilisation for PEMFC at 0.6 V is 72%
- Fuel utilisation for SOFC at 0.6 V is 67%
- Void fraction in the reactor is 0.5
- 2 moles of H_2 are produced from 1 mole of CH_4

Given:

- Design power of 1000 W
- 0.18655 gmol of H_2/hrA consumed
- 1.40 x 10^{-5} g of H_2/As consumed
- Molecular weight of H_2 is 2.016
- Diameter of catalyst pellet is 3 mm
- Operating pressure of 1 bar
- Density of CH4 is 0.6367 kg/m^3
- Density of air is 1.1367 kg/m^3
- Density of water is 0.7153 kg/m^3

Criteria to be met:

- Ratio of reactor diameter to pellet diameter must be greater or equal to 10
- Mean resident time of around 0.115 secs
- Pressure drop less than 0.5 bar
- Length of reactor must be 50 to 100 times greater than diameter of pellet

Current required = 1666.6670 A

Mass flow rate of H_2 required = 1.74 x 10^{-2} g/s

Using fuel utilisation of 67%,

Actual mass flow rate of H_2 required = 0.0260 g/s

Molar flow rate of H_2 required = 0.0129 g mol/s

Molar flow rate of CH4 required = 0.0064 g mol/s

Mass flow rate of CH4 required = 0.1034 g/s

Taking AF ratio = 4 and WF ratio = 3

Mass flow rate of air required = 0.4135 g/s

Mass flow rate of water required = 0.3101 g/s

Using design factor of 1.1,

Mass flow rate of CH4 required = 0.1137 g/s

Mass flow rate of air required = 0.4548 g/s

Mass flow rate of water required = 0.3411 g/s

Molar flow rate of CH4 required = 0.0071 mol/hr

Molar flow rate of air required = 0.0159 mol/hr

Molar flow rate of water required = 0.01893 mol/hr

Total flow rate of mixture, $Q = (m/\rho)_{CH_4} + (m/\rho)_{Air} + (m/\rho)_{H_2O}$

$= 0.0106\ m^3/s$

Residence time required, $t = \varepsilon V/Q \leq 0.115$ secs (1)

Where V is obtained from $\varepsilon V = \varepsilon V_C + (V_R - V_C)$

V_R is volume of reactor

V_C is volume of catalyst

Assuming that $V_C = 0.85V_R$ and sub into (1),

$0.575V_R \leq 0.0001214$ (2)

Taking the diameter of reactor to be 30 mm, which is 10 times the diameter of pellet, and sub into (2),

$L_R \leq 0.30$ m

Adding buffer zone to the front and end of the reactor to achieve uniform distribution of the gas mixture, the overall length of the reactor is 0.40 m, which satisfies all the criteria listed.

The actual diameter of the reformer is adjusted to the next best size of the tube that is available off-shelf, which is 32.46 mm. The completed reformer is shown in the figure below.

8.2 ATR experiment data

Mass balance for CH_4 experiment condition at AF= 2.5 and WF= 1.5 (120 l/hr):

	LPM		kg/hr		LPM		%		%		%		%		%		%						
Dry Input	2		0.1772		3.033		12.9		10.33		38.34		5.22		33.21		0						
	CH4	+	H2O	+	Air	~~>	CO	+	CO2	+	H2	+	CH4	+	N2	+	O2						
	l/hr		l/hr		l/hr																		
Dry Volume Conversion	120				181.98																		
	CH4	+	H2O	+	Air																		
	Kg/hr		Kg/hr		Kg/hr																		
Dry Mass Conversion	0.0788652		0.1772		0.21364452																		
	CH4	+	H2O	+	Air																		
	mole		mole		mole		mole		mole		mole		mole		mole		mole						
Dry Mole Conversion	0.004916783		0.009833518		0.007374681		0.002229403		0.00178525		0.006625992		0.00090213		0.005739415		0						
	CH4	+	H2O	+	Air	~~>	CO	+	CO2	+	H2	+	CH4	+	N2	+	O2						
							mole		mole		mole		mole		mole		mole		mole				
Wet Composition							0.002229403		0.00178525		0.006625992		0.00090213		0.005739415		0		0.007130982				
							CO	+	CO2	+	H2	+	CH4	+	N2	+	O2	+	H2O				
							%		%		%		%		%		%		%				
Wet Composition							9.13		7.31		27.14		3.70		23.51		0.00		29.21				
							CO	+	CO2	+	H2	+	CH4	+	N2	+	O2	+	H2O				

Mass balance for CH_4 experiment condition at AF= 3 and WF= 1.5 (120 l/hr):

	LPM		kg/hr		LPM		%		%		%		%		%		%						
Dry Input	2		0.1772		6.066		10.22		11		38.56		1.56		38.67		0						
	CH4	+	H2O	+	Air	~~>	CO	+	CO2	+	H2	+	CH4	+	N2	+	O2						
	l/hr		l/hr		l/hr																		
Dry Volume Conversion	120				363.96																		
	CH4	+	H2O	+	Air																		
	Kg/hr		Kg/hr		Kg/hr																		
Dry Mass Conversion	0.0788652		0.1772		0.42728904																		
	CH4	+	H2O	+	Air																		
	mole		mole		mole		mole		mole		mole		mole		mole		mole						
Dry Mole Conversion	0.004916783		0.009833518		0.014749363		0.002205861		0.00237421		0.008322702		0.000336707		0.008346444		0						
	CH4	+	H2O	+	Air	~~>	CO	+	CO2	+	H2	+	CH4	+	N2	+	O2						
							mole		mole		mole		mole		mole		mole		mole				
Wet Composition							0.002205861		0.00237421		0.008322702		0.000336707		0.008346444		0		0.00907396				
							CO	+	CO2	+	H2	+	CH4	+	N2	+	O2	+	H2O				
							%		%		%		%		%		%		%				
Wet Composition							7.19		7.74		27.15		1.10		27.22		0.00		29.60				
							CO	+	CO2	+	H2	+	CH4	+	N2	+	O2	+	H2O				

Mass balance for CH_4 experiment condition at AF= 3.5 and WF= 1.5 (120 l/hr):

	LPM		kg/hr		LPM		%		%		%		%		%		%								
Dry Input	2		0.1772		7.077		10.11		11.22		33.78		0.22		44.67		0								
	CH4	+	H2O	+	Air	~~>	CO	+	CO2	+	H2	+	CH4	+	N2	+	O2								
	l/hr		l/hr		l/hr																				
Dry Volume Conversion	120				424.62																				
	CH4	+	H2O	+	Air																				
	Kg/hr		Kg/hr		Kg/hr																				
Dry Mass Conversion	0.0788652		0.1772		0.49850388																				
	CH4	+	H2O	+	Air																				
	mole		mole		mole		mole		mole		mole		mole		mole		mole								
Dry Mole Conversion	0.004916783		0.009833518		0.01720759		0.002306667		0.00255992		0.007707143		5.01945E-05		0.010191773		0								
	CH4	+	H2O	+	Air	~~>	CO	+	CO2	+	H2	+	CH4	+	N2	+	O2								
							mole		mole		mole		mole		mole		mole		mole						
Wet Composition							0.002306667		0.00255992		0.007707143		5.01945E-05		0.010191773		0		0.009634196						
							CO	+	CO2	+	H2	+	CH4	+	N2	+	O2	+	H2O						
							%		%		%		%		%		%		%						
Wet Composition							7.11		7.89		23.75		0.15		31.41		0.00		29.69						
							CO	+	CO2	+	H2	+	CH4	+	N2	+	O2	+	H2O						

Mass balance for CH_4 experiment condition at AF= 4 and WF= 1.5 (120 l/hr):

	LPM		kg/hr		LPM		%		%		%		%		%								
Dry Input	2		0.1772		8.088		8.89		10.56		29.67		0		50.89		0						
	CH4	+	H2O	+	Air	~~>	CO	+	CO2	+	H2	+	CH4	+	N2	+	O2						
	l/hr		l/hr		l/hr																		
Dry Volume Conversion	120				485.28																		
	CH4	+	H2O	+	Air																		
	Kg/hr		Kg/hr		Kg/hr																		
Dry Mass Conversion	0.0788652		0.1772		0.56971872																		
	CH4	+	H2O	+	Air																		
	mole		mole		mole		mole		mole		mole		mole		mole		mole						
Dry Mole Conversion	0.004916783		0.009833518		0.019665817		0.002247311		0.00266947		0.007500306		0		0.012864529		0						
	CH4	+	H2O	+	Air	~~>	CO	+	CO2	+	H2	+	CH4	+	N2	+	O2						
							mole		mole		mole		mole		mole		mole		mole				
Wet Composition							0.002247311		0.00266947		0.007500306		0		0.012864529		0		0.010506907				
							CO	+	CO2	+	H2	+	CH4	+	N2	+	O2	+	H2O				
							%		%		%		%		%		%		%				
Wet Composition							6.28		7.46		20.96		0.00		35.95		0.00		29.36				
							CO	+	CO2	+	H2	+	CH4	+	N2	+	O2	+	H2O				

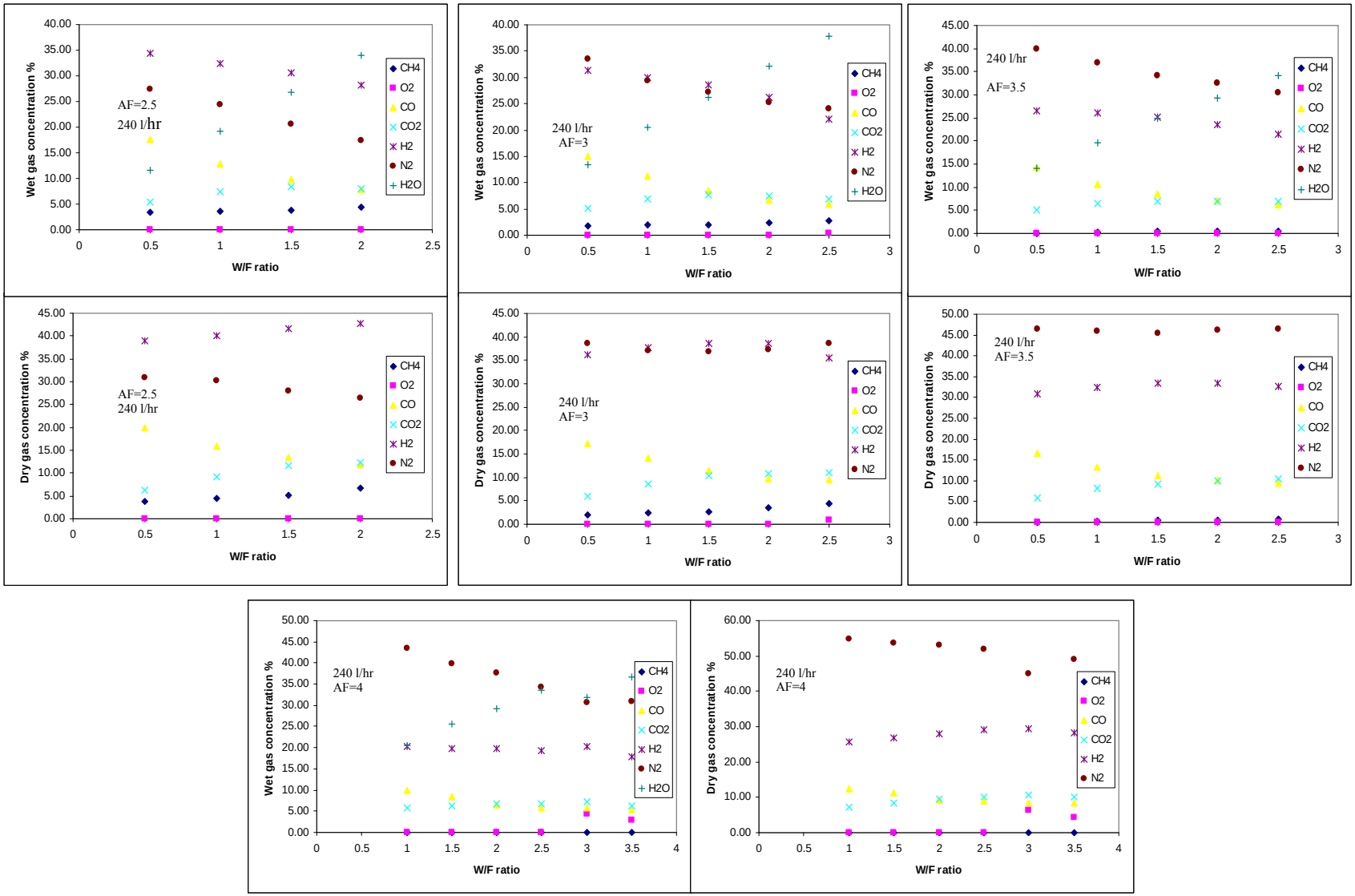

Wet and dry product gas concentrations at different WF and AF ratios (240 l/hr)

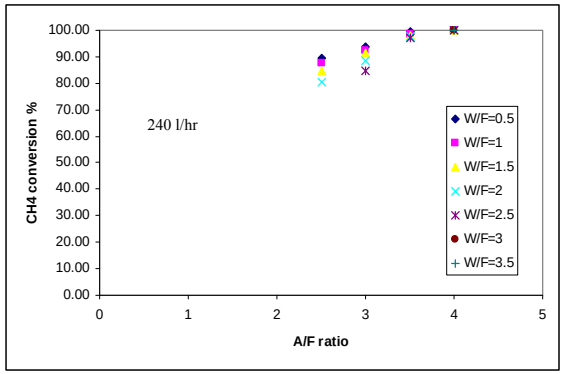

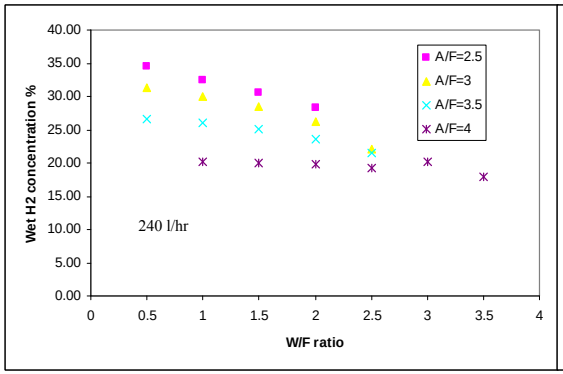

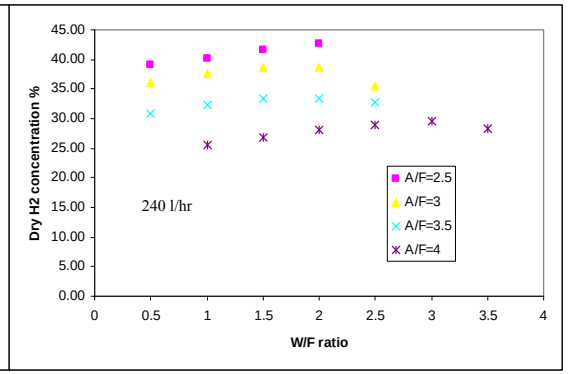

CH_4 conversion at different AF and WF ratios (240 l/hr)

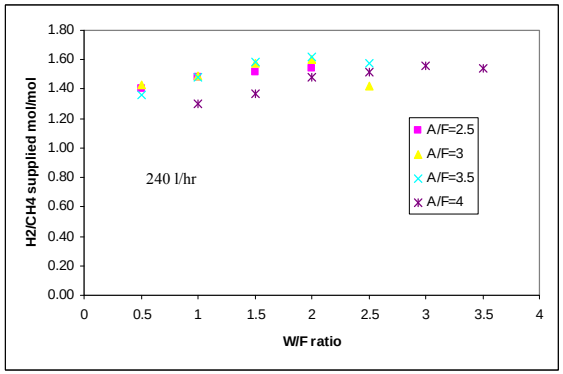

Mole of H_2 produced per mole of CH_4 supplied at different AF and WF ratios (240 l/hr)

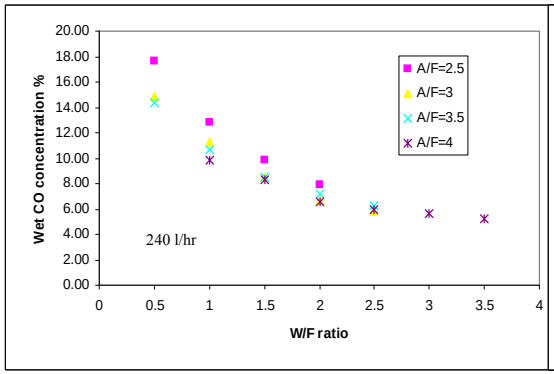

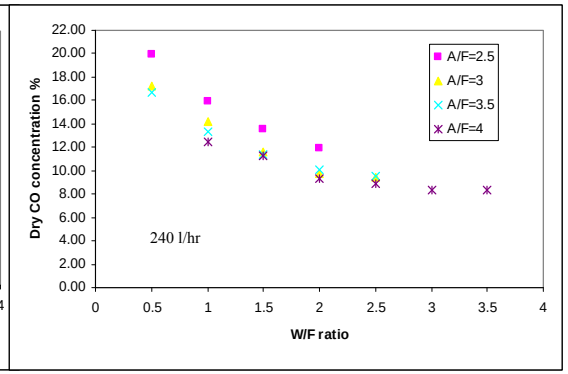

CO concentration at different AF and WF ratios (240 l/hr)

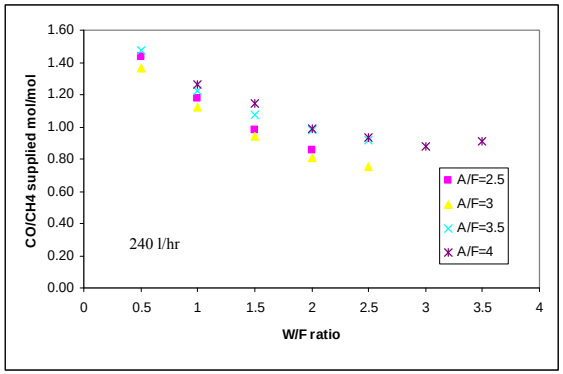

Mole of CO produced per mole of CH_4 supplied at different AF and WF ratios (240 l/hr)

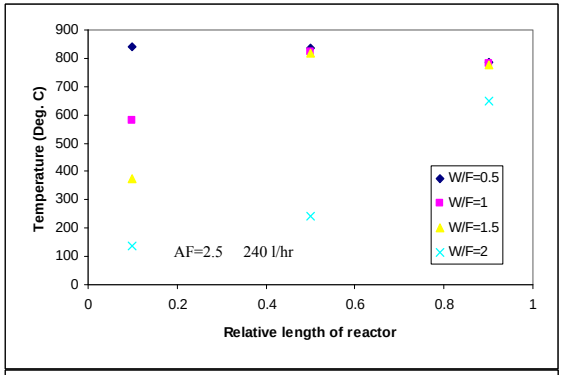

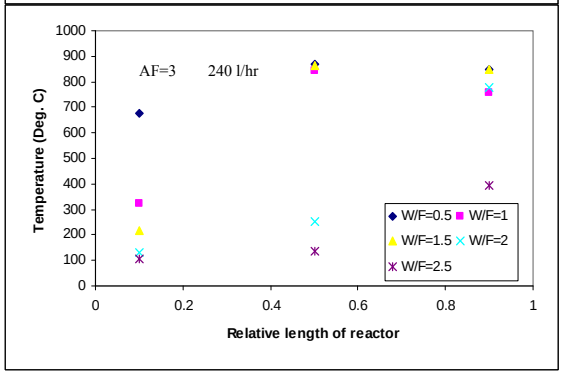

Catalyst temperature along reactor at different AF and WF ratios (240 l/hr)

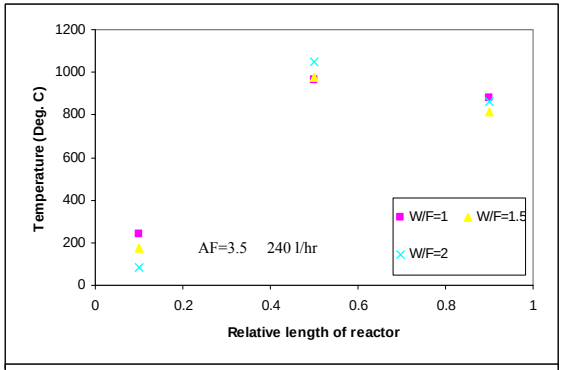

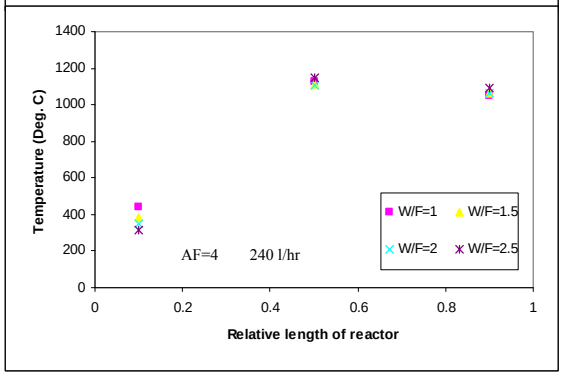

Catalyst temperature along reactor at different AF and WF ratios (240 l/hr)

8.3 STR experiment data

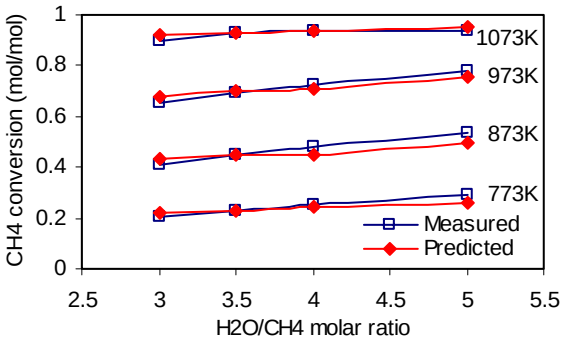

Comparison of predicted and measured total conversion of CH4 per mole of fed CH4 at different reforming temperature, resident time = 3.59 kgcat.s/mole of fed CH4.

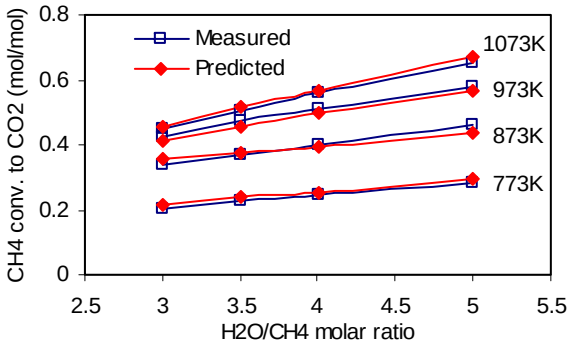

Comparison of predicted and measured conversion of CH_4 into CO_2 per mole of fed CH_4 at different reforming temperature, resident time = 3.59 kgcat.s/mole of fed CH_4.

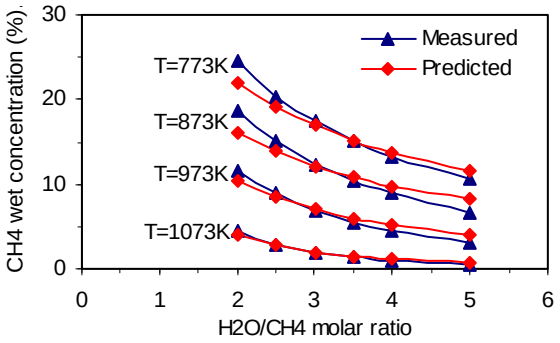

Comparisons of measured and predicted residual CH_4 dry concentration versus H_2O/CH_4 molar ratio at resident time of 3.59 kgcat.s/mol CH_4

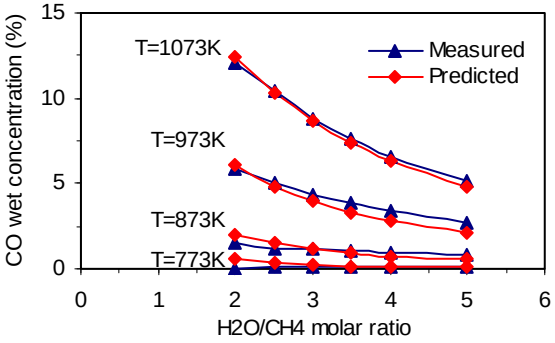

Comparisons of measured and predicted CO wet concentration versus H_2O/CH_4 molar ratio at resident time of 3.59 kgcat.s/mol CH_4

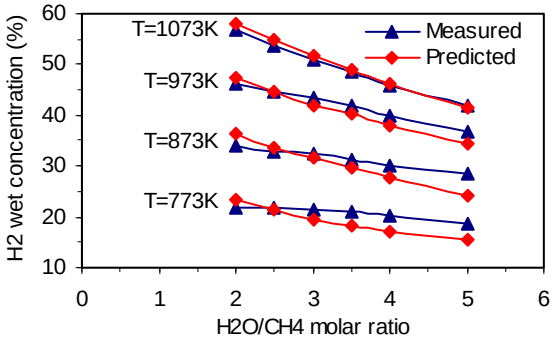

Comparisons of measured and predicted H_2 wet concentration versus H_2O/CH_4 molar ratio at resident time of 3.59 kgcat.s/mol CH_4